PAVEMENT HYDROPLANING RISK EVALUATION WITH INERTIAL MEASUREMENT UNIT (IMU) AND 1MM 3D TEXTURE DATA

By

WENTING LUO

Bachelor of Science in Business Administration
Beijing University of Civil Engineering and Architecture
Beijing, China
2006

Master of Science in Safety Engineering
Beijing Jiaotong University
Beijing, China
2008

Master of Science in Civil Engineering
University of Arkansas
Fayetteville, United State
2012

Submitted to the Faculty of the
Graduate College of the
Oklahoma State University
in partial fulfillment of
the requirements for
the Degree of
DOCTOR OF PHILOSOPHY
July, 2015

PAVEMENT HYDROPLANING RISK EVALUATION WITH INERTIAL MEASUREMENT UNIT (IMU) AND 1MM 3D TEXTURE DATA

Dissertation Approved:

Dissertation Advisor: Dr. Kelvin C. P. Wang

Committee member: Dr. Stephen Alan Cross

Committee member: Dr. Qiang Li

Outside Committee member: Dr. Joshua Habiger

ACKNOWLEDGEMENTS

I would like to express my appreciation and thanks to my advisor Professor Dr. Kelvin C.P. Wang, who is a great mentor for me. His rigorous academic attitude set a great model for me to follow. My deep gratitude goes to Dr. Wang as well for his patience and assistance during my hardship. Without his generosity and guidance, I would not accomplish this degree. His advice on both research and my career are priceless. I also want to thank Dr. Wang's wife, Lily Liu, for her assistance and advice on my daily lives.

Many thanks go to my committee member, Professor Dr. Stephen Alan Cross, for his constructive advice on my dissertation. I express my deep gratitude to my committee member, Dr. Qiang Li, as well for his kindness and academic guidance. I would like to give my sincere appreciation to Dr. Joshua Habiger, who is one of my academic committee members, for his wonderful teaching and valuable advice on my dissertation.

Many thanks also go to the research team members, Dr. Cheng Chen, Dr. Vu Nguyen, Mr. Lin Li, Mr. Justin Thweatt, Mr. Guangwei Yang, Mr. Aonan Zhang, Mr. Yang Liu for their sincere assistance and wonderful collaboration.

Special thanks to my family. Words cannot express my gratitude to my mother, my father, my mother-in law, and my father-in law. During the degree-seeking years, they took turns to serve or care for our family. Without their sacrifices, completing this degree would take even longer time. I would also like to thank all of my friends who supported me in writing, and encouraged me to strive towards my goal. At the end I would like express appreciation to my husband Lin Li who spent sleepless nights with me and was always my support in the moments when there was no one to answer my queries. The author is very proud of having such a helpful, understandable, and obedient daughter Jessie Li. The author also would like to give thanks to the Lord and give us a healthy and lovely son Ethan Li.

Name: WENTING LUO

Date of Degree: JULY, 2015

Title of Study: PAVEMENT HYDROPLANING RISK EVALUATION WITH INERTIAL MEASUREMENT UNIT (IMU) AND 1MM 3D TEXTURE DATA

Major Field: CIVIL ENGINEERING

Abstract: During wet weather automobiles traveling on pavements may experience hydroplaning that would cause out-of-control accidents. Annually 14% of all accidents with fatalities occur on wet pavements. However, not many studies have been conducted on identifying pavement sections with hydroplaning risks for pavement safety survey purpose. This is primarily due to two facts: 1) that it is difficult to acquire the high-quality texture and geometry data which serve as basis data for hydroplaning study; 2) that the existing hydroplaning speed prediction models may not be applicable on irregular pavement sections e.g. pavements with large slopes or long rutting track. To overcome these limitations, in this study PaveVision3D Ultra is used to collect 1mm 3D texture data with full lane coverage at highway speed. Inertial Measurement Unit (IMU) system is used to measure the geometry feature of pavements such as cross slope and longitudinal grade. ANalysis Of VAriance (ANOVA) test results indicated the collected texture data have good reliabilities if the data collection is conducted at a constant speed, while IMU data have the good repeatability regardless of data collection speed. Subsequently the existing prediction models are evaluated by validating the predicted water film depth (WFD) and hydroplaning speed with the measured values from eTape liquid level sensor and Dynamic Friction Tester (DFT). Results indicate the predicted values from Gallaway and University of South Florida (USF) models have good agreements with the ground truth. However, the two models only functions well on regular pavement. For pavements with large slopes or long rutting track, the models might work properly since effects of large slope and rutting on hydroplaning are not considered. In this study impacts of large slopes on vertical load are considered and incorporated the existing models. A new model named as 3S-WFD model is developed in the research to estimate water film depth of rutting pavement under three scenarios. Finally case studies are provided for hydroplaning evaluation on regular pavements, large sloping pavements, and rutting pavements, respectively. Results indicate the data and models used in this study can efficiently identify pavement segments with potential hydroplaning risks so that pavement engineers can take remedial measures to minimize potential traffic accidents. The methodologies proposed in the research would be beneficial in complementing the network level pavement safety survey by highway agencies.

TABLE OF CONTENTS

Chapter Page

LIST OF TABLES

Table Page

LIST OF FIGURES

CHAPTER 1. INTRODUCTION

1.1 Background

When vehicle or aircraft tires roll over water-covered or -flooded pavements, a layer of water film would be developed between tires and pavement surface. The resulting uplift force or pressure from water film would raise a portion of the tire off the pavement. Typically water pressure increases with the increase of vehicle velocity. The water film would separate larger portions of contact areas between tires and pavements until a critical speed termed hydroplaning speed is reached. At the hydroplaning speed, the tire is only supported by the water and thereby loses all contact with the pavement. The automobiles or aircraft under hydroplaning condition would pose substantial danger to traveling public as the vehicle would have a high level of possibility of losing control.

Hydroplaning risk evaluation has become a useful tool for pavement safety management. Substantial research efforts indicated prediction of pavement hydroplaning speed primarily depends on three factors: tire properties, pavement subsurface drainage, and pavement surface drainage (Gallaway 1971). Tire characteristics research includes studies on tire thread pattern, tire width, tire footprint, traffic load, vehicle speed, and inflation pressure (Kumar 2010, Jenq 2011, Ong 2008, Cao 2011, and Okano 2001). Studies on pavement subsurface drainage primarily involve pavement types, layer structure, and layer penetration (Ahmed 1997, Christorpher 1997, and Mallela 2000). Surface drainage ability is closely related to the pavement geometric design (pavement width, cross slope, and longitudinal slope), rainfall intensity, and surface texture properties (Kumar 2010, Ong 2008, Ong 2007, Okano 2001, Christorpher 1997, and Mallela 2001).

Numerous field studies were dedicated to develop hydroplaning prediction models in the past decades (Horne 1963). The existing models can be grouped into two categories: empirical models and analytical models (Chesterton 2006). The empirical methods use experimental data and equations to predict hydroplaning, including Road Research Laboratory (RRL) equations to estimate water film depth (WFD) (Russam 1968), National Aeronautics and Space Administration (NASA) models developed based on aircraft tire and airport pavement data (Horne 1963), and Gallaway model to predict roadway hydroplaning (Gallaway 1979). The analytical methods attempt to mathematically model hydroplaning of the sheet flow and its interaction with a tire, including analytical PAVDRN computer program developed by Pennsylvania State University (Huebner 1996), and the University of South Florida (USF) model based on Ong and Fwa's numerical prediction (Gunaratne 2012).

Figure 1.1 shows a timeline of some significant pavement safety-related studies and events (Smith 2011) on hydroplaning research. Several years after the First International

Skid Prevention Conference (Charlottesville, Virginia) in 1958 and 1 year after the historic Highway Safety Act of 1966 which authorized states to use federal funds to develop and strengthen their traffic safety programs, the first major guidance in the U.S. on pavement surface friction was published in National Cooperative Highway Research Program (NCHRP) Report 37 (Larson and Smith 2010). Although responsibility for highway safety was given to the states in 1971, a considerable amount of work on pavement skid resistance and friction was conducted in the early1970's, culminating in various Highway Research Board (HRB) workshops and syntheses, a symposium on skid resistance sponsored by the American Society for Testing and Materials (ASTM), and the publication of AASHTO's Guidelines for Skid Resistant Pavement Design (Larson 2010).

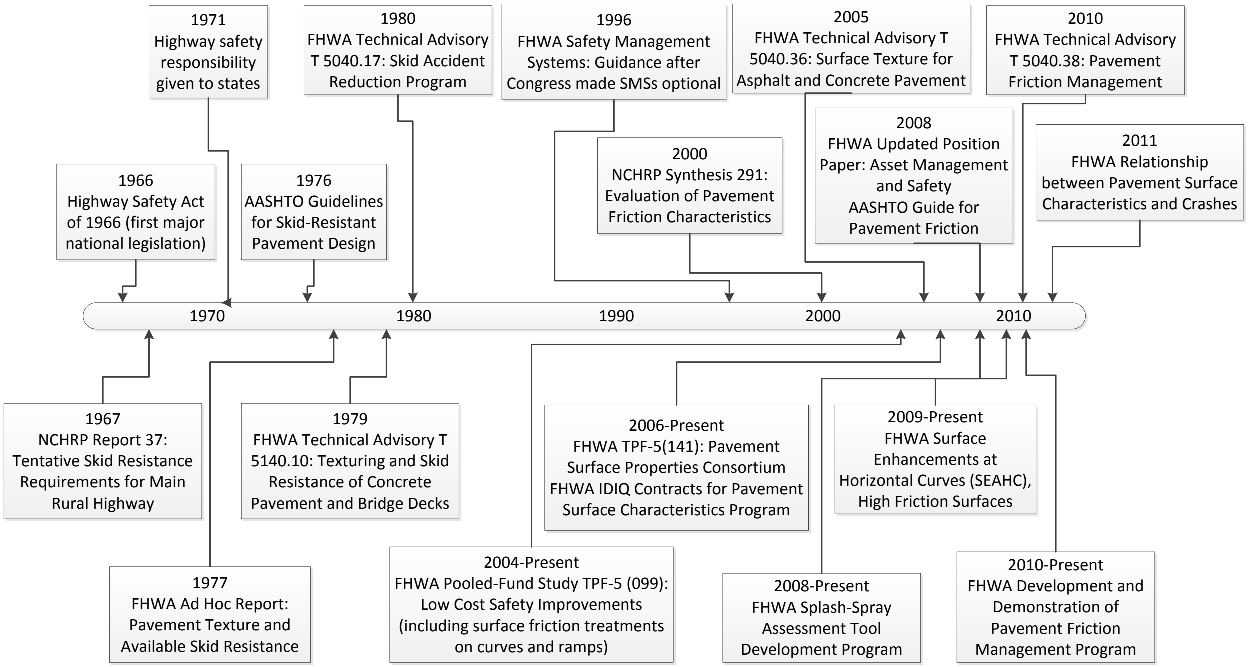

Figure 1.1 Historical timeline of significant pavement safety-related activities (Larson 2010)

1.2 Problem Statement

Past studies on pavement surface drainage focus on the drainage facility design, while limited research work has been conducted to evaluate the capability of existing pavement surface drainage at network levels due to limitations such as the existing data acquisition systems being incapable of continuously measuring surface texture at high speeds.

For pavement texture measurement systems, the traditional manual methods such as Sand Patch Method (SPM) is time consuming and labor intensive, and the collected texture data are usually restricted on a small area. The high-speed inertial profiling systems enable to produce one line-of-sight profile at high speeds in the traveling direction, but still cannot represent the entire pavement, especially for the irregular pavement surface. Due to unavailability of pavement texture data, several studies on pavement drainage capacities assumed the pavement surface to be smooth and uniform, and effects of pavement texture on pavement drainage was ignored (Ong 2008, Wang 2011, and ASTM 2005). However, pavement texture should not be negligible since it is an important contributing factor for water film depth calculation. Usually pavement texture properties are different on wheel path area and non-wheel path area due to pavement abrasion or wear of wheels, and therefore texture data collected in high resolution and full lane coverage is important in water film depth calculation and the subsequent hydroplaning speed prediction.

Pavement geometry measurement systems can be grouped into categories. The manual methods need traffic control and present a potential hazard to operators, therefore the automated methods are proposed as the promising alternative for pavement cross slope and longitudinal grade measurement. The widely used equipment including laser based measurement device and Inertial Measuring Unit (IMU) are always mounted on the survey vehicle for road geometry measurement. The automated methods are based on the assumption that the survey vehicle floor is parallel with pavement surface during travelling (Bolzon 2007, Caroti 2010). However, in real world the vehicle floor is not parallel with pavement surface during travelling, which can be caused by: 1) uneven gravity distribution of the vehicle; 2) vibration of the vehicle during travelling; 3) pavement surface geometry and condition. Therefore, the current automated methods have a limitation.

In the past decades numerous field studies were conducted to develop hydroplaning prediction models to integrate all the intervening factors on hydroplaning evaluation (Chesterton 2006). The rainfall intensity, tire inflation pressure, tire thread properties, pavement texture characteristics, and pavement geometry are considered as important factors in these models. To validate the capability of the models, the flat and straight pavements with good condition are selected as test beds. However, these models cannot produce accurate results on pavement sections on horizontal curves, and with large longitudinal slopes, and pavement rutting since some important factors (e.g. impacts of pavement slope on vertical load and rutting on water film depth) are not considered in these models.

1.3 Hydroplaning Risk Evaluation Approach

Digital Highway Data Vehicle (DHDV), developed by the WayLink Systems Corporation with collaborations from the University of Arkansas and the Oklahoma State University, has been have evolved into the sophisticated systems to conduct full lane data collection on roadways as highway speed up to 60mph. With the latest PaveVision3D

Ultra (3D Ultra for short), the collected data includes 2D/3D data, Right of Way (ROW), profile and texture data, and Inertial Measurement Unite (IMU) data. In this study two data sets are mainly considered: IMU data and 3D texture data since the drainage capacity of pavement surface is primarily related to pavement texture properties, cross slope, longitudinal grade, and pavement rutting. The implementation for the network-level pavement hydroplaning evaluation can be schematically described by Figure 1.2.

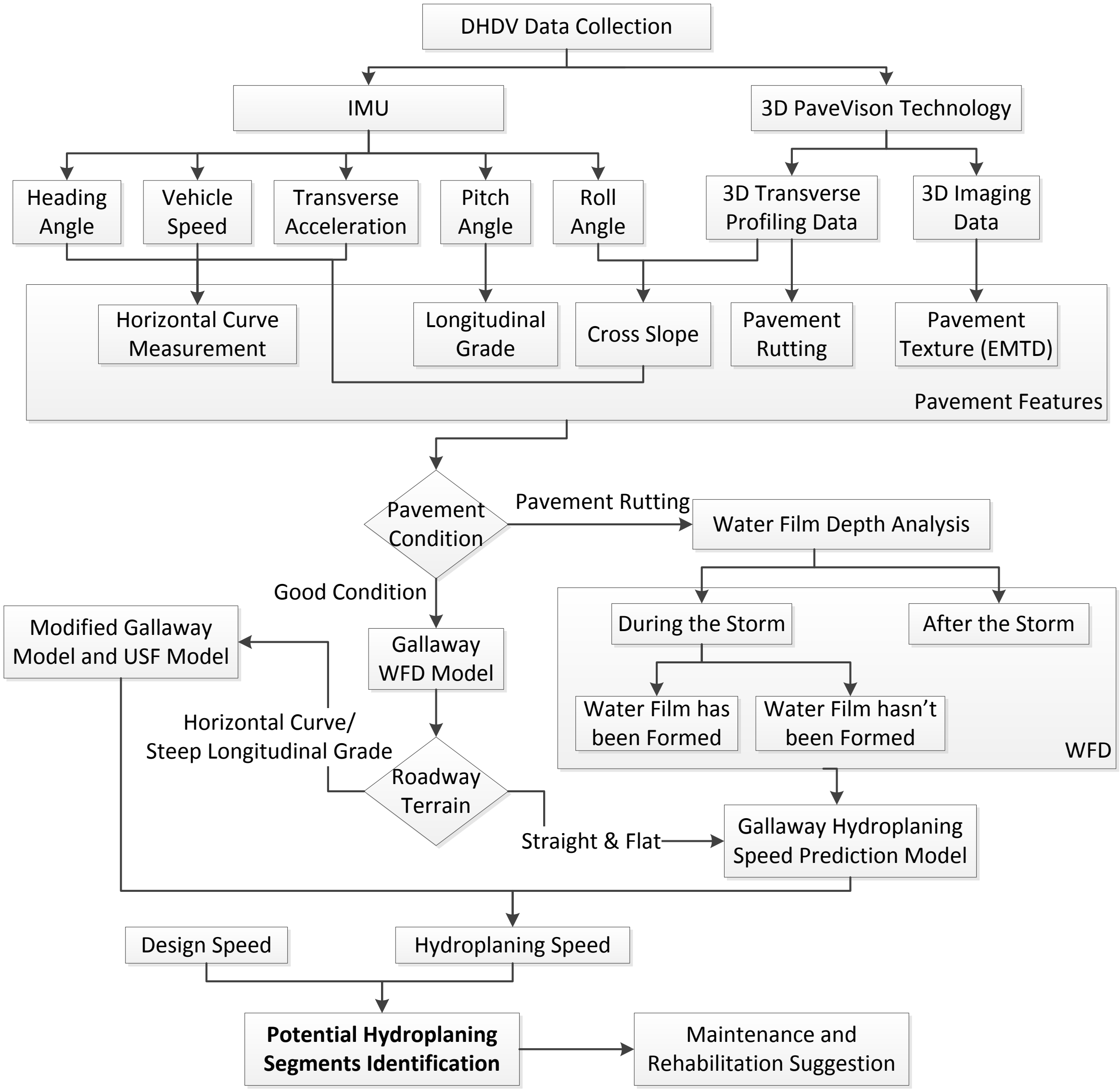

Figure 1.2 The diagram for network level pavement hydroplaning evaluation

In DHDV the signal or pulses to acquire 3D texture data is controlled and triggered by Distance Measurement Instrument (DMI). The signal to capture the IMU data is controlled and triggered by GPS receiver. Matching the IMU data set with the 3D imaging data set is critical for the following hydroplaning speed prediction since they are triggered by different signal sources. Subsequently the Mean Texture Depth (MTD) is calculated with 1mm 3D texture data, and geometry features are measured with 3D profiling data and IMU data. Finally the water film depth and hydroplaning speed can be estimated by incorporating the MTD, cross slope, and longitudinal grade into hydroplaning prediction models. By comparing the posted speed limit with the predicted hydroplaning speed, the potential hazardous locations on test sections can be identified so that the remedial measures can be taken to reduce the hydroplaning risk related accidents.

1.4 Study Objectives

The main objectives of the dissertation are presented as follows:

- Analyze intervening factors on hydroplaning and evaluate the current hydroplaning prediction models;
- Match the 1mm 3D texture data and IMU data, based on which the MTD is calculated and geometry features are calibrated;
- Improve the current models to estimate hydroplaning speed on road sections with horizontal curve, large longitudinal slope, or long rutting track;
- Develop a software to process 3D texture and IMU data so that hydroplaning speeds can be estimated with various models;
- Identify the hazardous locations with the predicted hydroplaning speeds for the purpose of network level pavement safety evaluation.

CHAPTER 2. LITERATURE REVIEW

2.1 Hydroplaning Phenomenon

Hydroplaning phenomenon might occur when a vehicle drives on a wet road covered by water film since the developed water film would diminish the frictional force between tires and pavement surface. According to Negrini (2003), the phenomenon of hydroplaning may occur in three forms:

- Dynamic Hydroplaning: it occurs when the water film on the track presents a height superior to 0.25 cm, which is associated to high intensity precipitations;
- Viscous Hydroplaning: it occurs when the water film has thickness of hundredths of millimeter, condition where the viscous properties of the water make it act as a lubricant, generating enough hydrostatic pressures to raise the tires;
- Reverted Rubber Hydroplaning: it is a rare phenomenon in road traffic accidents, but not uncommon in aircraft accidents. It occurs when, as a result of a long sideslip of a tire, there is the generation of high temperatures.

One study conducted by the National Aeronautics and Space Administration (NASA) demonstrated that there are three distinct zones of tire-wet pavement contact areas, where the percentage of occurrence of hydroplaning in these areas depends on the vehicle speed, pavement texture, and tire inflation pressure, as presented in Figure 2.1 (Okano 2001). Table 2.1 shows the relationship between the hydroplaning form and three zones.

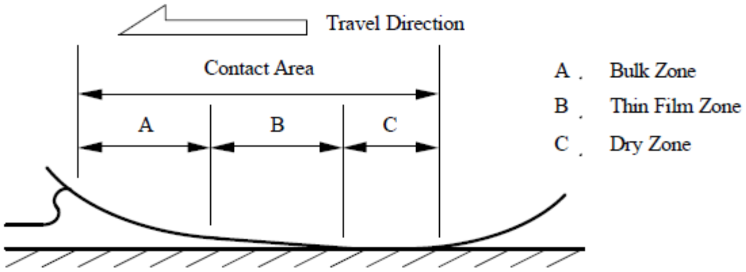

Figure 2.1 Three zone concept (Okano 2001)

Table 2.1 Total and Partial Hydroplaning according to the Three Zones Model (Aps 2006)

Parameter	Total Hydroplaning	Partial Hydroplaning	Contact
Zone	A	B	C
Condition of Pavement	Wet	Humid	Dry
Type of Interaction	Skid	Partial Contact	Rolling
Relevant Property	Macro-texture	Micro-texture	Macro & Micro
Occurring Phenomenon	Dynamic Hydroplaning	Viscous Hydroplaning	Friction

2.2 Intervening Factors on Pavement Hydroplaning

2.2.1 Pavement Texture

The irregularities of pavement surface from its smooth horizontal plane surface are known as surface textures (Wambold 1995). The available surface textures depend on aggregate mineralogy, aggregate size and gradation in the surface mix, voids in surface mix, pavement finishing and texturing techniques, and surface wear. The surface textures are classified into micro-texture, macro-texture, mega-texture and unevenness (roughness) based on texture sizes as indicated by texture amplitude (depth) and wavelength (Wambold 1995; ASTM E 867), as given in Table 2.2.

Table 2.2 Classification of Pavement Texture (ASTM E-867)

Domain	Interval of Dimensions	
	Horizontal	Vertical
Micro-texture	0 -- 0.5 mm	0 -- 0.2 mm
Macro-texture	0.5 mm -- 50 mm	0.2 mm -- 10 mm
Mega-texture	50 mm -- 500 mm	1 mm -- 50 mm
Irregularity	0.5 m -- 50 m	1 mm -- 20 cm

2.2.1.1 Effects on Pavement Drainage

Pavement texture depth affects the water accumulation and water dispersion. Well-textured pavements can provide flow paths to allow water in front of the tire to be forced out under pressure. Panie's study (1969) shows the relation between four types of concrete pavement surface treatment and hydroplaning potential, including dragged with wire, dragged with broom, dragged with burlap, and grooving. The results shows the pavement surfaces of grooving texture and dragged texture with wire have the better drainage efficiency. Henry's study (2000) summarizes the relationships between texture properties and tire-pavement interaction effects (Figure 2.2): 1) an increased texture depth is desired for increased and durable friction, and thereby safety and economy; 2) increased texture depth may affect the driver/residents comfort and economy in terms of noise, vehicle vibration, fuel consumption, and tire and vehicle wear.

2.2.1.2 *Texture Measurement Methods*

The methodologies for texture measurements can be roughly grouped into two categories: static and high-speed methods. The static test methods contain SPM which is commonly used for determining Mean Texture Depth (MTD) (ASTM E965), Circular Track Meter (ASTM E 2157), and Outflow Meter (ASTM E 2380). The static methods are conducted on the marked small areas, not suitable for project and network level applications. As for the high-speed test techniques e.g. the laser based data acquisition systems (ASTM E1845), their measurements mainly conducted on one longitudinal profile or line-of-sight, and the produced texture index is termed as the Mean Profile Depth (MPD).

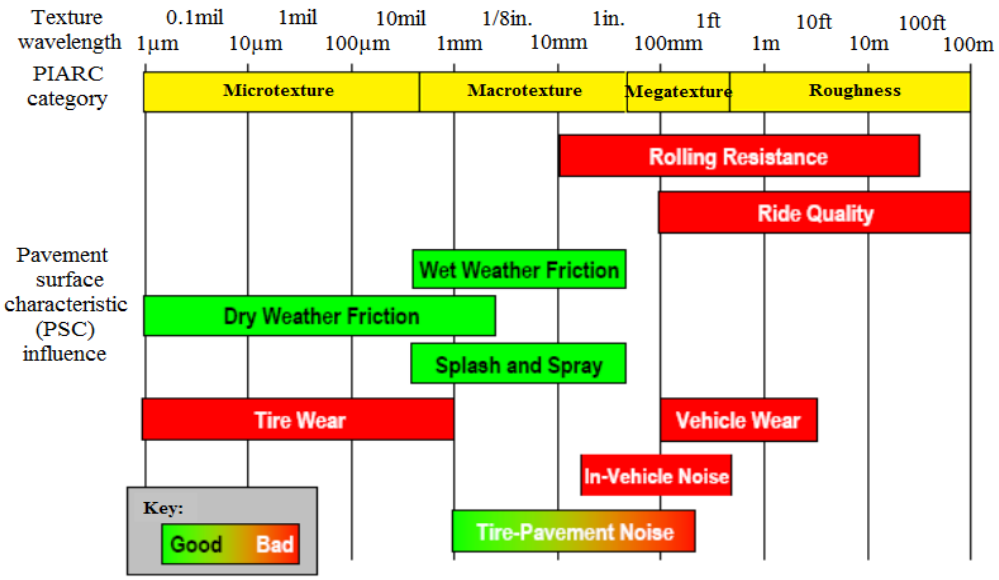

Figure 2.2 Ranges of texture and anticipated effects (Henry 2000)

ASTM E 965 describes a procedure to determine the average depth of pavement surface macro-texture by the use of a known volume of material on test surface and subsequent measurement of the total area covered. This measurement of surface texture depth reflects the pavement macro-texture characteristics. Equations 2.1 and 2.2

mathematically describe the average pavement macro-texture depth, and Figure 2.3 shows the instruments for sand patch method.

$$V = \frac{\pi d^2 h}{4} \tag{2.1}$$

$$MTD = \frac{4V}{\pi D^2} \tag{2.2}$$

Where V: internal cylinder volume, in^3; d: internal cylinder diameter, in; h: cylinder height, in; MTD: mean texture depth of pavement macro-texture, in; D: average diameter of the area covered by the material, in.

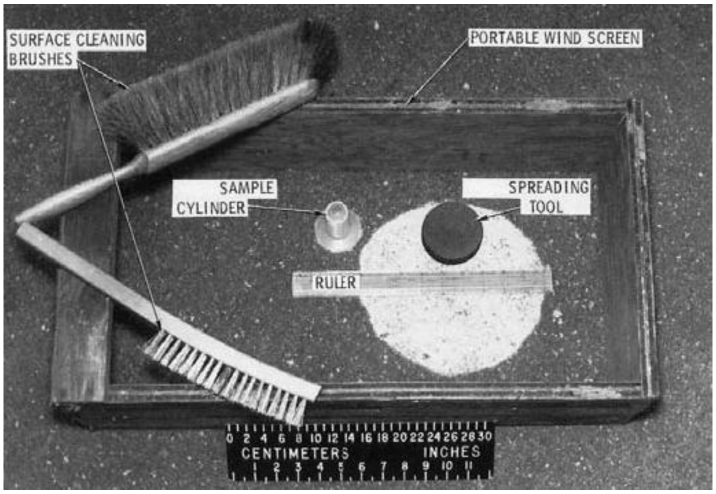

Figure 2.3 Apparatus for measuring surface macro-texture depth (ASTM E 965)

ASTM E 2157 describes the procedure for obtaining pavement macro-texture properties using the Circular Track Meter (CT-Meter). The CT-Meter consists of a Charge Coupled Device (CCD) laser displacement sensor mounted on an arm. When the arm rotates, the displacement sensor collects the profile data follows a circular track, as Figure 2.4 shows. Equation 2.3 shows the recommended relationship for the estimation of the MTD from the MPD by the CT-Meter.

$$MTD = 0.947MPD + 0.069 \tag{2.3}$$

Where, MTD: mean texture depth of pavement macro-texture, mm; MPD: mean profile depth of pavement macro-texture, mm.

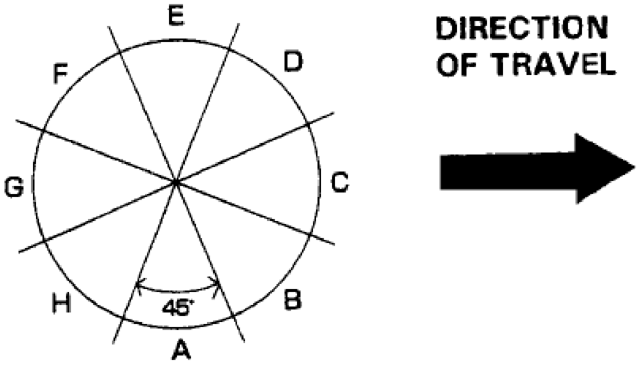

Figure 2.4 Segments of the Circular Track Tester (ASTM E 2157)

ASTM E 2380 describes the connectivity of the textures it relates to the drainage capability of the pavement through its surface and subsurface voids. For the test, the outflow meter is placed on the pavement with the plunger sealing the water discharge opening. Sufficient water is then poured into the cylinder to raise the switch floats to their raised or top position, which will prevent the timer from operating, as Figure 2.5 shows.

Figure 2.5 Outflow Meter (ASTM E 2380)

For each test section, the arithmetic average from all outflow meter test times will be determined and recorded to the 0.01 s. The Equation 2.4 is used to estimate the mean texture depth in this method.

$$MTD = \frac{3.114}{OFT} + 0.636 \tag{2.4}$$

Where MTD: volumetric texture depth defined in Terminology; OFT: outflow meter test times.

2.2.2 Pavement Geometry

Roadway design features are highly associated with the drainage capacity of pavement surfaces, including pavement lane width, cross slope, longitudinal grade, and curve radius. The minimum lane width from AASHTO geometric design are shown in Table 2.3.

Table 2.3 Minimum Lane Width (AASHTO, 2004)

Type of Roadways	Minimum Lane Width (feet)
Freeway	12
Major Arterials	11
Minor Arterials	11
Collectors (Major and Minor)	11
Local Roads	10
Auxiliary Lanes	10

It is more important to maintain a minimum longitudinal grade on curbed pavements than on uncurbed pavements in order to avoid undue spread of storm water on the pavement. Table 2.4 shows the maximum longitudinal grade design for different types of roadways.

The selection of pavement cross slope should be a tradeoff of surface drainage capacity and pavement ride quality requirements. On the straight road section, the recommended pavement cross slope is 0.02 feet per foot, and it shall not be less than 0.015 feet per foot or great than 0.04 feet per foot. The change in cross slope between adjacent through travel lanes should not exceed 0.04 feet per foot (AASHTO 2004).

Table 2.4 Maximum Grade (%) for Specified Design Speed (AASHTO 2004)

Flat Terrain		Design Speed (mph)											
Type of Roadway		15	20	25	30	35	40	45	50	55	60	65	70
Freeway		--	--	--	--	--	--	--	4	4	3	3	3
Arterial	Rural	--	--	--	--	--	5	5	4	4	3	3	3
	Urban	--	--	--	8	7	7	6	6	5	5	--	--
Collector	Rural	--	7	7	7	7	7	7	6	6	5	--	--
	Urban	--	9	9	9	9	9	8	7	7	6	--	--
Local		9	8	7	7	7	7	7	6	6	5	--	--
Industrial		--	--	--	4	4	4	4	3	3	3	--	--
Rolling Terrain		Design Speed (mph)											
Type of Roadway		15	20	25	30	35	40	45	50	55	60	65	70
Freeway		--	--	--	--	--	--	--	5	5	4	4	4
Arterial	Rural	--	--	--	--	--	6	6	5	5	4	4	4
	Urban	--	--	--	9	8	8	7	7	6	6	--	--
Collector	Rural	--	10	10	9	9	8	8	7	7	6	--	--
	Urban	--	12	12	11	10	10	9	8	8	7	--	--
Local		12	11	11	10	10	10	9	8	7	6	--	--
Industrial		--	--	--	5	5	5	5	4	4	4	--	--

Horizontal curve are designed for vehicle driving direction transition, which consists of lead-in/lead out, transition curve, and tangent, as Figure 2.6 shows. The lead-in and lead-out play a major role in gradually adjusting the super-elevation from the regular cross slope on a straight roadway to the maximum super-elevation at the curve, which is also known as super-elevation (Figure 2.7). Table 2.7 shows the relation between the super-elevation and radius of roadway.

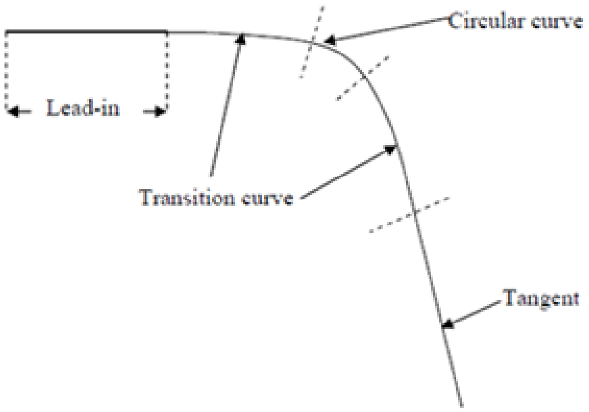

Figure 2.6 Composition of roadway curve (AASHTO 2004)

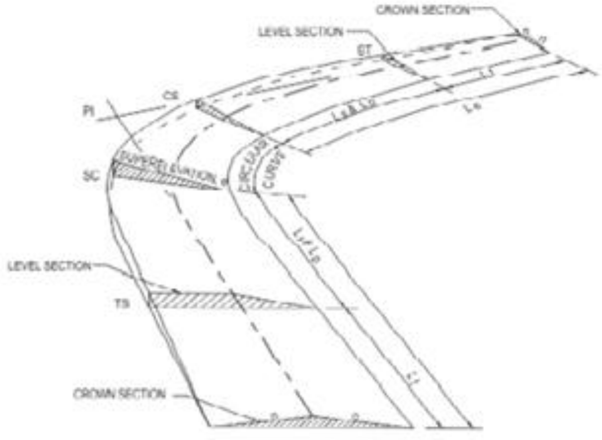

Figure 2.7 Super-elevation design for roadway curve (AASHTO 2004)

Table 2.5 Super-elevation Rates for Curves (AASHTO 2004)

	Design Speed (mph)							
	10	15	20	25	30	35	40	45
Minimum Super-elevation Rate	0	0	0.02	0.04	0.06	0.08	0.09	0.1
Minimum Radius (feet)	25	50	90	150	230	310	430	540

2.2.2.1 Effects on Pavement Drainage

The road geometry such as cross slope and longitudinal grade are important indexes for flow path slope and flow path length calculations. Longer flow paths mean more time to accumulate rainfall and results in thicker film depth. Changes in cross slope and longitudinal grade can help short the flow path length and reduce the time of water running on pavement surface (Chesterton 2006). Figure 2.8 shows relationships of the drainage path and pavement geometric features including cross slope, longitudinal grade, and pavement width.

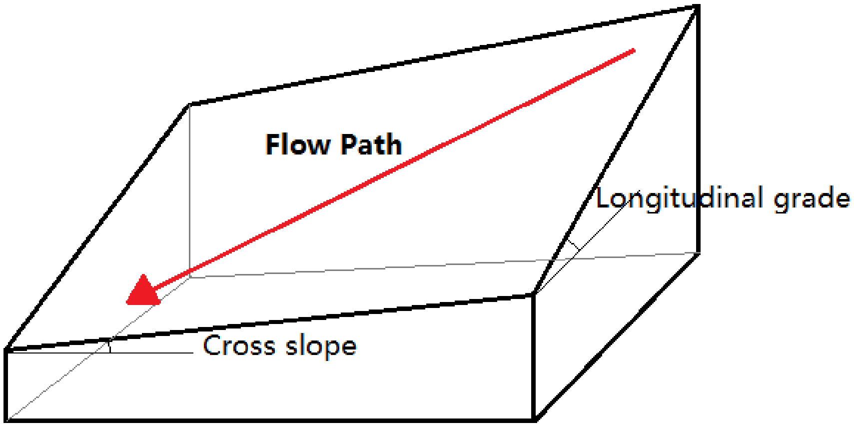

Figure 2.8 Pavement flow path

The flow of water across the surface of a paved roadway is controlled to a large extent, by the longitudinal grade of the roadway and its cross slope. The length of the flow path, L, can be expressed in Equation 2.6, and the slope of the flow path, S, can be evaluated using the Equation 2.7.

$$L = W\sqrt{1 + \left(\frac{g}{S_c}\right)^2} \tag{2.6}$$

$$S = \sqrt{{S_c}^2 + g^2} \tag{2.7}$$

Where L: the length of the flow path, ft; S: the slope of the flow path, %; W: the width of the drainage layer, ft; G: longitudinal grade of the roadway, %; S_c: roadway cross slope, %.

2.2.2.2 Geometry Measurement Methods

(1) Cross slope and longitudinal grade measurement

The measurements of cross slope and longitudinal grade are important for pavement safety. The too small slope and grade can cause hydroplaning issues, while the too large slope and grade may cause vehicle handling problems. The methods for cross slope and longitudinal grade measurements are summarized as follows:

(a). Manual Measurement Method

Currently most highway agencies conduct cross slope and longitudinal grade measurement manually with a digital level (Tsai 2012), as Figure 2.9 shows. However, this method is time-consuming and needs traffic control, and it is not suitable for a network-level survey.

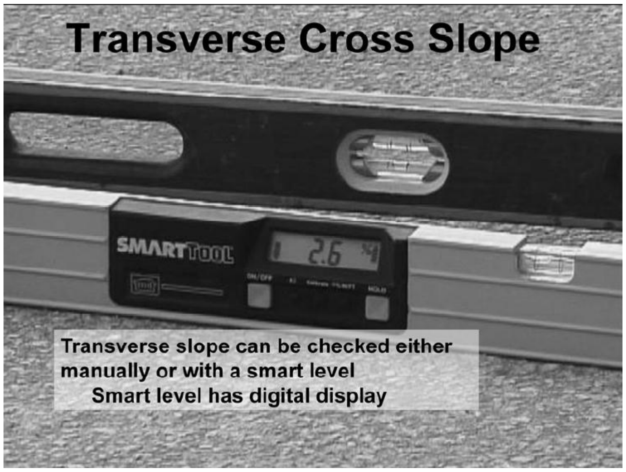

Transverse Cross Slope

Transverse slope can be checked either manually or with a smart level
Smart level has digital display

Figure 2.9 Manual cross slope measurement (Tsai 2012)

(b) Inertial Navigation Systems (INS)/Inertial Measuring Unit (IMU)

INS/IMU, widely used in cross slope measurement, is mounted on a road survey vehicle to measure the vehicle deflection. INS/IMU is a self-contained sensor consisting of three accelerometers and three fiber-optic gyroscopes. The accelerometers are used to establish a vertical position reference of the vehicle, while gyroscopes are used to determine vehicle orientation as well as longitudinal grade and cross-slope (Vemulapalli 2009). Bolzon (2007) assumed that the suspensions have a linear elastic behavior consisting of a two-dimensional (mass-springs) system, in which the mass is a rigid body subject to rotation. With the model lying on an inclined plane and subject to gravity and to a transversal force, a vehicle going along a curvilinear road section with a cross slope α can be measured (Figure 2.10). Due to the deflection of vehicle, the cross slope measured by IMU needs to be calibrated (Figure 2.11).

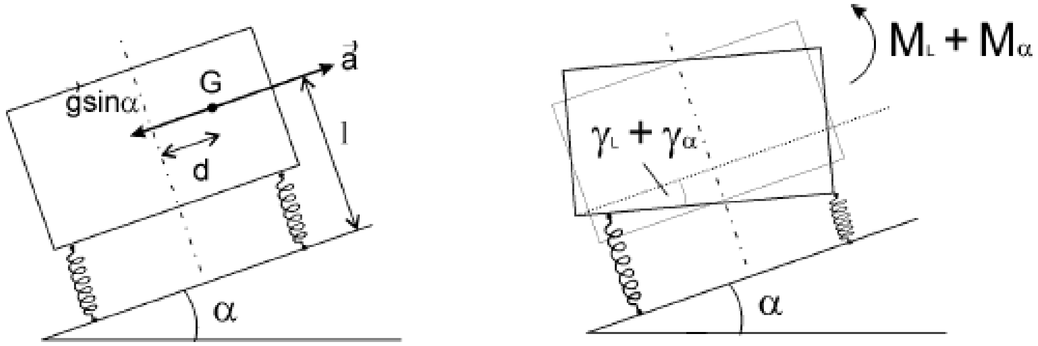

Figure 2.10 Non-deformed and deformed configurations on inclined plane (Bolzon 2007)

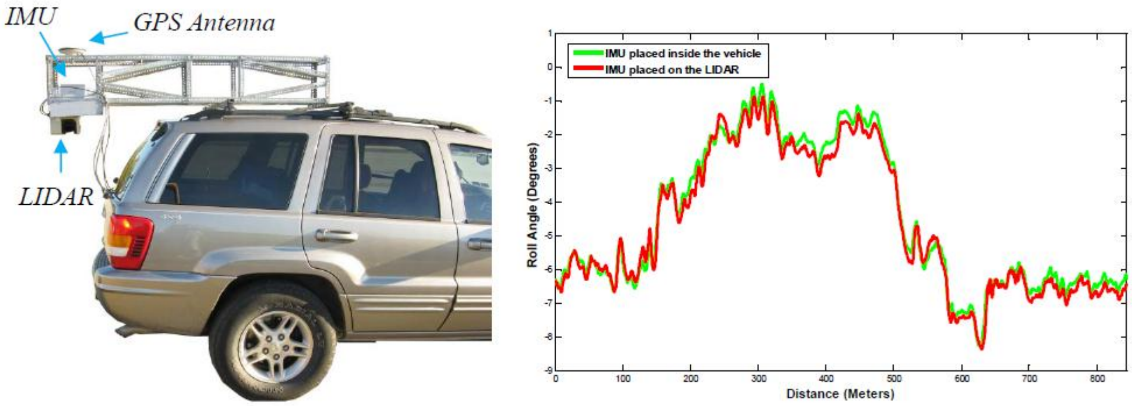

Figure 2.11 IMU Mounted on LIDAR and test results (Vemulapalli 2009)

(c). Laser based Device

Laser based device is also used for the cross slope measurement through calibrating IMU measurements in this research, as Figure 2.12 shows. The distance meter has been overhung on the rear end of the vehicle to survey the cross section of the road. The vehicle's position and trim at each scan time can be obtained via an independent circuit, generating a pulse of adequate amplitude at even intervals (Bolzon 2007).

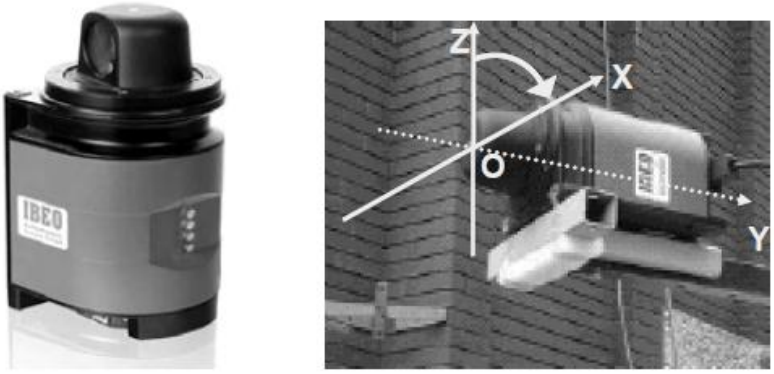

Figure 2.12 Automotive laser sensor (Bolzon 2007)

(2) Horizontal curve measurement

Aside from the cross slope and longitudinal grade measurements, another geometry feature namely horizontal curve radius needs to be measured as well. Generally three approaches are available and summarized as follows:

(a). Ball Bank Indicator (BBI) Method

The BBI (Figure 2.13) measures the combination of lateral acceleration, vehicle body roll and super-elevation, and its calculation is described in Equation 2.8 (Carlson 2008). Each term in Equation 2.8 cannot be individually determined from the BBI reading alone. If body roll is neglected, the BBI reading in degrees would be a direct measure of lateral acceleration, and the radius can be estimated using the point–mass in Equation 2.9.

Figure 2.13 Manual ball-bank indicator (Carlson 2008)

$$BBI = Lateralacceleration - supperelevation + bodyroll \tag{2.8}$$

$$R = \frac{v^2}{127(e+f)} \tag{2.9}$$

Where, R: road curve radius, ft; v: vehicle speed (mph); e: average full supper-elevation, %; f: side friction factor.

(b). Chord Length method

The chord length method is conducted based on a line that touches the circumference of a circle at two points. With the chord method, a technician stretches a string of known length so that each end just touches the lane edge-line of the horizontal curve (Carlson 2005). After the string is stretched, an offset distance is measured from the middle of the string to the lane edge line. With the string length and offset known, the curve radius can be calculated by Equation 2.10.

$$R = \frac{C^2 + 4M^2}{8M} \tag{2.10}$$

Where, R: road curve radius, m; C: length of string, m; M: offset distance, m.

(c). Compass method

The compass method uses the measured length of the curve and the compass heading of each tangent approach to calculate the radius of the curve. The length of the curve is considered to be the average of the lengths measured along the inside and outside lane edge-line paint stripes, and the compass heading is recorded for each tangent approach of the curve. The difference of the two compass headings is calculated in degrees, and the curve radius is calculated by Equation 2.11 (Carlson 2005).

$$R = \frac{57.3 \times L}{\Delta} \tag{2.11}$$

Where, R: roadway curve radius, m; L: length of curve, m; Δ: difference in compass headings, degrees.

2.2.3 Pavement Rutting

Pavement rutting is the accumulation of permanent deformation in all or a portion of the layers in a pavement structure that results in a distorted pavement surface. Rutting occurs only on flexible pavements, as indicated by the permanent deformation along the wheel path. The width and depth of rut are affected by structural property of pavement layers (thickness and material quality), traffic loads, and environmental conditions. Based on the wheel path definition from LTPP (Figure 2.14), the width of lane is assumed as 12ft, and the width of inner and outer wheel path are defined as 2.5ft with their center lines 2.5ft away from the lane edge (Miller, 2003).

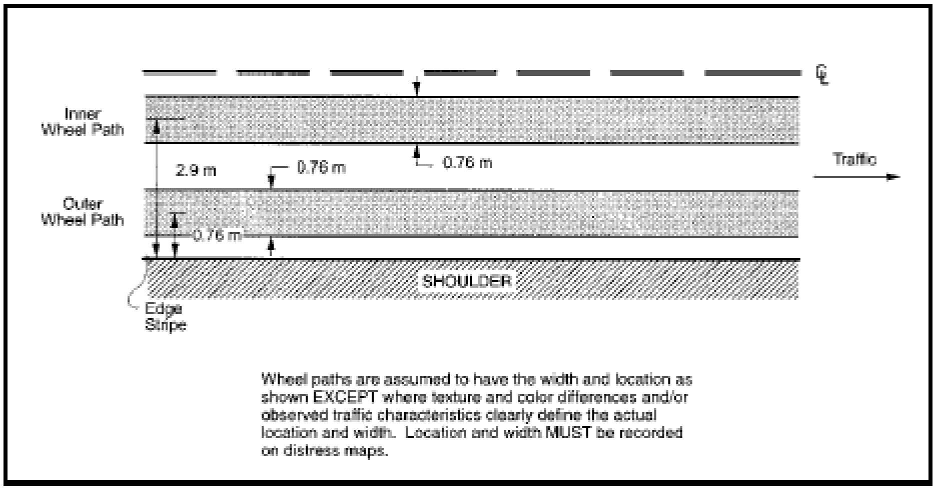

Figure 2.14 Wheel path definition from LTPP (Miller 2003)

2.2.3.1 Effects on pavement drainage

Pavement surface rut can be regarded as a small reservoir during rainy weather (Figure 2.15). The trapped water may separate tires from pavement surface, resulting in the decrease of skid resistance and the increase of potential hydroplaning risks. In addition, the ponding water along the rutting track would be trapped for a long time before they are evaporated into the air or penetrate into the ground, which extends their impacts on safety driving. It should be emphasized that splash and spray from the trapped water would reduce visibility, leading to driving-related safety issues as well

2.2.3.2 Methods for Transverse profile measurement

Five methods have been used to measure pavement rutting depths, as summarized in Table 2.6. The manual methods include dipstick, six foot straight edge, and Roll-O-Matic. The dipstick method (Figure 2.16a) may miss a local maximum rut depth due to the 1 foot intervals of measurement. The six foot straight edge method (Figure 2.16b) only provided the maximum rut depth, not the lateral location or volume of the water a rut might hold. The pavement management vans only provide an average rut depth for the entire length of the cell, and may not capture the local maximum rut depth as it travels along each test cell. However, only the Roll-O-Matic and Automated Laser Profile System methods (Figure 2.16c) provide enough data to determine both the maximum rut and volume of the water a rut might hold.

Figure 2.15 Pavement rutting track

Table 2.6 Five Methods for Pavement Rutting Measurement (MnROAD 2011)

Measurement Device	Type of Measurement
Six Foot Straight Edge	Determines maximum rut depth manually
Dipstick	Measures transverse surface profile at 1ft intervals
Roll-O-Matic	Obtains continuous trace of transverse surface profile on paper
Pavement Management Van	Measures average rut depth along entire length of test cell
Laser Profile System	Measures transverse profile at 0.25 inch intervals with a laser

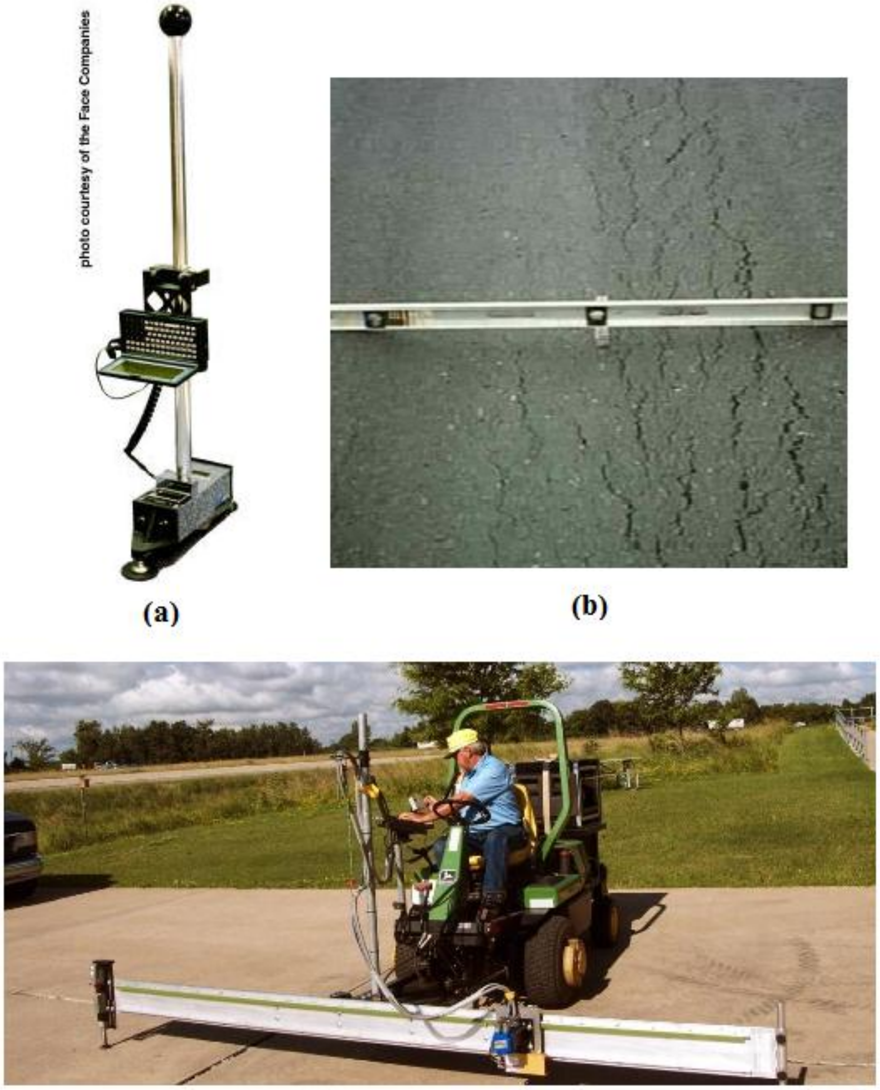

(a) (b)

(c)

Figure 2.16 Instruments for pavement rutting measurement: (a) Dipstick (b) Six foot straight edge (c) Automated laser profile system (MnROAD 2011)

2.3 Hydroplaning-related Measurements

2.3.1 Water Film Depth Measurement Approaches

The measurement of water film depth during storm event is important for the development of hydroplaning prediction models. Table 2.7 summarizes the current researches on water film depth measurement. Figure 2.17 shows the relevant instruments for water film depth measurement.

Table 2.7 Summary of Water Film Depth Measurement

Source	Equipment	Description	Accuracy
Ross and Russam (1968)	Steel bar with studs	Use a steel bar placed on the road surface with studs set at intervals. The water depth was manually read from this bar.	0.05 mm
Gallawaty et al. (1971)	Leupold & Stevens point-gauge	Use a manually operated Leupold & Stevens point-gauge to take measurements of the water depth from a datum line.	0.2mm
Kulakowski and Douglas (1990)	Electric probe (Figure 2.18a)	When the probe is lowered, a circuit is closed, and when the probe contact with water, the electric motor stops and a micrometer reading is taken. By lowering the probe further until it strikes the pavement surface, a second reading can be taken, and the water depth can be calculated.	0.025mm
Coiret (2005)	Limnimeter (Figure 2.18b)	The device uses a pair of metal needles lowered automatically until the water surface closes the circuit between them.	N/A
Roe et al. (1997)	Twin metal wire probe	The resistance measured between the two probe wires, which are at a fixed distance apart, could be used to calculate the water depth.	N/A
Coiret (2005)	Light ray	A light ray is directed onto a wet pavement and analyzed after having been altered in the liquid medium and retro-reflected by the road surfacing.	Reliable from 1mm to 5 mm
Campbell Scientific INC, (2007)	Vaisala remote road surface state sensor (Figure 2.18c)	Use reflection-based water detection principle to measure the presence of water or ice on a pavement.	Reliable from 0 to 2 mm
Vogt and Fevrier (2013)	Electric prod (Figure 2.18d)	When the measurement prod has contact with the water film of the road, an electric circuit is closed, and an LED sign is shining. The digital display shows the measured water depth.	0.1mm

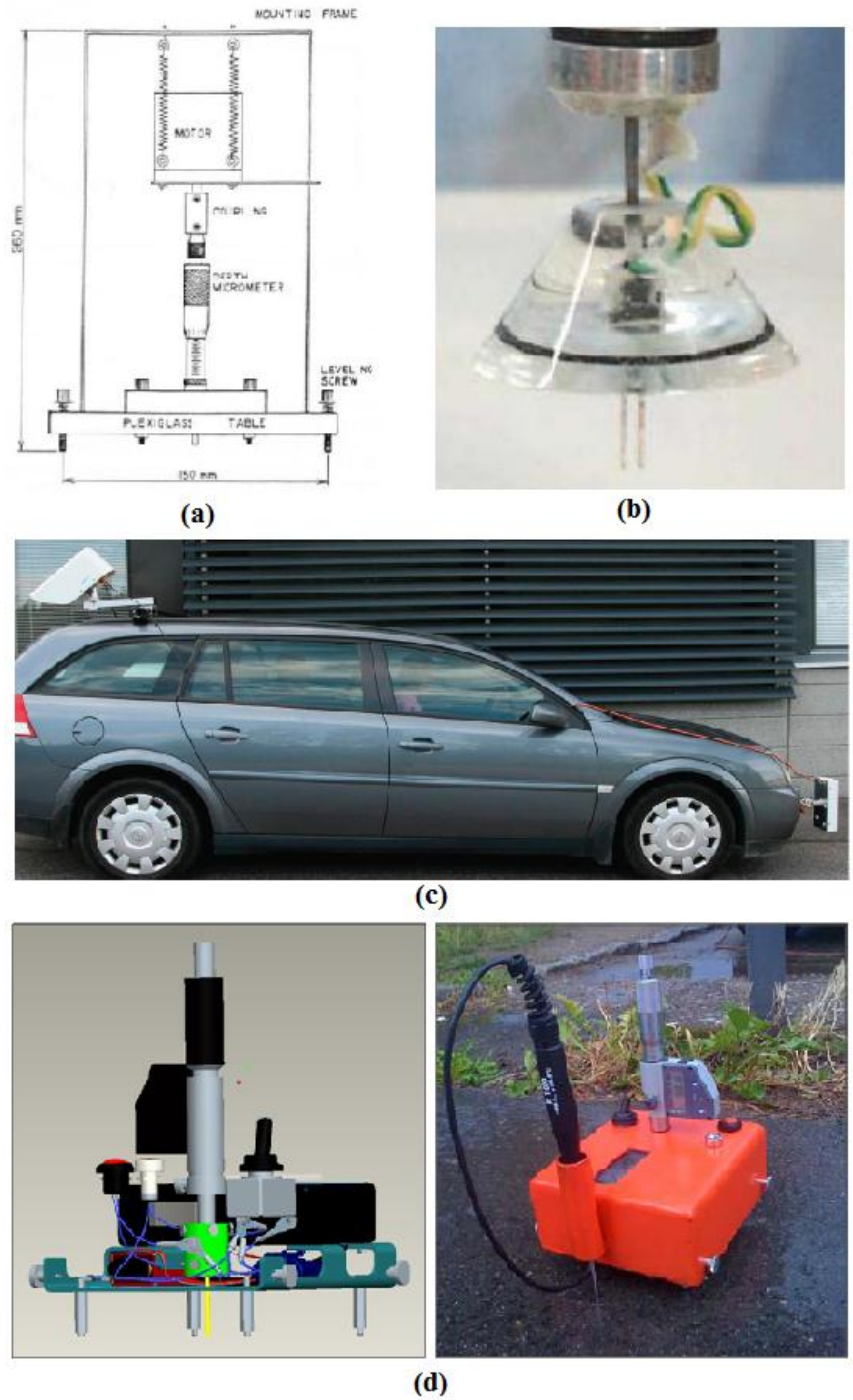

(a) (b)

(c)

(d)

Figure 2.17 Equipment for water for depth measurement: (a) Electric probe (Kulakowski 1990) (b) Limnimeter probe (Coiret 2005) (c) Vaisala condition patrol DSP310 (Campbell Scientific INC 2007) (d) Electric prod with digital display (Vogt 2013)

2.3.2 Hydroplaning Speed Estimation Approaches

Hydroplaning speed measurement is important for both the development of empirical hydroplaning models and the verification of analytical hydroplaning models. Past studies indicated the methods for hydroplaning speed estimation can be classified into three categories: field test, hydroplaning simulation by Finite Element Method (FEM), and crash data.

Gallaway's (1979) hydroplaning speed model is an empirical model, and developed based on the field friction test data. The tests were performed with the TTI research trailer. Combined with the capability of measuring ASTM E274 locked-wheel skid numbers, the tests can measure test wheel rotational speed referenced to a fifth wheel on the TTI research trailer. When the horizontal force for a given speed is not dependent on whether the vehicle is accelerating or decelerating through the speed, or traveling at a constant speed, the speed of fifth wheel is considered as hydroplaning speed.

Kumar and FWA (2009) presented a verified hydroplaning simulation model for rib tire and the solutions for hydroplaning speeds using the finite element method. The hydroplaning characteristics of the standard ASTM E501 rib tire were studied for different tire groove widths, spacing and depths at fixed water depth of 5 mm.

Jayasooriya's study (2014) captured the hydroplaning speed from the crash database. In this research the hydroplaning crash data was extracted from five databases provided by Florida Department Of Transportation (FDOT), which are Crash analysis and reporting system database, Pavement condition survey database, Geographical information system database, Vehicle passenger and driver information database, and Police long-form database.

2.4 Hydroplaning Prediction Models

Substantial efforts has been devoted to the development of formulas and criteria to identify the precise speed at which hydroplaning occurs. The most common approaches have been used to calculate the critical speed required for dynamic hydroplaning. Some of these equations are simple relationships which define the hydroplaning speed as a function of one or two variables. Others are considerably more complex. As might be expected, the task of predicting when hydroplaning will occur, or of identifying a particular wet-weather accident as a hydroplaning incident, is rather difficult and involves in a substantial degree of uncertainty.

2.4.1 NASA Hydroplaning Model

In 1962 the NASA Langley Research Center published a formula for hydroplaning based on the hydrodynamic forces experienced by an aircraft tire (Horne 1962). Equation 2.12 was derived by balancing the vehicle down force with the hydrodynamic up force. This formula is still used today as an indicator of the relationship between tire pressure and hydroplaning speed. The average water film depth is limited to 7.62 mm in this model.

$$V_P = K\sqrt{P} \tag{2.12}$$

Where, V_p: Tire hydroplaning speed, mph; K: Constant dependant on fluid and flow dynamics determined from experimental data for specific tire and road combinations; P: Tire inflation pressure, psi.

2.4.2 Road Research Laboratory (RRL) Model

This method was developed by Road Research Laboratory (RRL) in 1968. The 2yr return period storm with duration of 5min is recommended for obtaining rainfall intensity.

Equation 2.13 indicates the water film depth calculation, and this method did not include any allowance for pavement texture depth. It is recommended that maximum WFD should be no more than 4 mm (NAASRA 1974, Russam 1968).

$$d = 0.046 \frac{\left(L_f I\right)^{\frac{1}{2}}}{S_f^{\frac{1}{5}}} \tag{2.13}$$

Where, d: Depth of flow or water film thickness at the end of the flow path, mm; L_f: Length of flow path, m; I: Rainfall intensity, mm/hr; S_f: Flow path slop, m/m.

2.4.3 Gallaway Model

Gallaway B. M. et al developed an empirical method in 1979 on hydroplaning prediction for the US Department of Transportation. The method was outlined in the Texas Department of Transportation Hydraulic Design Manual, as described by Equations 2.14 to 2.18. The local rainfall intensity and road geometry is used in Equation 2.18 to obtain the water film depth. This depth is then used to predict the hydroplaning velocity (Equation 2.14) (Gallaway, 1979).

$$V = 0.9143SD^{0.04}P^{0.3}(TD + 0.794)^{0.06}A \tag{2.14}$$

$$SD = \left(\frac{W_d - W_w}{W_d}\right)100 \tag{2.15}$$

$$A = \frac{12.639}{WFD^{0.06}} + 3.507 \tag{2.16}$$

$$A = \left[\frac{22.351}{WFD^{0.06}} - 4.97\right] \cdot TXD^{0.14} \tag{2.17}$$

$$WFD = z\left\{\frac{TXD^{0.11}L^{0.43}I^{0.59}}{S^{0.42}}\right\} - TXD \tag{2.18}$$

Where, V: Vehicle speed at which aquaplaning occurs, km/hr; SD: Spin down speed (10%at initiation of aquaplaning); W_d: Rotational velocity of wheel on dry surface; W_w: Rotational velocity of wheel after spindown due to contact with flooded surfaces; P: Tire pressure, Kpa (165Kpa recommended design value); TD: Tire tread depth, mm (0.5mm recommended design value); A: The greater of the equation 16 and 17; TXD: Pavement texture depth, mm (0.5mm recommended); WFD: Water film depth on pavement surface, mm; z: 0.01485 (Constant); L: Pavement flow path length, m; I: Rainfall intensity, mm/hr; S: Pavement cross slope, m/m.

2.4.4 Sight Distance Model

Ivey et al (1975) proposed an empirical relationship between rainfall intensity, driver visibility and speed. The Equation 2.19 is usually rearranged to give the rainfall intensity for a specific design speed. Sight distance may also be substituted in form a geometric design manual such as AASHTO, and the maximum rainfall intensity calculated for hydroplaning WFD calculations.

$$S_v = \frac{2000}{i^{0.68}} \cdot \frac{40}{V_i} \tag{2.19}$$

Where S_v: Sight distance, ft; i: Rainfall intensity, in/hr; V_i: Vehicle velocity, m/hr.

2.4.5 PAVDRN Model

PAVDRN is a computer program that was developed by the University of Pennsylvania in 1998 with funding from the National Cooperative Highway Research Program (AASHTO, 2004). It uses a one-dimensional steady state form of the kinematic wave equation (Equation 2.20) to calculate the water film depth. The program also uses a condensation of formulas to determine a relationship between velocity at which hydroplaning initiates and WFD, as Equation 2.23 shows.

$$WFD = \left[\frac{nLI}{105.425S^{0.5}}\right]^{0.6} - MTD \tag{2.20}$$

$$n = \frac{1.49S^{0.306}}{N_R^{0.424}}\ (Porous\ asphalt) \tag{2.21}$$

$$N_R = \frac{q}{v} \tag{2.22}$$

$$HPS = 26.04WFD^{-0.259}\ (WFD\ (in) <\ 0.095in\ or\ 2.4mm) \tag{2.23}$$

Where, WFD: Water Film Depth, mm; MTD: Mean Texture Depth, mm; S: Slope, m/m; I: Rainfall intensity, mm/hr; f: Infiltration rate or permeability of pavement, mm/hr; n: Manning’s roughness coefficient; N_R: Reynold’s number; q: Quantity of flow per unit width, m^3/s/m; v: Kinematic viscosity of water; HPS: Hydroplaning Speed, km/h.

2.4.6 University of South Florida (USF) Model

The USF model is an analytical hydroplaning prediction model developed at the University of South Florida. The method was developed based on Ong and Fwa's comprehensive numerical prediction, shown in Equation 2.24. The USF model can be used to predict the hydroplaning speeds for different light vehicles that employ tires compatible with the locked-wheel tester tires (Gunaratne 2012).

$$v_p = W^{0.2} \times {P_t}^{0.5} \times [(\frac{0.82}{WFD^{0.06}}) + 0.49] \tag{2.24}$$

Where, WFD: Water film depth, mm; v_p: Hydroplaning speed, km/h; P_t: Inflation pressure, Kpa; W: Wheel load, N.

2.4.7 Browne's Hydroplaning Model

Browne 1975 developed a model to describe the minimum hydroplaning speed for a pavement surface with slight micro-texture. Equation 2.25 is the formula of this method for the hydroplaning speed estimation. However, this formula is not applicable to dynamic hydroplaning.

$$V_H \geq \frac{L}{\Delta T_{sf}} \tag{2.25}$$

Where, V_H: The minimum viscous hydroplaning speed, km/h; L: The length of the tire footprint region, m; ΔT_{sf}: The time required for sufficient reduction of the fluid film for contact between the tread rubber and the pavement asperities.

2.4.8 Yang's Hydroplaning Model

Yang (1972) has proposed an analytical equation to define hydroplaning as part of an effort to develop design criteria for runway pavement grooving. The underlying principle for Equation 2.26 is that hydroplaning will occur when the water escape velocity due to an external force, the tire pressure, is less than the speed at which the surface water travels sideways.

$$cp^{1/2} = \frac{\pi a/4}{2b/v} \tag{2.26}$$

Where, c: A constant; p: The tire inflation pressure, lbf/in^2; a: The width of the tire footprint region, in; b: The length of the tire footprint region, in; v: The vehicle velocity, in/sec.

2.5 Summary

This chapter firstly summarizes pioneering studies on factors affecting hydroplaning including surface texture, pavement geometry features, and pavement rutting. These factors can be measured using static or dynamic methods with different accuracies. For the network-level survey purpose, these factors would be continuously measured using DHDV at highway speeds, including texture data, cross slope, longitudinal grade, horizontal radius curves, and rutting depth and width.

The existing methods for water film depth calculation are presented. Past studies indicates that the risk of hydroplaning increases with the exaltation of the water film depth which is dependent on surface texture properties, flow path slope, flow path length, rainfall intensity, and pavement surface type. The development of formulas and models to estimate water film depth and the onset of dynamic hydroplaning for pneumatic tires has been going on for approximately 50 years. However, some important intervening factors on water film depth calculation has been ignored in these models, such as effects of large slope and pavement rutting on water film depth.

Therefore the current hydroplaning speed prediction models are malfunctioned on pavement sections with horizontal curve, large longitudinal slope, or rutting. In addition, there were few research studies conducted on detecting and identifying hydroplaning risk sections in a network level pavement safety survey. This is primarily due to two facts: 1) that it is difficult to acquire the high-quality texture and geometry data which are served as the basis for hydroplaning study; 2) that the existing hydroplaning speed prediction models might be malfunctioned on the irregular pavement sections e.g. pavements with large slopes or long rutting track.

CHAPTER 3. EVALUATION OF WATER FILM DEPTH AND HYDROPLANING SPEED PREDICTION MODELS

3.1 Validation of Water Film Depth Models

Currently the water film depth prediction models can be classified into two categories: empirical model developed from field test data and analytical model deduced from FEM simulation methods (Anderson 1998). This section attempts to estimate the water film depths under various models during storm event. Finally, the comparisons are made between the collected and estimated WFDs so that the better and much reliable models for WFD calculation can be determined.

3.1.1 Water Film Depth Models

3.1.1.1 Existing Water Film Depth Models

Four types of water film depth estimation models are examined in this study, including empirical form of PAVDRN model, Gallaway Model, NZ Modified Equation, and analytical form of PAVDRN model, as shown in Table 3.1. The definition of the variables in these models, such as water film depth (water film thickness), thickness of total flow, and mean texture depth are illustrated in Figure 3.1.

Table 3.1 Summary of Tested Water Film Depth Model

Source	Model Structure	Equation Form	Variables
Empirical form of PAVDRN	Empirical	$WFD = \frac{0.00372L^{0.519}I^{0.562}MTD^{0.125}}{S^{0.364}} - MTD$	I: Rainfall intensity (in/hr); MTD: Mean texture depth (in); L: Longest flow path length (ft); S: Drainage slope (ft/ft); n: Manning's roughness coefficient.
Gallaway	Analytical	$WFD = 0.0034\left(\frac{MTD^{0.11}L^{0.43}I^{0.59}}{S^{0.42}}\right) - MTD$	
NZ modified Equation	Empirical	$WFD = \frac{0.0502L^{0.316}I^{0.2712}}{S^{0.3}} - MTD$	
Analytical form of PAVDRN	Analytical	$WFD = (\frac{nLI}{36.1S^{0.5}})^{0.6} - MTD$	

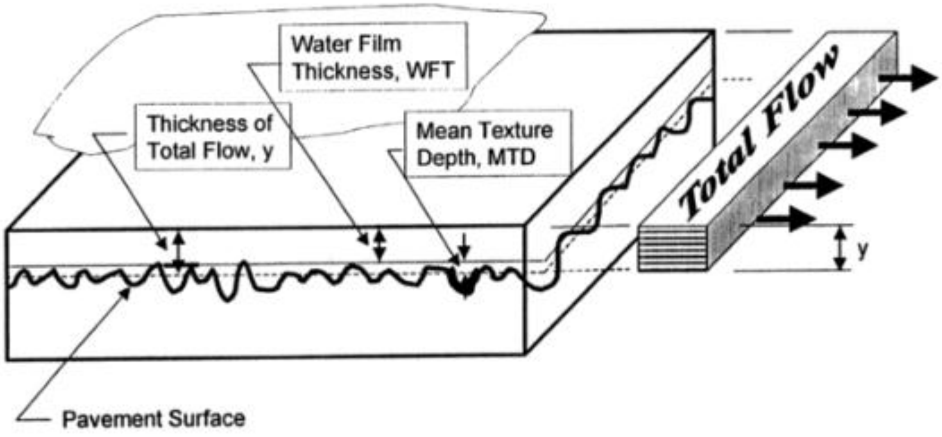

Figure 3.1 Definition of water film thickness, mean texture depth, and total flow in current hydroplaning prediction model (Anderson 1998)

3.1.1.2 Sensitive Analysis of WFD Models

Water film forms on the pavement surface during natural rainfall. Its thickness is related to the effectivity of pavement drainage and dimensions of flow path. Usually rainfall intensity, pavement texture, cross slope, and longitudinal grade are considered as the contributing factors on water film depth. The sensitive tests are provided in this section to verify the sensitivity of four WFD models to their variables. In this test the reference variable are assumed as follows:

- Rainfall Intensity: $'i' = 6in/hr$
- Texture Depth: $'MTD' = 0.06in$
- Cross Slope: $'Sc' = 2\%$
- Longitudinal grade: $'S_l' = 5$ %

The sensitivity of the WFD models to their variables are analyzed, as shown in Figure 3.2. The rainfall intensity, mean texture depth, cross slope and longitudinal grade are each varied by ± 25%, ± 50%, and ± 75% individually while maintaining the other variables at the reference value. The resulting change in WFD is calculated for rainfall intensity, MTD, cross slope and longitudinal grade. It can be seen that the resulting change in WFD is apparent along the increase of rainfall intensity, MTD, cross slope, and longitudinal grade. In the four WFD models, the water film depth increases with increase of rainfall intensity and longitudinal grade, while with decrease of MTD and cross slope. The rainfall intensity is most sensitive in analytical PAVDRN model, and followed by NZ modified model, empirical PAVDRN model, and Gallaway model, as Figure 3.2a shows. Figure 3.2b shows that there is no obvious difference between four WFD models for the sensitivity of the WFDs to MTD. In Figure 3.2c, the NZ modified model is more sensitive in cross slope than the other models. However, the sensitivity of four models to longitudinal grade is not obvious, as Figure 3.2d shows.

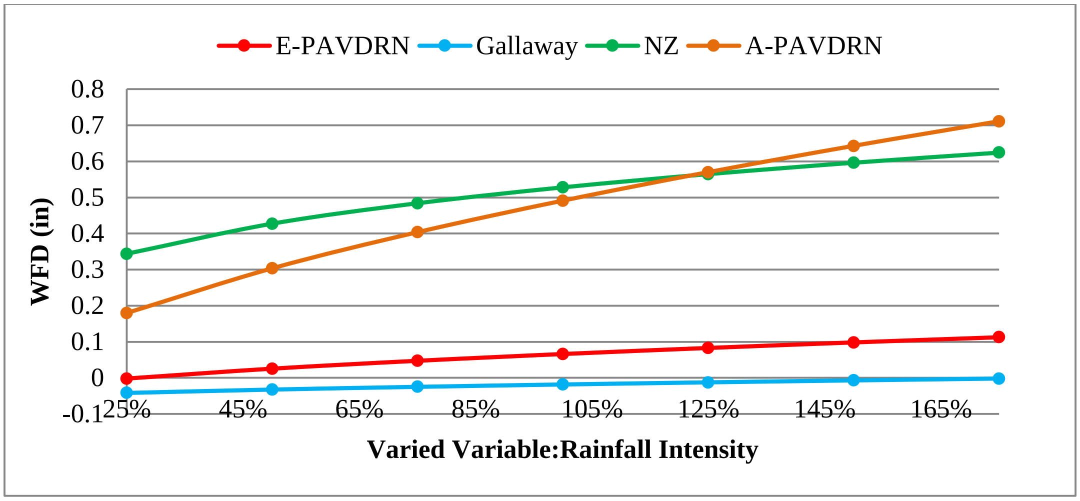
E-PAVDRN
Gallaway
NZ
A-PAVDRN
0.8
0.7
0.6
0.5
0.4
0.3
0.2
0.1
0
-0.1
WFD (in)
25%
45%
65%
85%
105%
125%
145%
165%
Varied Variable:Rainfall Intensity

(a)

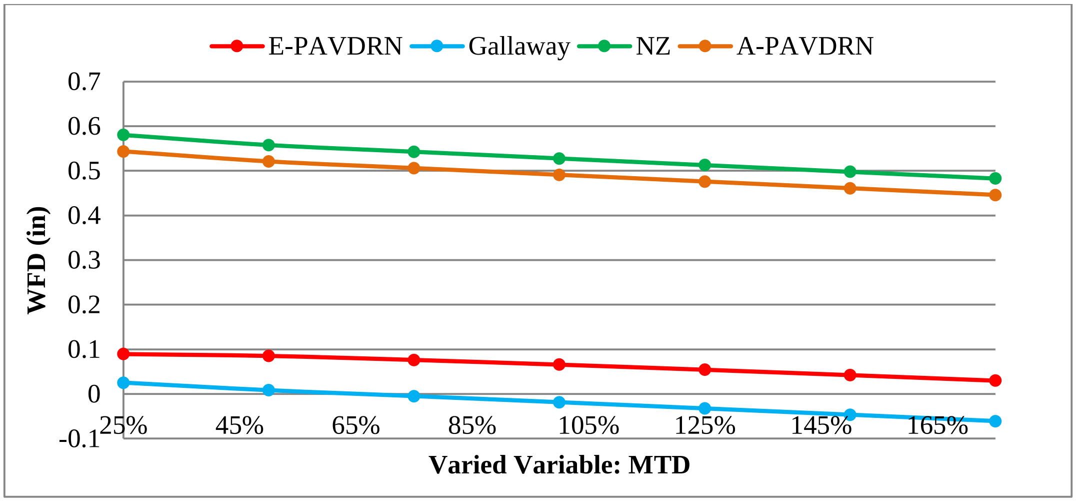
E-PAVDRN
Gallaway
NZ
A-PAVDRN
0.7
0.6
0.5
0.4
0.3
0.2
0.1
0
-0.1
WFD (in)
25%
45%
65%
85%
105%
125%
145%
165%
Varied Variable: MTD

(b)

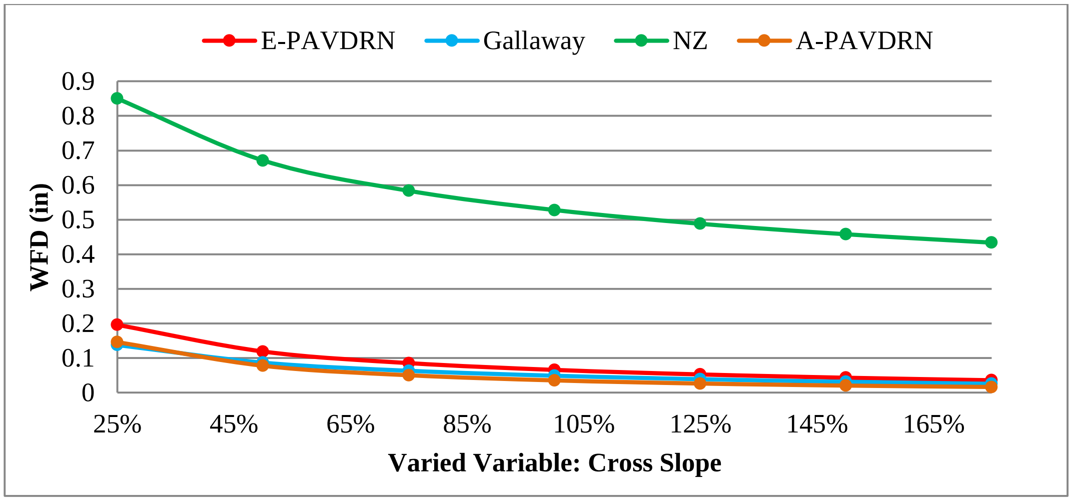
E-PAVDRN
Gallaway
NZ
A-PAVDRN
0.9
0.8
0.7
0.6
0.5
0.4
0.3
0.2
0.1
0
WFD (in)
25%
45%
65%
85%
105%
125%
145%
165%
Varied Variable: Cross Slope

(c)

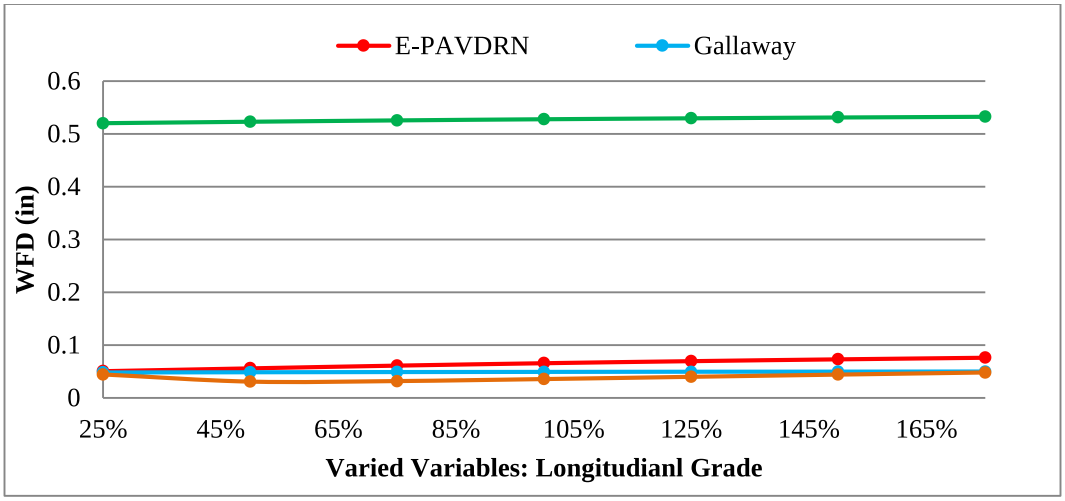

(d)

Figure 3.2 Sensitivity tests for four WFD models to their variables

3.1.2 Data Collection Instruments

Figure 3 shows the general principle of the rainfall intensity and actual WFD test in this study. During the storm events, the rain gauge is placed on the test site to record rainfall intensity (water volume on the rain gauge is recorded every five minutes), meanwhile the eTape Liquid Level Sensor linked with FLUKE 289 RMS Multi-meter is applied to measure the water film depth on the pavement surface (the WFD is recorded every 5 second). In order to avoid the equipment wetting by rain, the eTape Liquid Level Sensor and FLUKE 289 RMS Multi-meter are fixed in the box, and a small hole on the box bottom make the eTape sensor touching the pavement surface. After storm events, the WFD related pavement features including pavement texture and pavement slope are measured by LS-40 Surface Texture Scanner and SurPro3500 walking profiler respectively.

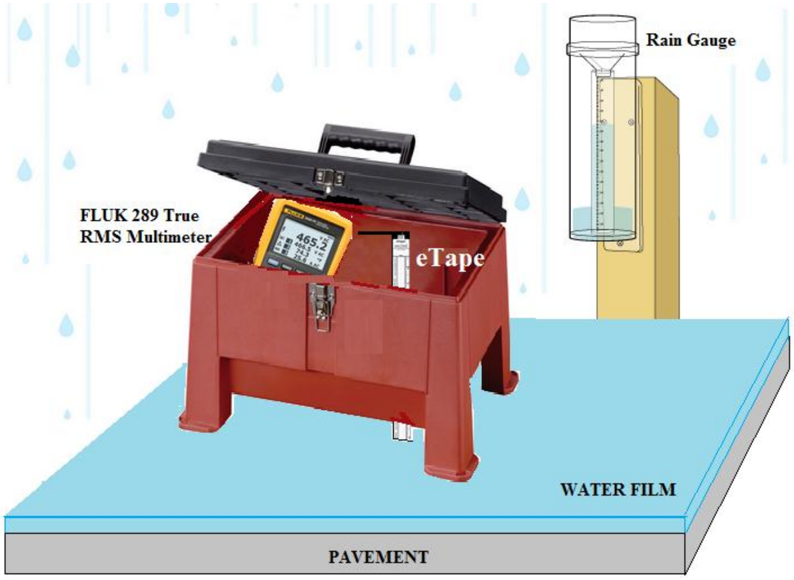

Figure 3.3 Water film depth and rainfall intensity measurement

3.1.2.1 Rainfall Intensity and WFD Test

A rain gauge, as shown in Figure 3.4, is a type of instrument used by meteorologists and hydrologists to gather and measure the amount of liquid precipitation over a set period of time (Wikipedia 2015). The standard plastic rain gauge used in this study has four inch outer cylinder for rain collection, and 0.98 inch inner cylinder to fill the rain. After the inner cylinder is filled, the amount insider it is discarded, then filled with the remaining rainfall in the outer cylinder until all the fluid in the outer cylinder is gone, adding to the overall total until the outer cylinder is empty. In this study the water volume in rain gauge is recorded every five minutes, and the unit in millimeter per five minutes is transferred to the unit in millimeter per hour.

Figure 3.4 Standard plastic rain gauge

eTape liquid level sensor is a solid-state sensor with a resistive output that varies with the level of fluid (MILONE 2015). It results in a change in resistance that corresponds to the distance from the top of the sensor to the surface of the fluid. The sensor's resistive output is inversely proportional to the height of the liquid. It does away with clunky mechanical floats, and easily interfaces with electronic control systems. The eTape liquid level sensor combine with the FLUKE 289 true RMS multi-meter (FLUKE 2015), as Figure 3.5 shows, can measure water film depth, and the data is recorded every 5 seconds.

Figure 3.5 eTape liquid level sensor and FLUKE 289 true RMS multi-meter

After the storm event, the corresponding texture data and flow path slope are measured by LS-40 Surface Texture Analyzer and SurPro3500 walking profiler, respectively.

3.1.2.2 LS-40 Surface Texture Analyzer

LS-40 Surface Texture Scanner (Figure 3.6) is a high resolution surface measurement and analysis device. It scans a 4.25” by 6” or 10” areas and produces a high resolution digital surface structure with an intensity image and a surface depth related range image. Its 3D graphic display allows users to view detailed structure from different angles. LS-40 provides accurate and stable texture MPD by processing thousands of profiles over the entire surface (Table 3.2), with optional processing modules of measuring other surface features (Bergstrom 2001).

Figure 3.6 LS-40 Surface Texture Analyzer in operation

Table 3.2 LS-40 Surface Texture Analyzer Specification

Scan area	**4.25” x 4” (108mm x 101mm), LS-40-6 model 4.25” x10” (108mm x 254 mm), LS-40-12 model**
No. of	Up to 5120 profile lines in a single measurement
Data/scan	2048 samples per scan line
X Y	0.002” (0.052mm) or 0.004” (0.1mm) for both x and y.
Z Resolution	0.01 mm/ 0.0004 inch at depth range of 0.75” (19.05mm)
Accuracy	0.002” (0.05 mm)
Test Time	85 profiles per second. 25 second for a full scan of 2048 profiles
Power	Battery operation (3 hour)
Dimension	13”(381mm)W x 8.5”(165mm)D x 10”(254mm)H , model 6 18”(457mm)W x 8.5”(165mm)D x 10”(254mm)H , model 12
Function:	Primary function: Surface texture analysis
	Optional functions: 1) Crack or concrete joint faulting measurement; 2) Aggregate shape and surface feature measurement
Controller	Controlled and processed by a laptop computer for virtually unlimited data

3.1.2.3 SurPro500 Walking Profiler

The SurPro3500 (Figure 3.7) is a rolling surface profiler intended for a wide range of applications on roads, structures, runways and floors. It is inclinometer-based profiling devices and can automatically collect runway unfiltered true elevation profiles with high accuracy and repeatability at speeds up to 4 km/h (International Cybernetics 2015). As one of the most advanced walking surface profiler, it is widely accepted as the industry reference ("gold") profiling device. It has co-linear wheels (no side wheels or outrigger) which enable accurate profiling in wheel ruts and easy to steer following chalk line. Its wheel spacing of 250 mm, 12" and 300 mm support several ASTM Standards. SurPro3500 saves profiling data in several widely used profiling data formats including PPF, ERD and PRO formats.

Figure 3.7 SurPro3500 walking profiler in operation

3.1.3 Evaluation of WFD Estimation Models

3.1.3.1 Test Sites

Six test sites, located in Stillwater Oklahoma, are chosen for WFD model evaluation, as shown in Figure 3.8, among which three are asphalt pavements and the other three are concrete pavements. Pavement texture properties are illustrated in Figure 3.9. In addition, pavement type, site geometry feature, drainage facility, and pavement condition for these six test sites are summarized in Table 3.3.

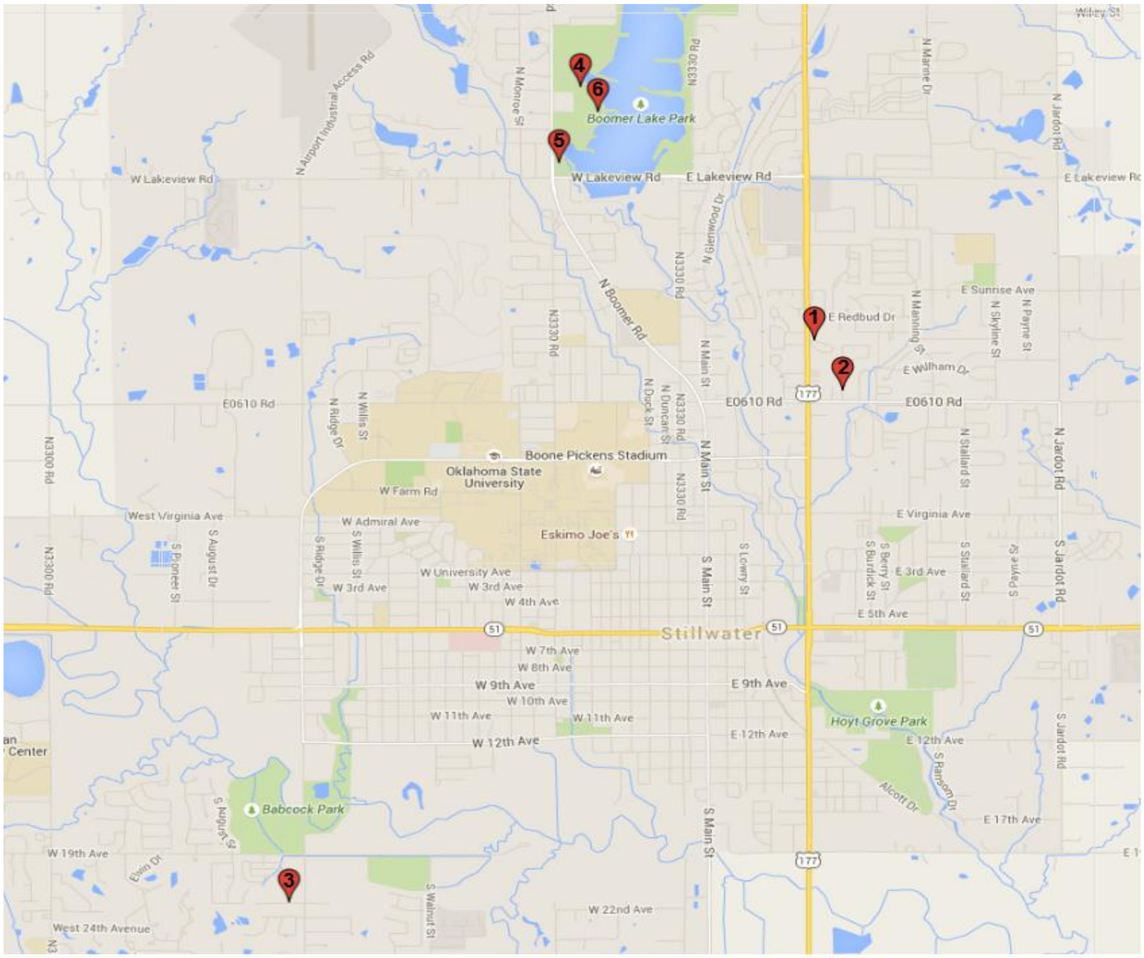

Figure 3.8 Six test sites in google map

Table 3.3 Summary of the Six Test Sites

Test Site	Pavement Type	Flat/Sloping	Drainage Facility	Pavement Condition
1	Asphalt Pavement	Sloping	Ditch	Good
2	Asphalt Pavement	Sloping	Gutter	Good
3	Asphalt Pavement	Flat	Ditch	Excellent
4	Concrete Pavement	Sloping	Gutter	Good
5	Concrete Pavement	Sloping	Gutter	Good
6	Concrete Pavement	Flat	Gutter	Good

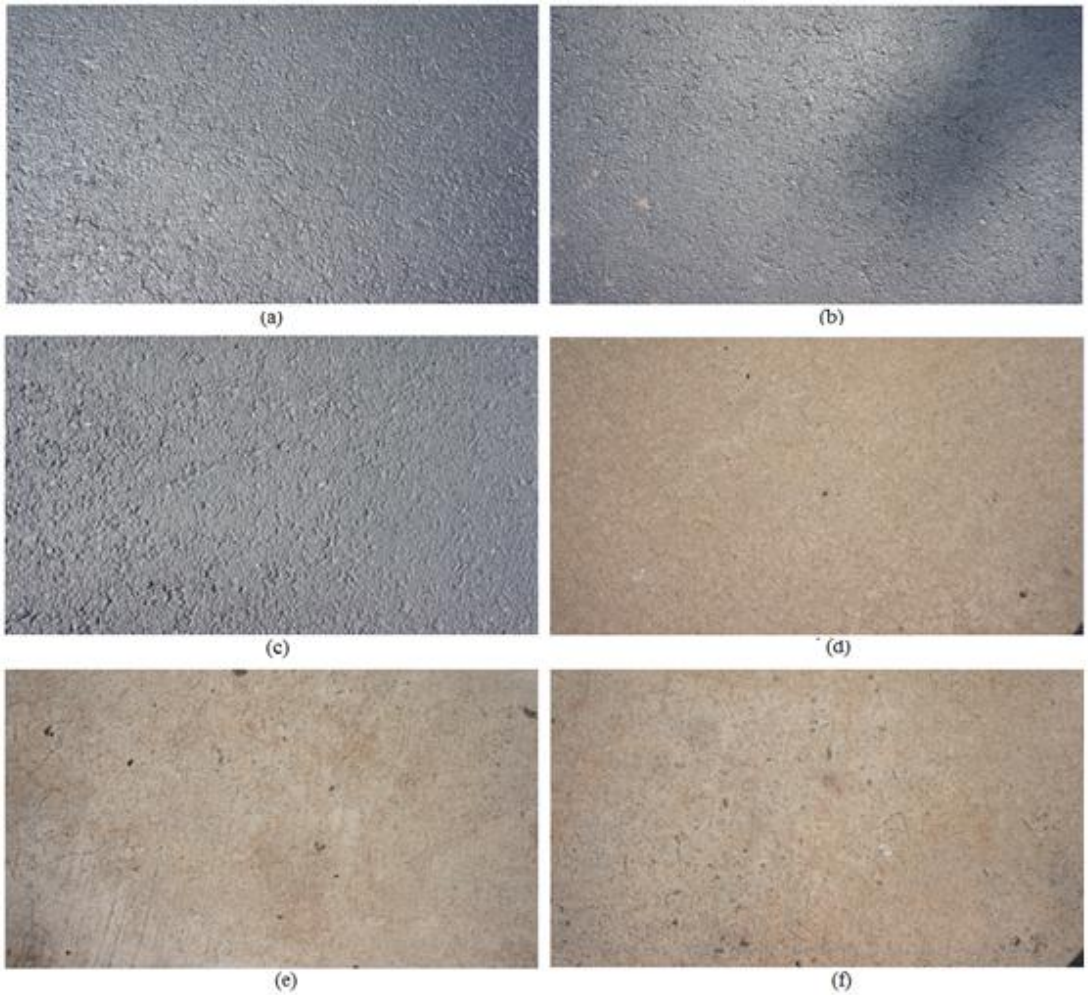

Figure 3.9 Pavement Texture of (a) Test Site 1; (b) Test Site 2; (c) Test Site 3; (d) Test Site 4; (e) Test Site 5; (f) Test Site 6

3.1.3.2 Data Collection and Analysis

The longitudinal grade and cross slope are collected by SurPro3500 walking profiler. Pavement texture data is collected with LS 40 Surface Texture Analyzer. The measured longitudinal grade, cross slope, MPD, and MTD at six test sites are summarized in Table 3.4. It can be seen that test sites 1, 2, and 4 have the large longitudinal grade, and the other test sites are located in relatively flat road section. At the six test sites, the measured cross slope is ranged from 1.083% to 3.734%; the calculated MTDs are around 1.2 mm for the flexible pavement test sites (test site 1, 2, and 3), and around 0.93 mm for the rigid pavement test sites (test site 4, 5, and 6).

Table 3.4 Summary of Pavement Characteristics at Six Test Sites

Test Site	1	2	3	4	5	6
Longitudinal grade (%)	4.4	3.072	0.063	4.385	-1.087	-1.942
Cross slope (%)	-1.083	2.415	-1.15	-3.302	-3.734	1.298
MPD (mm)	1.14	1.03	1.045	0.83	0.79	0.843
MTD (mm)	1.415	1.125	1.235	0.93	0.927	0.943

The water volume from the rain gauge is recorded every 5 minutes. For each test site, four set of data are recorded, and thereby 20 minutes rainfall data are collected in total. The water film depth variation in storm events is recorded by FLUKE 289 true RMS multi-meter. Figure 3.10a to Figure 3.10f shows the variation of water film depth and the rainfall intensity at six test sites. It can be seen that the peak water film depth sometimes appears after the peak rainfall intensity since the accumulated water on pavement surface cannot drain off immediately, which lead the offsets between peak water film depth and he peak rain fall intensity. By comparing the water film depths of flexible pavements (test sites #1, #2, and #3) and rigid pavements (test sites #4, #5, and #6), it can be found that the drainage of flexible pavement is better than rigid pavement due to the penetration of the flexible pavement.

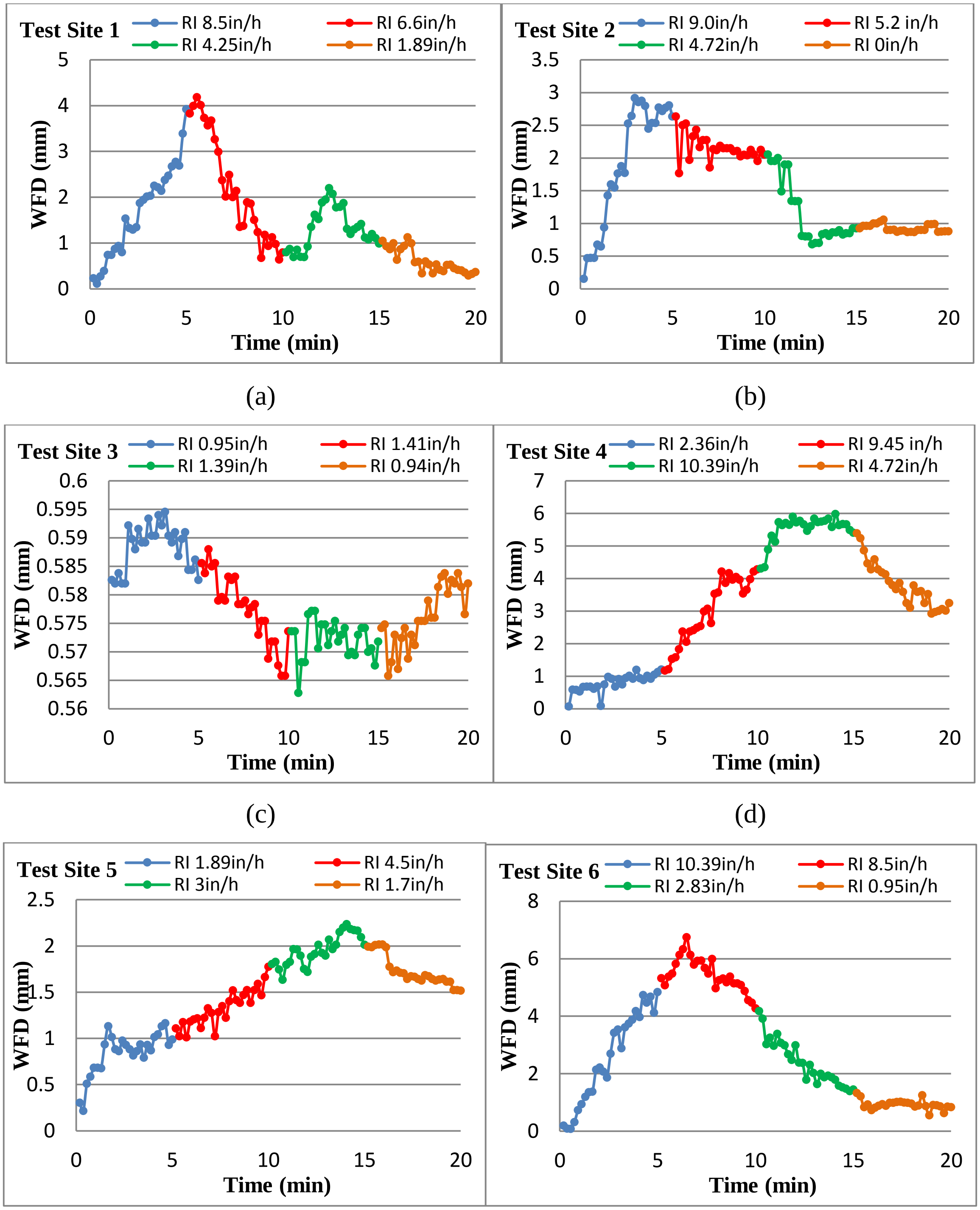

(a) (b)

(c) (d)

(e) (f)

Figure 3.10 Water film depth during storm events on (a) test site 1; (b) test site 2; (c) test site 3; (d) test site 4; (e) test site 5; (f) test site 6

3.1.3.3 Result Validation

In this case the measured cross slope, longitudinal grade, MTD, and rainfall intensity are loaded into the WFD prediction models, and the estimated water film depth can be obtained, as shown in Figure 3.11a to Figure 3.11f. The actual WFD measured by eTape liquid level sensor is marked by red line. By comparing the actual WFD with estimated WFDs from the four models, it can be found that the estimated WFD from Gallaway model and empirical PAVDRN model are closer to the ground truth than other models. Therefore, the Gallaway WFD estimation model is used for the following research in this study.

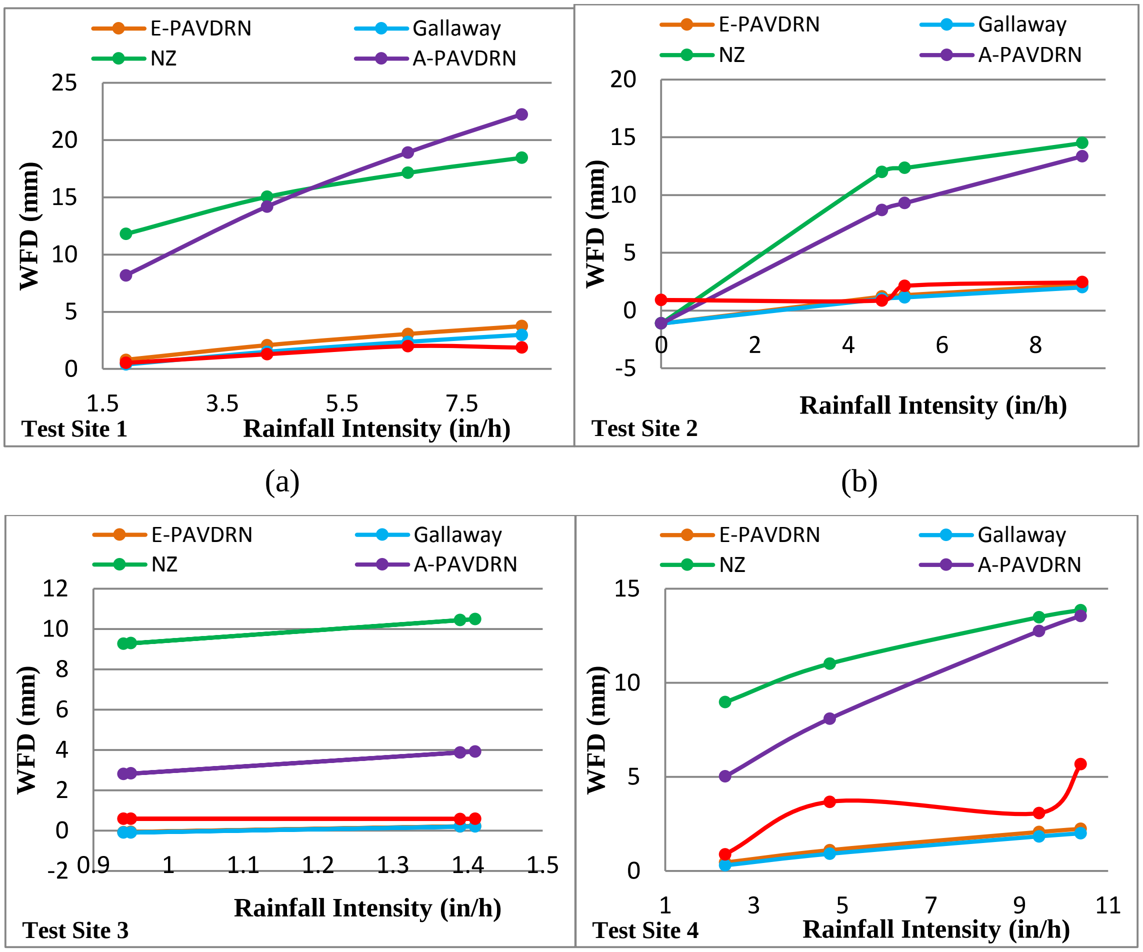

(a) (b)

(c) (d)

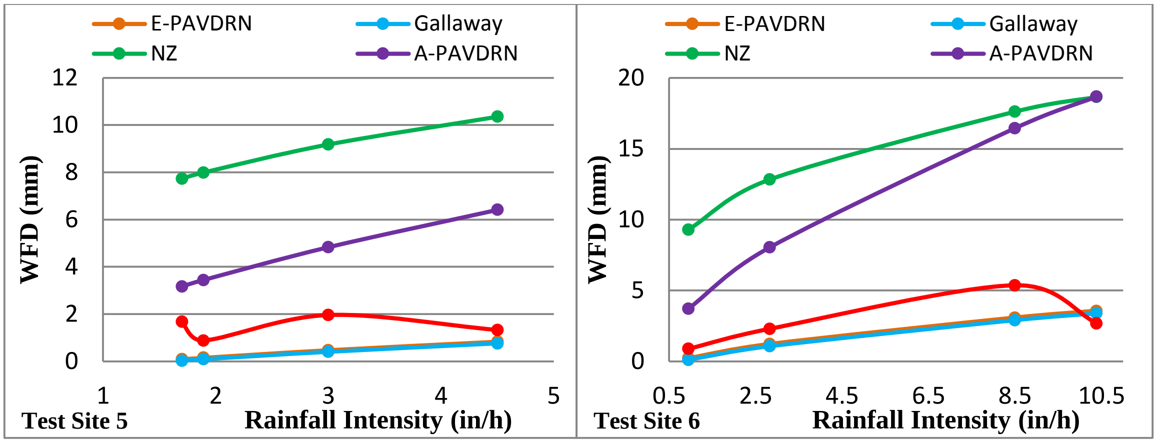

(e) (f)

Figure 3.11 Estimated WFD by models and ground truth by eTape at (a) test site 1; (b) test site 2; (c) test site 3; (d) test site 4; (e) test site 5; (f) test site 6

3.2 Validation of Hydroplaning Speed Prediction Models

The various empirical and analytical models have been developed to estimate pavement hydroplaning speed based on a series of factors. However, it is still unsolved problem to determine the most efficient model for hydroplaning speed prediction for researchers, in this paper the predicted hydroplaning speeds from different model would be validated with the ground truth so that the more reasonable and reliable model can be determined.

3.2.1 Hydroplaning Speed Prediction Models

3.2.1.1 Existing Hydroplaning Speed Prediction Models

The predicted hydroplaning speed is served as basis to evaluate the potential hydroplaning risks on test pavement section by comparing with the posted speed limit. As stated above, pavement hydroplaning speed is highly associated with water film depth, mean texture depth, tire inflation pressure, and tire tread depth. In this study four hydroplaning speed prediction models namely Agrawal model, PAVDRN model, Gallaway model, and USF model, are investigated, as summarized in Table 3.5.

Table 3.5 Summary of Hydroplaning Speed Models

Source	Model Structure	Equation Form	Variables
Agrawal	Empirical	$v_p = 37.5 + 5.28WFD^{-0.5}$	WFD: Water film depth (in); MTD: Mean texture depth (in); P_t: Inflation pressure (Kpa); SD: Spin down ratio; TD: Tire tread depth (in); W: Wheel load;
PAVDRN	Analytical	$v_p = 96.3WFD^{-0.259}, if\ WFD \geq 2.4mm$ Otherwise $v_p = 4.94A$ $A = Max.of \begin{cases} \left(\frac{12.64}{WFD^{0.06}}\right) + 3.507 \\ \frac{35.15}{WFD^{0.06}} - 7.817(0.0393MTD)^{0.1} \end{cases}$	
Gallaway	Analytical	$v_p = SD^{0.04}P_t^{0.3}(TD + 1)^{0.06}A$ $A = Max.of \begin{cases} \left(\frac{10.409}{WFD^{0.06}}\right) + 3.507 \\ [\left(\frac{28.952}{WFD^{0.06}}\right) - 7.817]MTD^{0.14} \end{cases}$	
USF - Gunaratne et al.	Empirical / Finite Element	$v_p = (W)^{0.2}(P_t)^{0.5}(\frac{0.82}{WFD^{0.06}} + 0.49)$	

3.2.1.2 *Sensitive Analysis of Hydroplaning Speed Prediction Models*

Since the water film depth is the key parameter to predict hydroplaning speed in these four models, the sensitive tests of the four models to water film depth are conducted. In the test the reference variables are assumed as follows:

- Texture Depth: $'MTD' = 0.06in$
- Inflation pressure: 'P_t' = 165 Kpa
- Wheel load: 'W' = 4800 N
- Water film depth: 'WFD'= 0.08 in

The texture depth, inflation pressure, and wheel load are assigned to the assumed values, and the WFD is assumed to be varied by ± 25%, ± 50%, and ± 75%, based on which the four hydroplaning speed prediction models are used to calculate the hydroplaning speeds, as shown in Figure 3.12. It can be seen that the resulting change in hydroplaning speed is apparent with the increase of WFD. Generally the estimated hydroplaning speeds decrease with the increase of WFD. Results also indicated that PAVDRN and Agrawal models are much sensitive to WFD than other two models.

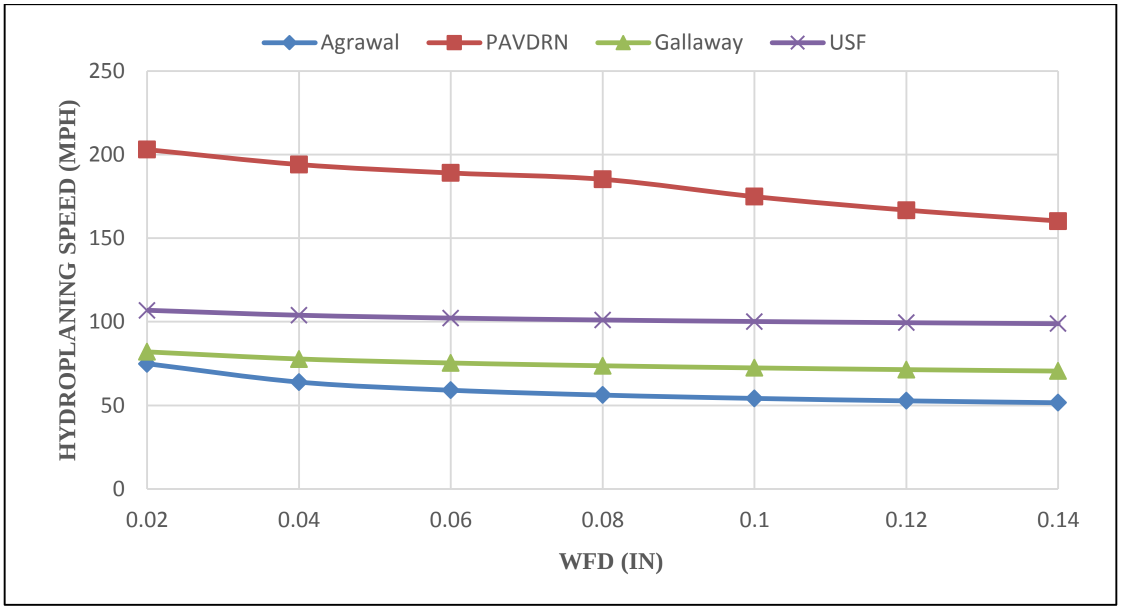

Figure 3.12 Sensitivity test for hydroplaning speed models to WFD

3.2.2 Data Collection Instruments

In order to validate the accuracy of hydroplaning speeds predicted from these four models, the Dynamic Friction Tester (DFT) is used as a reference device to measure the potential hydroplaning speeds. The DFT is a portable instrument to measure pavement surface friction as a function of speed and under various conditions (ASTM E1911), as Figure 3.13a shows. This instrument uses a disk that spins with its plane parallel to the test surface, and subsequently the friction coefficient and test speed are recorded. When the friction number is infinitely close to zero, the wheel speed at that time can be considered as hydroplaning speed. However, the maximum water thickness produced by this instrument is only 1mm, which cannot meet the requirement of the hydroplaning simulation test. Therefore a water pool with graduation is designed to maintain constant water film depth during test in Figure 3.13b. The collected data in this test includes friction coefficient, wheel speed, and fixed water film depth in the pool.

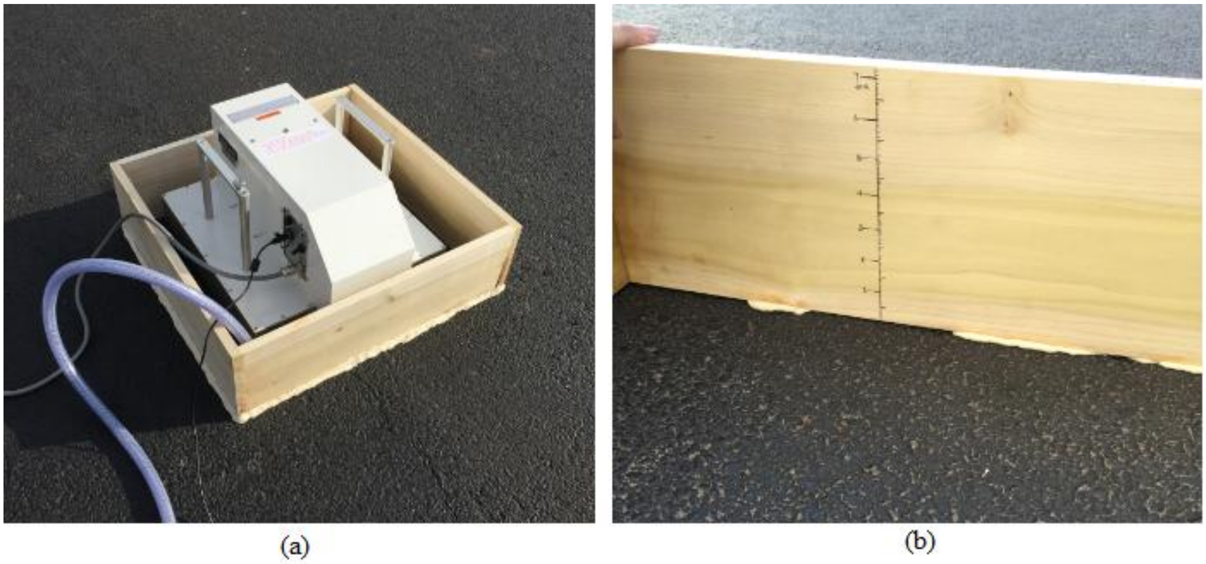

Figure 3.13 Hydroplaning speed verification: (a) DFT; (b) the pool with graduation

3.2.3 Evaluation of Hydroplaning Speed Prediction Models

3.2.3.1 Test Sites

Four test sites, located in Stillwater Oklahoma, are chosen for the predicted hydroplaning speed validation, as shown in Figure 3.14. The four test sites belong to asphalt pavements and have good condition. Table 3.6 summaries the road geometry features, pavement texture, cross slope, longitudinal grade, and fixed WFD at the four test sites.

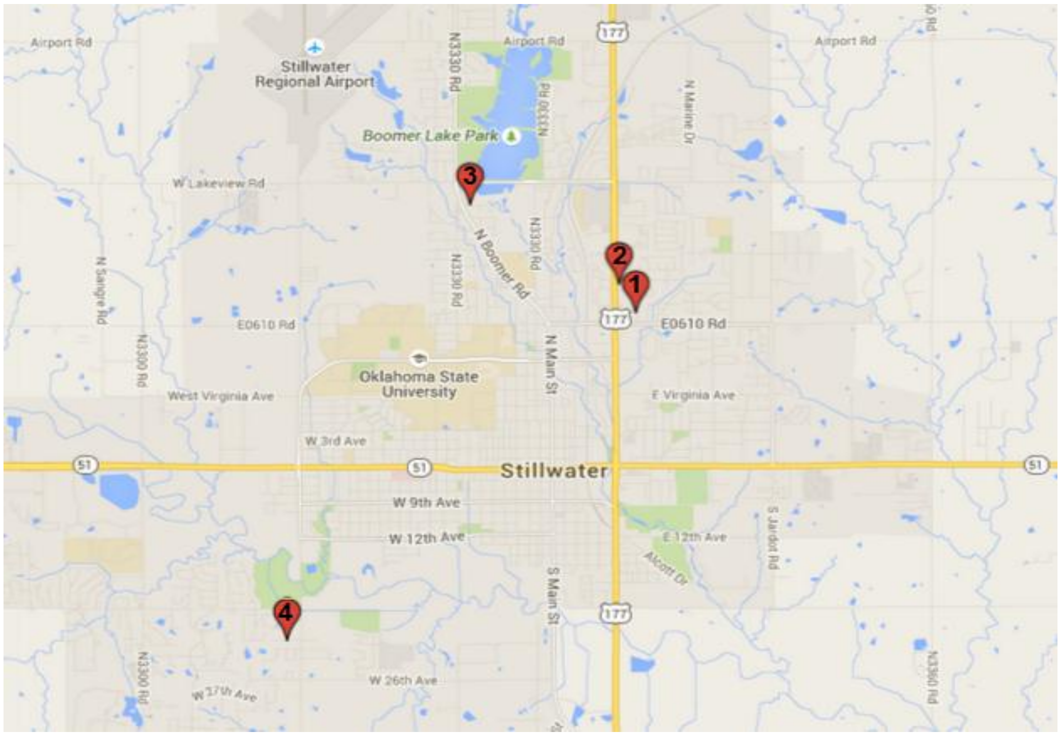

Figure 3.14 Locations of the DFT test sites

Table 3.6 Summary of Road Characteristics at Four Test Sites

DFT Test Site	1	2	3	4
Geometry	Curve/Flat	Straight/Slope	Straight/Flat	Straight/Slope
Fixed WFD (mm)	1.65	3.64	10.48	0.84
MTD (mm)	1.04	1.10	1.17	1.11
Cross Slope (%)	-2.11	-0.90	0.33	-3.54
Longitudinal Grade (%)	3.04	4.41	12.00	0.70

3.2.3.2 Data Collection and Analyses

Prior to field tests, the water should be poured into the built-up pool and make sure the test area are totally wet, and subsequently the DFT is used on wetted pavements to measure the dynamic friction number at four test sites, as shown Figure 3.15. Generally the moment of friction coefficient that is infinitely close to zero can be considered as the time of occurrence of hydroplaning risks, and the corresponding test speed for occurrence of hydroplaning risk is taken as hydroplaning speed, which is marked with red points in Figure 3.15. In Figure 3.15, it can be observed that the measured hydroplaning speed at four test sites are 84.98 km/h, 80.97 km/h, 68.99 km/h, and 91.98 km/h, respectively.

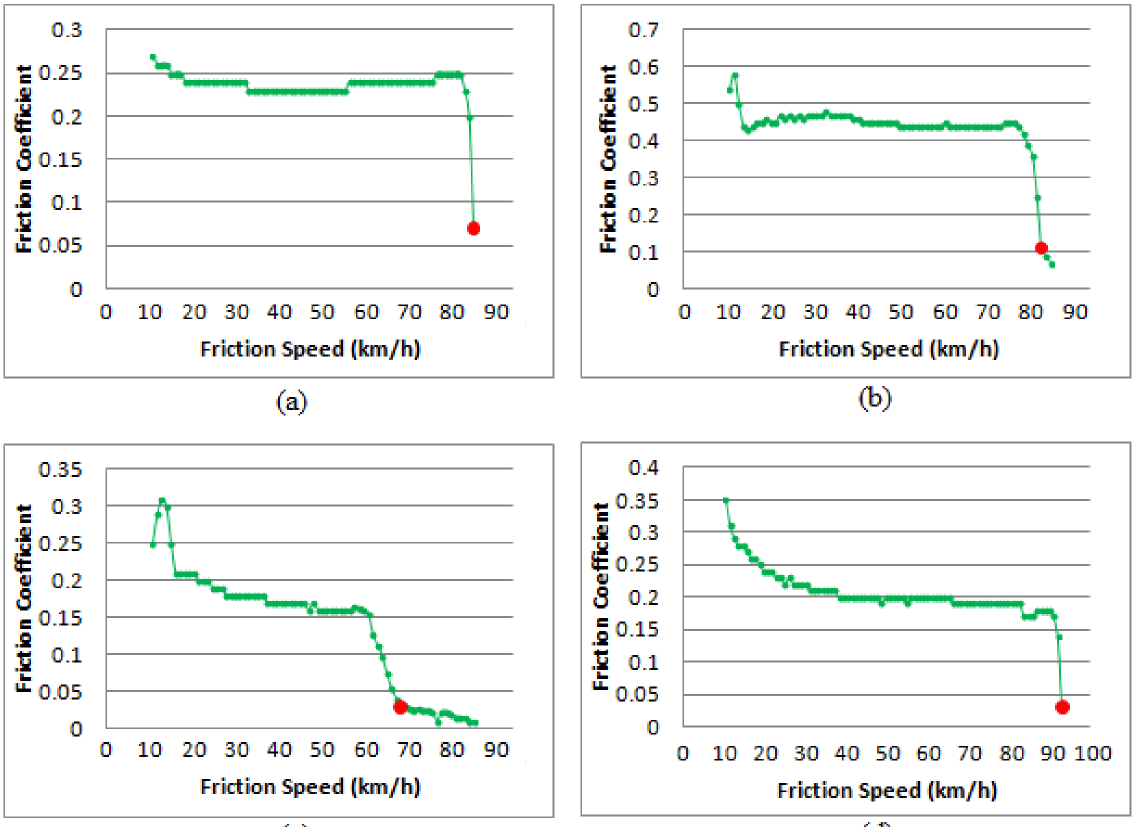

(a) (b)

(c) (d)

Figure 3.15 DFT test results for: (a) test site 1; (b) test site 2; (c) test site 3; (d) test site 4

3.2.3.3 *Results Validation*

Once the measured WFD and MTD are incorporated into the four hydroplaning speed prediction models, the hydroplaning speeds can be estimated, as given in Table 3.7. In this case the actual hydroplaning speed is measured by DFT and is given in Table 3.7 as well. By comparing the ground truth with the estimated hydroplaning speeds (Figure 3.16), it can be seen that the estimated hydroplaning speeds from the Gallaway and USF models are much closer to the ground truth than that from other two models. Therefore, in this study the Gallaway and USF models are selected for the following hydroplaning speed prediction.

Table 3.7 Hydroplaning Speeds from Predictive Models and DFT

Hydroplaning Speed (km/h)	Site #1	Site #2	Site #3	Site #4
Agrawal Model	58.21608	51.44762	45.71997	66.53423
PAVDRN Model	188.9017	159.277	121.1169	232.8571
Gallaway Model	71.01632	67.27121	62.36373	75.5103
USF Model	101.9068	98.77193	94.8078	104.702
DFT Test	84.98	80.97	68.99	91.98

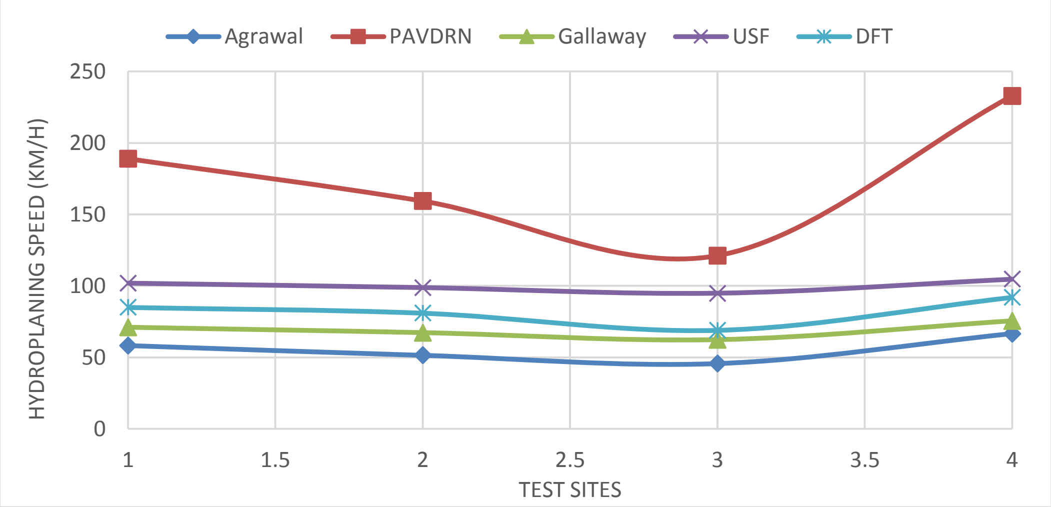

Figure 3.16 Comparison of predicted and measured hydroplaning speeds

3.3 Summary

This chapter mainly presents the validation of WFD estimation models and hydroplaning speed prediction models. For the validation of WFD estimation models, four models namely empirical PAVDRN, Gallaway model, NZ modified model, and analytical PAVDRN are involved and their sensitivity to mean texture depth, cross slope, longitudinal grade, and rainfall intensity are investigated respectively. The rain gauge and eTape liquid level sensor are used to measure the actual WFD. The LS-40 Surface Texture Analyzer and SurPro3500 Walking Profiler are used to measure pavement geometry feature and surface texture property on test sites, respectively. Finally six test sites are applied to investigate the reliability of the four WFD estimation models. Findings indicate the predicted WFDs from Gallaway model produces the best agreement with the ground truth, and thereby it would be served as the basis for the following hydroplaning speed prediction.

To examine the reliability of the hydroplaning speed prediction models, four models namely Agrawal model, Gallaway model, PAVDRN model, and USF model are tested. In this study the DFT is used to collect the potential hydroplaning speed on test areas with the built-up pool. Four AC pavement sites are chosen to validate which model would produce the better agreement with the ground truth. Results show the Gallaway and USF model are more accurate in hydroplaning speed prediction than other models. Accordingly the Gallaway and USF model are chosen for the following hydroplaning speed prediction in this study.

CHAPTER 4. DATA ACQUISTION AND PREPARATION

4.1 Data Acquisition System

As stated in Chapter 2, the factors that influence hydroplaning speeds include rainfall intensity, tire inflation pressure, tire tread depth, pavement width, pavement texture, cross slope, and longitudinal grade. In order to predict the potential hydroplaning speeds for network level pavement survey, pavement texture data, cross slope, and longitudinal grade should be continuously measured. In this study Inertial Measurement Unit (IMU) and PaveVision3D Ultra technology are mounted on DHDV to acquire pavement geometry and texture data respectively.

4.1.1 Digital Highway Data Vehicle (DHDV)

DHDV, developed by the WayLink Systems Corporation with collaborations from the University of Arkansas and the Oklahoma State University, has been evolved into the sophisticated system to conduct full lane data collection on roadways at highway speed up to 60 mph (about 100 km/h). Figure 4.1a shows the exterior appearance of the DHDV equipped with the 3D Ultra technology. With the high power line laser projection system and custom optic filters, DHDV can work at highway speed during daytime and nighttime and maintain image quality and consistency. The camera and laser working principle is shown in Figure 4.1b.

(a)

(b)

Figure 4.1 Photographs of (a) DHDV exterior appearance; (b) Pavevision3D working principle.

4.1.2 Inertial Measurement Unit (IMU)

Inertial Measurement Unit (IMU) is a self-contained sensor consisting of accelerometers and fiber-optic gyroscopes (XSENS 2015). The physical principle of gyroscope operation is analogous to the Doppler Effect, which involves determination of the phase shift between two counter propagating light beams.

Currently the IMU system have been integrated and synchronized into the DHDV vehicle. The accelerometer and fiber-optic gyroscopes within the IMU are mounted such that their sensor coordinate axes are not aligned with those of the vehicle. Figure 4.2 illustrates the orientation with which the IMU is mounted in the electronics module. Cross slope and longitudinal grade data are collected by IMU in this study.

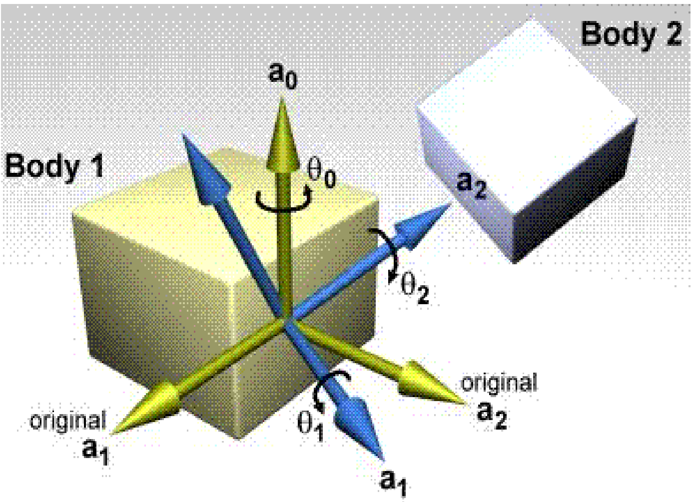

Figure 4.2 Transformed IMU coordinate axes

4.1.3 PaveVision3D Ultra Technology

With the latest PaveVision3D Ultra (3D Ultra in short), the resolution of surface texture data in vertical direction is about 0.3 mm and in the longitudinal direction is approximately 1 mm at 60 mph data collection speed. 3D Ultra is able to acquire both 2D and 3D laser imaging data from pavement surface through two separate left and right sensors. Each sensor in the rear of the vehicle consists of two lasers and five special-function cameras. For the two lasers, one is for providing 2D visual illumination and the other one is for providing the 3D data illumination. For the five cameras, four cameras are for capturing 3D laser illumination and the other one is for capturing 2D laser illumination (Wang 2011).

Figure 4.3 show the sensor system configuration of PaveVision3D in a DHDV. Each sensor case covers half of a lane and contains two sensor assemblies: 2D laser imaging for 1mm visual images, and 3D laser imaging for 1mm surface information. The PaveVision3D hybrid system can display surface texture in a visual and realistic format, which is used to obtain mean texture depth and transvers profile in this study.

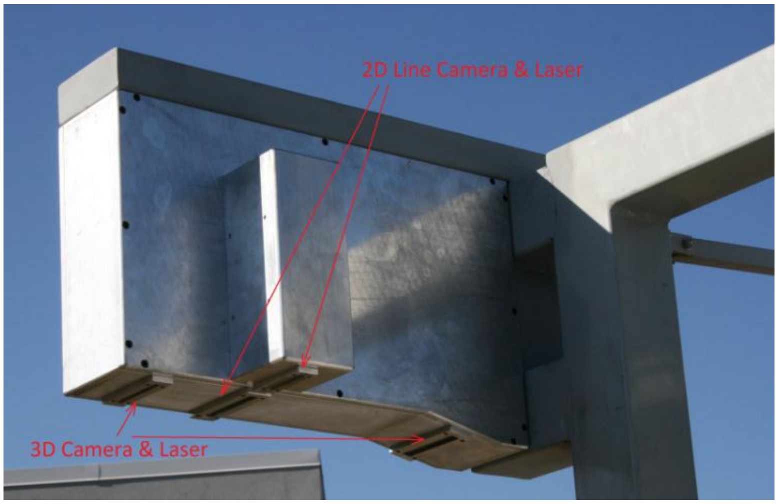

Figure 4.3 A laser imaging sensor (Wang, 2011)

4.2 Data Preparation

The collected raw data includes IMU roll angle, IMU pitch angle, IMU heading angle, vehicle speed, transverse acceleration, 3D laser imaging data, and Distance Measurement Instrument (DMI) pulse. The 3D imaging data collected is stored on computer hard disk in the form of raw images. Each raw image has a size of 4096 pixel wide by 2048 pixel long. The raw images are served as the basic sampling elements for mean texture depth calculation. The IMU data set has different sample size with 3D imaging data, but the two data sets can be matched by DMI pulse. The data source, sample size, and their applications are described in Table 4.1, and thus the data preparation covers the calculation of Estimated MTD, calibration of cross slope, horizontal curve radius measurement, and rutting measurement.

Table 4.1 Application of the Raw DHDV for Pavement Characteristics Measurement

Application	Raw Data	Source	Sample size
EMTD	3D Laser Imaging Data	PaveVision3D Ultra Technology	7.5ft
Cross Slope	IMU Roll Angle	IMU	0.625ft
	Transverse Profiling Data	PaveVision3D Ultra Technology	7.5ft
Longitudinal Grade	IMU Pitch Angle	IMU	0.625ft
Horizontal Curve	IMU Heading Angle	IMU	0.625ft
	IMU Roll Angle	IMU	0.625ft
	Transverse Acceleration	IMU	0.625ft
	Transverse Profiling Data	PaveVision3D Ultra Technology	7.5ft
	Distance Measurement Instrument (DMI) pulse	DMI	0.625ft
Pavement Rutting	Transverse Profiling Data	PaveVision3D Ultra Technology	7.5ft

4.2.1 Repeatability Test of the Collected Data

To verify the reliability of the calculated EMTD, cross slope, and longitudinal grade, the repeatability test is conducted. In this study The Analysis of Variance (ANOVA) method is used for data analysis.

4.2.1.1 Test Design

Two 1500ft road sections (sites #1 and #2) that are located at E Lakeview Road and W 32nd Street in Stillwater, Oklahoma are chosen as test bed. Three repetitive measurements are conducted on each test site. The test sites #1 and #2 are respectively constructed with grooved texture and the dragged texture. In this study the 3D texture and IMU data are sampled with a length of 7.5 feet, and thus there are 200 samples for each measurement pass. For each pass, the EMTD, calibrated cross slope, and longitudinal grade are calculated, as shown in Table 4.2.

Table 4.2 Example of EMTD and IMU Data of Test Site 1

Mileage (ft)	Pass 1			Pass 2			Pass 3		
	EMTD	Cross Slope	Long Grade	EMTD	Cross Slope	Long Grade	EMTD	Cross Slope	Long Grade
75	1.943	1.382	-1.3	1.897	1.448	-1.21	1.871	1.464	-1.22
150	1.987	1.479	-1.5	1.975	1.477	-1.43	1.963	1.505	-1.43
225	1.861	1.364	-1.49	1.918	1.38	-1.44	1.861	1.434	-1.42
300	1.753	1.368	-1.49	2.072	1.341	-1.44	1.691	1.398	-1.43
375	1.935	1.372	-1.47	1.987	1.336	-1.43	1.89	1.405	-1.42
450	1.867	1.366	-1.21	1.894	1.339	-1.18	1.758	1.375	-1.2
525	1.692	1.248	-0.65	1.721	1.233	-0.63	1.618	1.291	-0.64
600	1.798	1.262	9.933	1.953	1.233	9.856	1.848	1.285	9.72
675	1.556	1.241	0.18	1.951	1.247	0.214	1.828	1.24	0.197
750	1.583	1.263	0.28	1.969	1.272	0.306	1.872	1.274	0.271
825	1.519	1.153	0.414	1.938	1.176	0.42	1.771	1.196	0.409
900	1.411	1.191	0.791	1.788	1.218	0.792	1.616	1.171	0.789
975	1.591	1.189	1.288	1.802	1.224	1.282	1.813	1.233	1.286
1050	1.482	1.362	1.398	1.539	1.406	1.401	1.743	1.395	1.405
1125	1.379	1.18	1.415	1.495	1.238	1.418	1.769	1.224	1.419
1200	1.408	1.052	1.291	1.49	1.083	1.283	1.797	1.103	1.313
1275	1.496	1.034	1.433	1.576	1.082	1.465	1.841	1.096	1.444
1350	1.479	1.073	1.331	1.701	1.123	1.355	1.9	1.145	1.357
1425	1.541	1.028	0.86	1.988	1.062	0.865	1.901	1.079	0.853
1500	1.565	1.073	0.2	2.012	1.094	0.212	1.84	1.087	0.205

4.2.1.2 ANOVA Analyses

Analysis of Variance (ANOVA) is a common statistical technique for hypothesis test to check the equality of variations among two or more groups (Park 2009). In this study this technique is applied to test the repeatability of EMTD and IMU data of different runs or passes at the each test site. There are five distinct of levels (α) in scale for P-values: 0-0.001, 0.001-0.01, 0.01-0.05, 0.05-0.1, and 0.1-1. α = 0.05, the mostly widely used distinct level, is selected as distinct level, and the significant difference is considered as “existence” if the distinct of level is smaller than 0.05.

Based on the ANOVA test results at test site #1, significant difference exists among the three EMTD data sets ($\alpha = 0.05, F_{2,600} = 5.23, P = 0.0056$), while the IMU data sets appear in good repeatability ($\alpha = 0.05,$ Cross_slope: $F_{2,600} = 2.79, P = 0.0623,$ Longitudinal_grade: $t\_value = 0.57, P = 0.5703$). The EMTD distributions under different runs for test site #1 are plotted in Figure 4.4a. Note that EMTD from the first run is distinctively different from others. After removing EMTD data from the first run, ANOVA test shows there is good repeatability between data set #2 and #3 ($\alpha = 0.05, F_{1,400} = 0.69, P = 0.4057$).

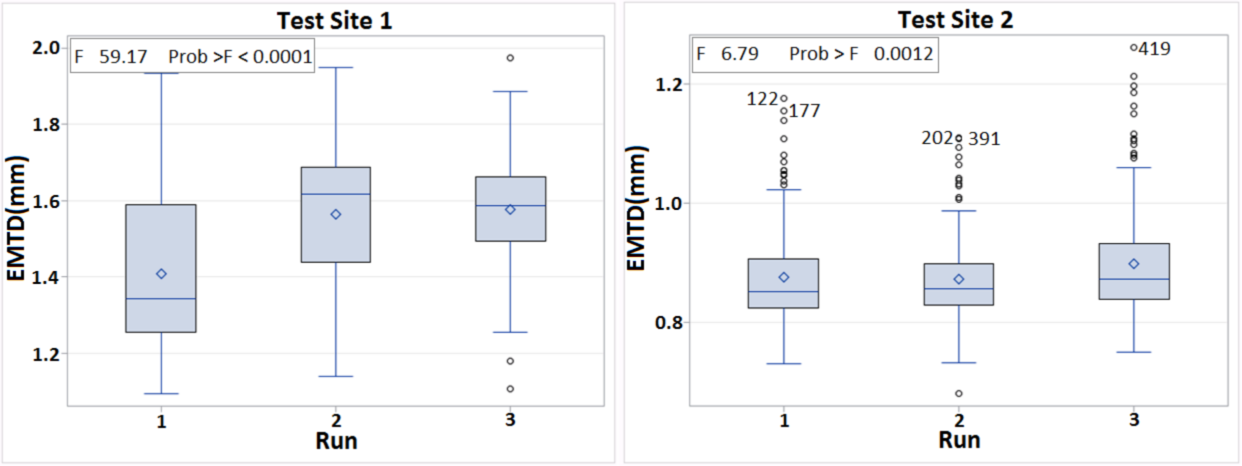

(a) (b)

Figure 4.4 Statistics analysis of EMTD data at (a) test site 1; (b) test site 2

Similar analysis is performed at test site #2. It is found that significant difference exists among the three EMTD data sets ($\alpha = 0.05, F_{2,600} = 7.34, P = 0.0007$), while the difference among the three IMU data sets are not significant ($\alpha = 0.05,$ Cross_slope: $F_{2,600} = 0.50,\ P = 0.60$, Longitudinal_grade: $t\_value = 0.34, P = 0.7357$). The EMTD under different runs for test site 2 are plotted in Figure 4.4b. It is determined that the EMTD data set from the third run should be removed. Again, ANOVA test for the data set #1 and #2 indicates that these two data set have good repeatability ($\alpha = 0.05, F_{1,400} = 0.06, P = 0.8075$).

4.2.1.3 Influences of Test Speed on Repeatability

ANOVA test result indicated the 3D texture data is not as good as IMU data in terms of the repeatability, which might be caused by two factors: (1) data collection are conducted under different test speed; (2) influences of the vehicle vibration on data quality are not suppressed. In this study influences of the traveling speed and body roll angle of survey vehicle on data quality are investigated to attempt to find the reasons that cause the unexpected errors in EMTD data. Finally a recommendation would be made to suppress factors affecting data quality, and thereby the high quality 3D texture data can be collected.

Figure4.5a shows the data collection speed distribution along the IMU data sample at test site #1. The test speed from run #1 is named as speed1, the similar name conversion is also used for the other two runs. Note that the speed of the three runs range from 20mph to 30 mph, and the standard deviation of data collection speed of 3 runs at test site 1 are 1.37, 2.47, and 2.60 respectively. The variation of the speed is not large to cause unexpected errors in EMTD data.

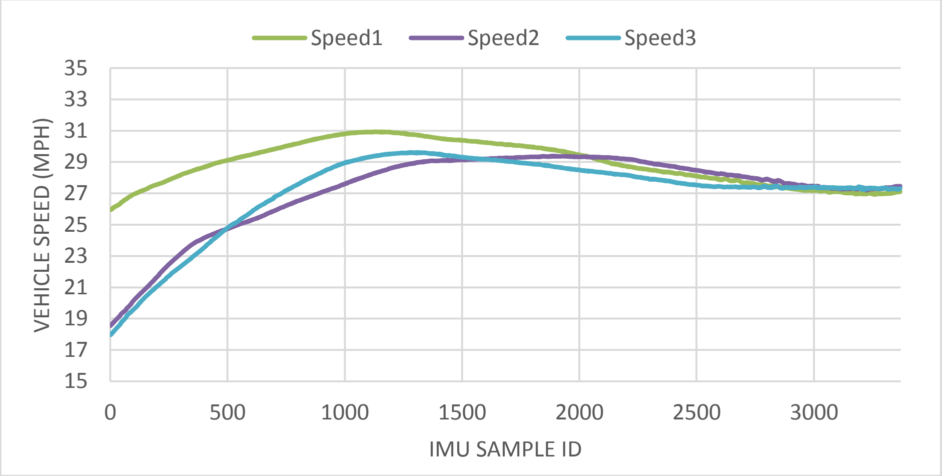

(a)

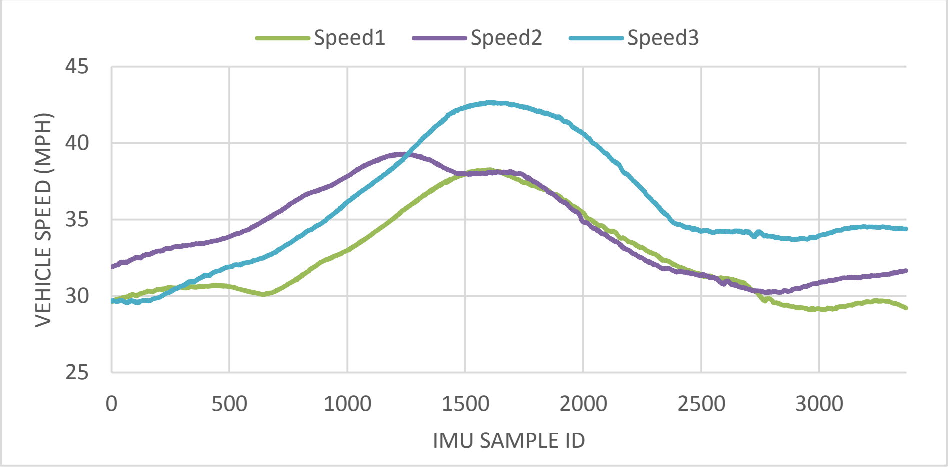

(b)

Figure 4.5 Data collection speeds of three runs at (a) test site 1; (b) test site 2

Figure 4.5b shows the data collection speeds along the IMU data sample at test site #2. The standard deviation of test speed at three runs are 2.94, 2.97, and 3.90, respectively. In addition, the range of speed3 is larger (from 30mph to 43mph) than the speed1 and spee2. It can be estimated that the EMTD from run#3 may be not have the good repeatability with the EMTDs from the other two runs, which has a good agreement with the ANOVA test result.

4.2.1.4 Influences of Vehicle Vibration on Data Repeatability

Figure 4.6a shows the body roll of survey vehicles under three runs at test site #1. The body roll are calculated from 3D transvers profiling data (200 samples for each run). The average values from the three runs are 1.87, 0.26, and 0.29, respectively. Note that the vehicle body roll angle from the run #1 is around seven times larger than the values from run #2 and #3. The large difference between run#1 and the other two runs might be caused by vehicle vibration during data collection, which agree with the results from ANOVA test.

Figure 4.6b shows the body roll of survey vehicles under three runs at test site #2. The average values of the vehicle body roll from the three runs are 0.35, 0.37, and 0.34, respectively. Note that the variations of vehicle body roll angle are pretty small for the three passes, and their impacts on data quality can be overlooked in this case. However, due to the impacts of test speed, the EMTD from run#3 still have the poor repeatability with that from the other two runs.

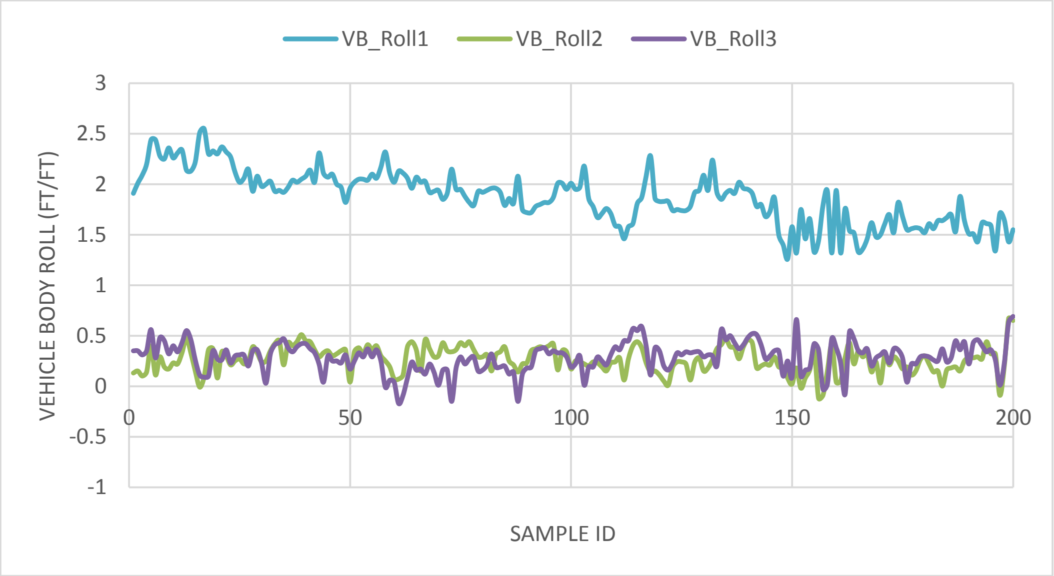

(a)

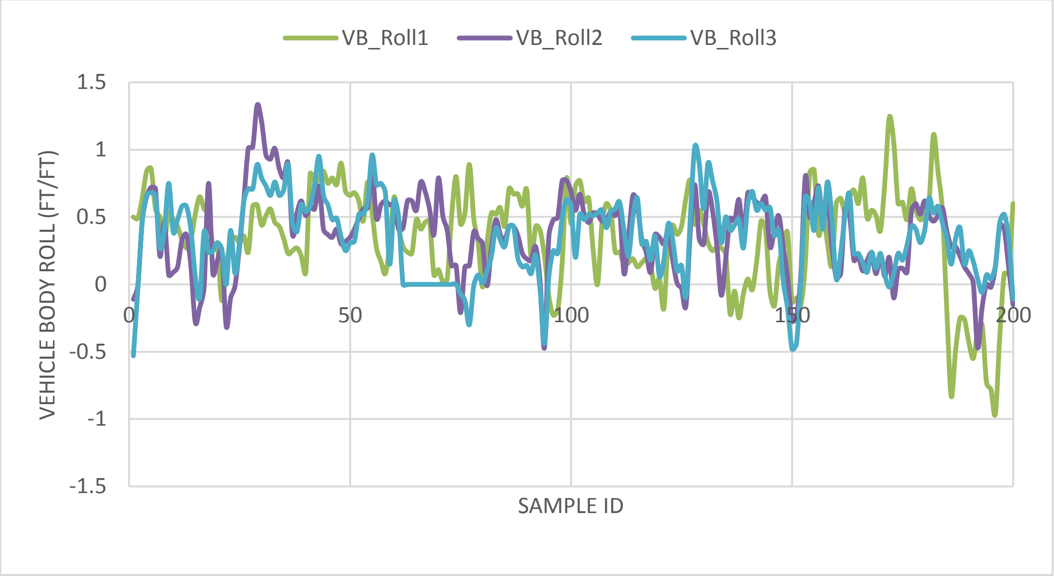

(b)

Figure 4.6 Survey vehicle body roll under three runs at (a) test site #1; (b) test site #2

Based on the abovementioned analysis, it is recommended that the data collection should be conducted at constant speeds and avoid vehicle vibration, through which the impacts of test speeds and the vehicle vibration on data quality can maximally suppressed.

4.2.2 Estimated Mean Texture Depth (EMTD)

In this study the 1mm 3D texture data is used to calculate mean texture depth by simulating sand patch method, and the calculated index is termed as Estimated Mean Texture Depth (EMTD). As a volumetric method, the calculation of EMTD is based on 1mm 3D laser imaging data of the entire lane, as shown in Equation 4.1 (Wang 2011). EMTD and MTD are assumed to be equivalent in this research.

$$\mathrm{EMTD} = \frac{1}{\mathrm{K}} \times \sum_{\mathrm{i}=1}^{\mathrm{K}} \frac{\iint_0^{\mathrm{D}} [\mathrm{F_0} - \mathrm{F}(\mathrm{x},\mathrm{y})]\mathrm{dxdy}}{\mathrm{D}} = \frac{1}{\mathrm{K}} \times \sum_{\mathrm{i}=1}^{\mathrm{K}} \frac{\sum_{\mathrm{x}=1}^{\mathrm{x}=\mathrm{N}} \sum_{\mathrm{y}=1}^{\mathrm{y}=\mathrm{M}} [\mathrm{F_0} - \mathrm{F}(\mathrm{x},\mathrm{y})]}{\mathrm{D}} \quad (4.1)$$

Where, $F(x, y)$ The pixel depth at point (x, y); D: The integral or gridded area containing of M×N pixels; F_0: The maximum peak in each area D; K: The number of grids within the test sample.

4.2.3 Cross Slope Calibration

A properly designed and constructed cross slope is important since it allows water to drain off the pavement surface as rapidly as possible, and thereby reduce hydroplaning and traffic accidents. Too small slope may cause low efficiency of drainage, while too large slope may cause vehicle handling problems. IMU mounted on the data vehicle can measure the Euler angles, which are termed as roll (Euler angle about x-axis), pitch (Euler angle about y-axis) and yaw (Euler angle about z-axis) (Bancroft 2011).

Typically the roll angle is widely accepted to represent pavement cross slope, and pitch angle is widely used to represent the pavement longitudinal grade. Their measurements were conducted on the assumption that the vehicle floor is parallel with the pavement surface during the travelling. However, in real word the vehicle floor is unparalleled with the pavement surface during data collection (Figure 4.7) with the following reasons: 1) the uneven gravity distribution of vehicle; 2) the vibration of the vehicle during the traveling; 3) surface condition of pavement.

This paper attempts to measure the survey vehicle body roll angle (angle γ) using the transverse profiling data collected by PaveVision 3D Ultra technology. The instruments used in measuring the cross slope include IMU system and the 3D Ultra sensors. The IMU is mounted in the middle of DHDV, and the four 3D laser cameras are overhung on the rear end of DHDV (two for each side). These four 3D laser cameras cover the entire lane, and the transverse profiling data from the 3D sensors are directly related to the distance between the pavement surface and the 3D sensors. The "true" cross slope of the road way can be approximately determined based on two values: the tilt of the vehicle floor and the slope of the road surface visualized by the lasers.

Due to roughness and distress of pavement, the road surface does not appear as straight line in transverse direction. Therefore, a method, the Least Squares Approximation (LSA) of the laser sensor readings, is used to solve this problem. The LSA lines fit could be given by Equation 4.2.

$$y = ax + b \tag{4.2}$$

As Figure 4.7 shows, the IMU provides angle of the vehicle relative to a level datum, as shown by angle θ, and the difference in laser measured height y_1 and y_2 over distance L is equal to the slope of the vehicle relative to the pavement (Equation 4.3). Therefore, the cross slope can be obtained by the Equation 4.4.

$$\gamma = \mathrm{act}\tan(\frac{y_2 - y_1}{L}) \tag{4.3}$$

$$\alpha = \tan(\theta - \gamma) \tag{4.4}$$

Since the angle θ and γ are very small, the cross slope equals to the slope of IMU roll angle minus the slope of vehicle relative to the pavement, as Equation 4.5 shows (Mekemson 2002).

$$\alpha = \tan(\theta) - \tan(\gamma) \tag{4.5}$$

Where α: Cross slope of pavement, m/m; γ: Angle measured by the laser sensors with respect to the roadway surface, degree; θ: Roll angle measured by the IMU, degree; L: The distance between left and right laser, m; y_1: The vertical distance from left sensor to the least-square approximation line of pavement, m; y_2: The vertical distance from right sensor to the least-square approximation line of pavement, m.

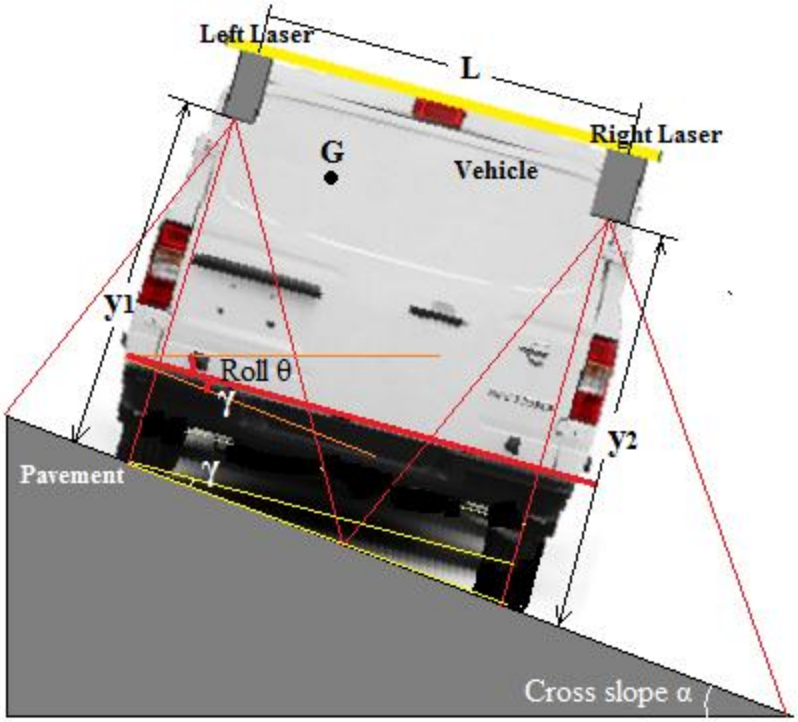

Figure 4.7 Estimation of cross slope from IMU roll angle and laser measurement

4.2.4 Horizontal Curve Measurement

Typically the special design is used at horizontal curve segments of roadways, and the resulting hydroplaning risk would be different with that on straight road section. The cross slope at the horizontal curves is known as super-elevation. The lead-in and lead-out play a major role in gradually adjusting the super-elevation from the regular cross slope on a straight roadway to the maximum super-elevation at the curve. The design values of super-elevation depend on the radius of horizontal curve, as Table 2.5 shows. Therefore, measuring the horizontal curve radius is necessary for hydroplaning risk evaluation. Three methods namely Kinematics method, Geometry method, and Lateral acceleration method are employed to compute horizontal curve radius based on both IMU and 3D transverse profiling data. To examine effectiveness of the three methods in radius calculation, the ground truth measured by satellite pictures is used.

4.2.4.1 Kinematics Method

The kinematic method uses the velocity in the longitudinal direction and the centrifugal acceleration of survey vehicle for curve radius calculation (Beer 1977), as Equation 4.6 shows. Both "v" and "a" are directly obtained by IMU: "v" is the north velocity in IMU data set, and "a" is the transverse acceleration in IMU data set.

$$R = \frac{v^2}{a} \tag{4.6}$$

Where, R: curve radius, m; v: the velocity of the vehicle in the longitudinal (body X) direction measured by IMU, km/h; a: the centrifugal acceleration of the vehicle on a horizontal plane measured by IMU, m/s^2.

4.2.4.2 Geometry Method

The geometry method plots the actual vehicular horizontal trajectory using the velocity vector and then determines the radius (Duminda 2007), as Figure 4.8 shows. Due to the presence of high resolution data, the error associated with the linear approximation can be ignored for the vehicular horizontal trajectory.

The longitudinal displacement of the vehicle between two consecutive data points i and ($i+1$) can be calculated by Equation 4.7 using the average velocities at those two points. In this method, the vehicle trajectory on the x-y plane is described by the function $y = f(x)$, and the curve radius can be calculated by Equation 4.8. Since x and y coordinates are found in terms of time as discrete quantities (Equation 4.9 and 4.10), the second order Forward Difference formulae can be obtained by Equation 4.11-4.14, and the numerical forms of the derivatives can be obtained by Equation 4.15 and 4.16.

$$ds = \frac{1}{2}(v_i + v_{i+1})dt \tag{4.7}$$

$$R = \frac{(1 + (\frac{dy_i}{dx_i})^2)^{3/2}}{(\frac{d^2y_i}{dx_i{}^2})} \tag{4.8}$$

$$x_i = \mathrm{x}_{(\mathrm{i}-1)} + 1.0161 \times (\mathrm{D}_\mathrm{i} - \mathrm{D}_{(\mathrm{i}-1)}) \times cos(\alpha_\mathrm{h} \times \frac{3.14}{180}) \tag{4.9}$$

$$y = \mathrm{y}_{(\mathrm{i}-1)} + 1.0161 \times (\mathrm{D}_\mathrm{i} - \mathrm{D}_{(\mathrm{i}-1)}) \times sin(\alpha_\mathrm{h} \times \frac{3.14}{180}) \tag{4.10}$$

$$x' = \frac{(-x_{(i+2)} + 4x_{(i+1)} - 3x_i)}{2h} \tag{4.11}$$

$$y' = \frac{(-y_{(i+2)} + 4y_{(i+1)} - 3y_i)}{2h} \tag{4.12}$$

$$\mathrm{x}'' = \frac{(-\mathrm{x}_{(\mathrm{i}+3)} + 4\mathrm{x}_{(\mathrm{i}+2)} - 5\mathrm{x}_{(\mathrm{i}+1)} + 2\mathrm{x}_\mathrm{i})}{\mathrm{h}^2} \tag{4.13}$$

$$\mathrm{y}'' = \frac{(-\mathrm{y}_{(\mathrm{i}+3)} + 4\mathrm{y}_{(\mathrm{i}+2)} - 5\mathrm{y}_{(\mathrm{i}+1)} + 2\mathrm{y}_\mathrm{i})}{\mathrm{h}^2} \tag{4.14}$$

$$\frac{\mathrm{dy}_\mathrm{i}}{\mathrm{dx}_\mathrm{i}} = \frac{\mathrm{y}'}{\mathrm{x}'} \tag{4.15}$$

$$\frac{\mathrm{d}^2\mathrm{y}_\mathrm{i}}{\mathrm{dx}_\mathrm{i}^2} = \frac{(\mathrm{y}''\mathrm{x}' - \mathrm{x}''\mathrm{y}')}{(\mathrm{x}')^2} \tag{4.16}$$

Where, R: curve radius, m;ds: the longitudinal displacement that occurs when the vehicle travels between the points i and (i+1); v_i: the respective velocities at points i, km/h; dt: the time elapsed during the travel between points i and (i+1); D_i: Distance Measurement Instrument (DMI) pulse at point i from IMU; α_h: IMU heading angle, degree.

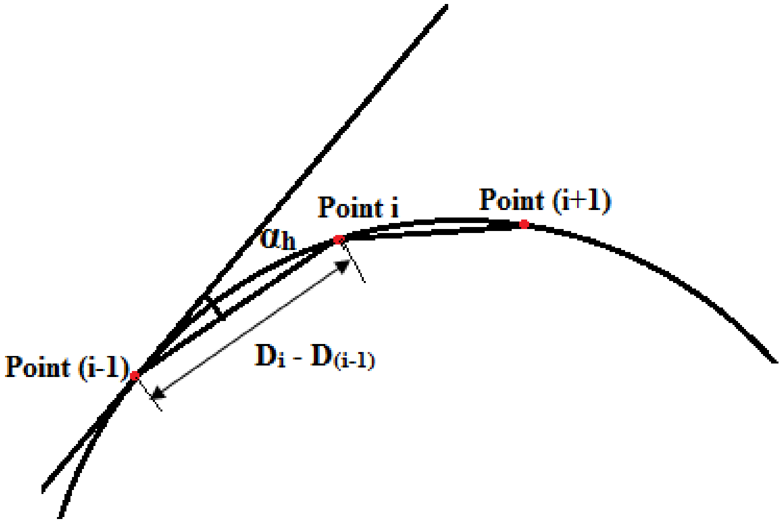

Figure 4.8 Geometry method for curve radius measurement

4.2.4.3 *Lateral Acceleration Method*

The lateral acceleration method uses the same equation as BBI method (Equation 4.17: point-mass equation) for curve radius calculation (Carlson 2008). Different from BBI method, the lateral acceleration, vehicle speed, and the super-elevation are measured by IMU and PaveVision 3D Ultra technology. In IMU data set, the lateral acceleration, "a", is the transverse acceleration, and the "v" is the vehicle speed.

$$R = \frac{v^2}{127(e + a)} \tag{4.17}$$

Where, R: curve radius, m; v: vehicle speed, km/h; e: super-elevation, m/m; a: lateral acceleration measured by IMU, m/s^2.

4.2.4.4 *Chord Offset Method in Field*

The chord offset method is a common method for roadway curve radius calculation (Carlson 2008). In this study the chord length and offset distance of road curve are measured on satellite pictures. Firstly, an electric tape is used held on either end at the precise edge of the road way in the satellite picture, and then an electric comparing rule is used at the middle of the tape to measure the distance between the edge of the tape and the edge of the roadway. The curve radius can be calculated by Equation 4.18. The curve radius measured by this method is considered as ground truth in this study.

$$R = \frac{L^2}{8\mathrm{M}} + \frac{\mathrm{M}}{2} \tag{4.18}$$

Where, R: curve radius, m; L: the chord length, m; M: Offset distance, m.

4.2.5 Pavement Rutting Measurement

In this study the transverse profile data extracted from 3D texture data is applied for rutting measurement in compliance with the standard procedures specified in AASHTO PP69 (AASHTO, 2010). The rutting depth and width are important factors for rutting water film depth calculation.

To measure rutting dimension (e.g. depth and width), a dedicated software is developed. Figure 4.9 shows the measured rutting dimension and their calculation process based on one transverse profile. The calculated rut depth and width are displayed in the left side of the interface. The first curve at the top left side shows the raw transverse profile extracted from 1mm 3D texture data. The second chart at the top right side shows the filtered transverse profile in compliance with AASHTO PP-69. The third chart at the bottom left side show the calibrated transverse profile by combining with IMU roll data. The fourth curve at the bottom right side shows the rotated transverse profile in horizontal level. Finally, the rutting depth and width are measured in accordance with the AASHTO PP-69 calculation standards.

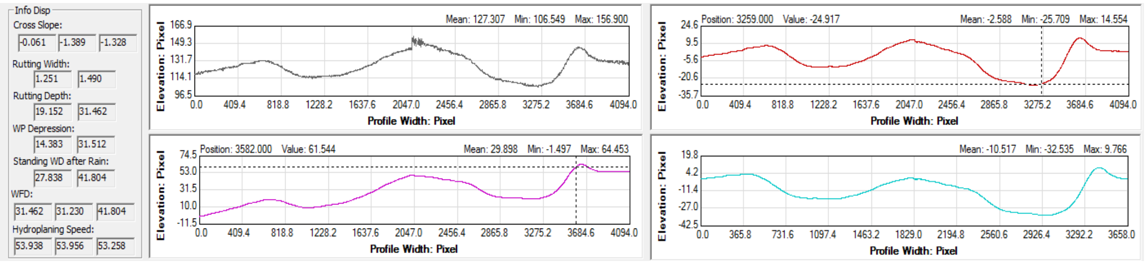

Info Disp
Cross Slope: -0.061 -1.389 -1.328
Rutting Width: 1.251 1.490
Rutting Depth: 19.152 31.462
WP Depression: 14.383 31.512
Standing WD after Rain: 27.838 41.804
WFD: 31.462 31.230 41.804
Hydroplaning Speed: 53.938 53.956 53.258

Figure 4.9 Rutting depth and width measurement

4.3 Summary

This chapter presents two subsystems mounted on Digital Highway Data Vehicle (DHDV), namely IMU and PaveVision3D Ultra. PaveVision3D Ultra is used to acquire 1mm 3D texture data and IMU system is used to collect the longitudinal grade and cross slope data. The repeatability test of the collected data are conducted on two test sites. The repeatability of IMU data are analyzed using ANOVA statistical method, and findings indicate the good repeatability exist among the three repetitive passes. The repeatability of 3D texture data is represented with EMTD, and findings indicate a fair agreement exist among three repetitive passes. Results also indicate the quality of 3D texture data is susceptible to test speeds and vehicle vibration. Therefore, during data collection the constant test speeds and avoiding vibration are recommended to guarantee data quality.

EMTD is used to describe pavement texture properties and calculated by simulating sand path method with 3D image texture data. To obtain the accurate cross slope data, the roll data from IMU systems are calibrated with the transverse profile data, and thereby the actual cross slope can be measured. The horizontal curve radius measurement plays an important role in predicting hydroplaning speed at horizontal curve segments. Three IMU data based approaches namely kinematic method, Geometry method, and Lateral acceleration method are presented to determine the radius of horizontal curves. The pavement rutting measurement is conducted based on AASHTO PP 69 standard.

The chapter are served as the basis for the hydroplaning speed prediction under various scenarios such as on the regular pavement surface, on the horizontal curve segments, and on the rutting pavements.

CHAPTER 5. HYDROPLANING SPEED PREDICTION ON REGULAR PAVEMENTS

5.1 Model Preparation

In this study the regular pavement surface are defined as pavement sections without the horizontal curve, the large longitudinal slope, and the pavement rutting, based on which the hydroplaning risk evaluation can be conducted. The model evaluation results in Chapter 3 indicate the predicted values from Gallaway model has the best agreements with the ground truth, and thus it would be chosen for hydroplaning risk evaluation in this study.

Prior to using hydroplaning speed prediction models, several key parameters should be determined first, including rainfall intensity, MTD, cross slope, and longitudinal grade. In this study the rainfall intensity is obtained from official government agencies. The MTD in the Gallaway model is substituted by EMTD derived from the volumetric measuring method using 3D texture data. The cross slope is substituted by the calibrated cross slope that are calculated from the IMU roll data and 3D texture data. The longitudinal grade is directly calculated from the IMU pitch data. Subsequently water film depth can be calculated using Equation 2.18, based on which the hydroplaning speed can be predicted using Equation 2.14. By comparing predicted hydroplaning speeds with the posted speed limit, pavement segments with the potential hydroplaning risk can be identified out so that pavement engineers can take a series of maintenance activities to avoid the occurrence of traffic accident due to hydroplaning.

5.2 Case Study

5.2.1 Test Sites

Two field test sites are located at E Lakeview Road and W 32nd Street in Stillwater, Oklahoma. Lakeview Road and the 32nd Street are constructed with grooved texture and the dragged texture respectively. The test section length, lane width, and surface condition are given in Table 5.1.

Table 5.1 Summary of Test Sites (Hydroplaning Evaluation for Straight Road Sections)

Site No	Location	Test Length	Lane Width	Texture Type	Surface Condition
1	Lakeview Rd	1500ft	12ft	Grooved, random spacing	Good
2	W 32nd Ave	1500ft	12ft	Broom dragged texture	Good

5.2.2 Local Rainfall Intensity

The local rainfall intensity at the test site is obtained from National Oceanic and Atmospheric Administration's (NOAA) National Water Service database (NOAA 2015). Table 5.2 shows the precipitation in Stillwater Station Oklahoma from NOAA database. The two-year return period storm with duration of five minus is used for rainfall intensity acquisition. In this section the local average and maximum rainfall intensity are chosen to predict WFD. Based on precipitation data from NOAA'S National Water Service (NOAA

2015), the average and maximum rainfall intensity in Stillwater OK are 6 in/h and 6.972 in/h, respectively.

Table 5.2 Precipitation (90% Confidence Intervals) in Stillwater Station (NOAA 2015)

Duration (in inches)	**Average recurrence interval (years)**			
	1	**2**	**5**	**10**
5 min	0.428 (0.376-0.498)	0.499 (0.437-0.581)	0.615 (0.537-0.717)	0.710 (0.616-0.832)
10 min	0.627 (0.550-0.729)	0.731 (0.640-0.850	0.900 (0.786-1.05)	1.04 (0.903-1.22)
15 min	0.765 (0.671-0.889)	0.891 (0.781-1.04)	1.10 (0.958-1.28)	1.27 (1.10-1.49)
30 min	1.14 (0.997-1.32)	1.33 (1.16-1.54)	1.64 (1.43-1.91)	1.89 (1.64-2.21)
60 min	1.51 (1.32-1.75)	1.76 (1.54-2.05)	2.17 (1.90-2.53)	2.51 (2.18-2.94)
2 hr	1.88 (1.66-2.17)	2.19 (1.93-2.54)	2.71 (2.38-3.13)	3.13 (2.73-3.64)
3 hr	2.09 (1.85-2.41)	2.44 (2.16-2.81)	3.01 (2.65-3.47)	3.49 (3.05-4.04)

5.2.3 MTDs and WFDs at the Two Sites

Figure 5.1 shows the EMTDs at two test sections. Since the pavement surface at test site 1 is constructed with transverse grooves, the EMTD at this site is approximately 1.5 mm, which is 0.6 greater than the EMTD at test site 2 which is constructed with dragged texture. Typically MTDs at grooved sections are greater than the MTDs at dragged sections with the exception that pavement has been worn out with very shallow grooves.

The MTD, longitudinal grade, cross slope, and rainfall intensity are incorporated into the Gallaway model to predict the WFD. In this section the local average and maximum rainfall intensity are chosen to predict WFD. Results indicate that the dragged texture pavement section has greater WFDs than that with grooved texture. In other words, pavement section with dragged texture has worse pavement surface drainage performance than grooved pavement section, as shown in Figure 5.2.

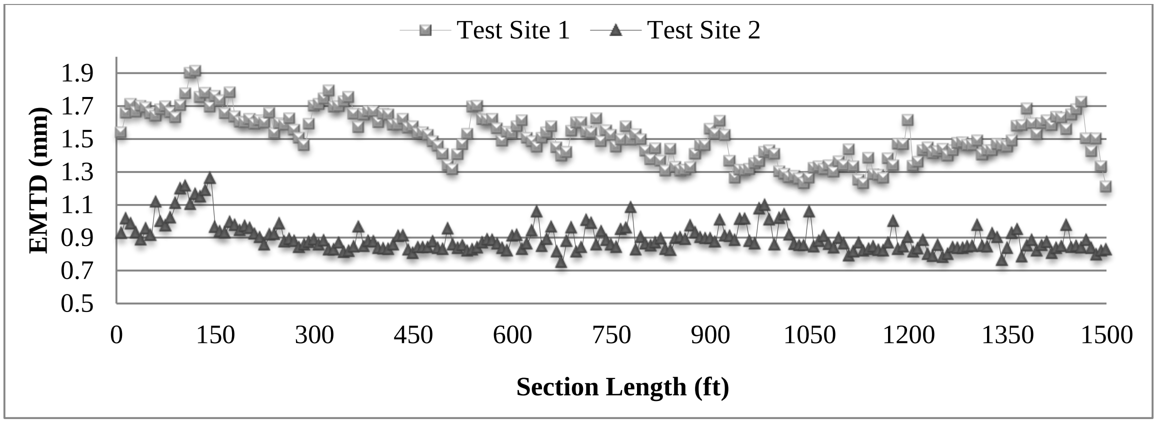

Figure 5.1 EMTDs at two sites

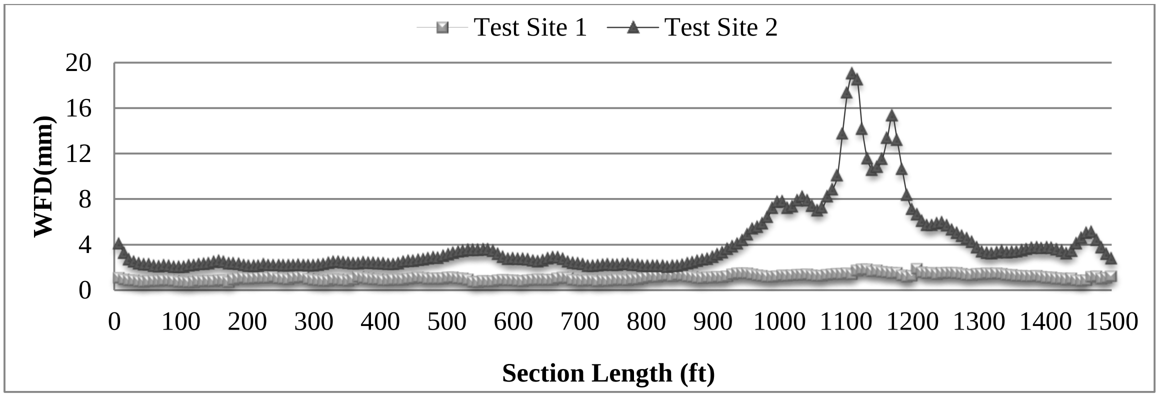

Figure 5.2 WFDs at two sites

5.2.4 Potential Hydroplaning Segment Detection

Predicting the pavement hydroplaning speed and identifying the segments that are susceptible to hydroplaning are very practical for pavement management. Figure 5.3 shows the predicted hydroplaning speeds based on Gallaway model at two test sections. At test section 1, the speed limit is 35 mph. The predicted hydroplaning speeds across the entire section are much greater than the speed limit, which entails there is no potential hydroplaning at this section if drivers abide by the speed limit, as illustrated in Figure 5.3a and Figure 5.4a. At test section 2, the speed limit is 45 mph. Hydroplaning might occur within the segment ranging from 1080ft to 1185ft, as shown in Figure 5.3b where the predicted hydroplaning speed is lower than 45 MPH. It should be noted that there is a high hydroplaning risk at the segments marked with the yellow circle in Figure 5.4b. Highway agency may post a reduced speed traffic sign at that location to minimize the traffic accident caused by hydroplaning. In addition, pavement engineers may also take other measures such as constructing superior grooving texture to increase the potential hydroplaning speed.

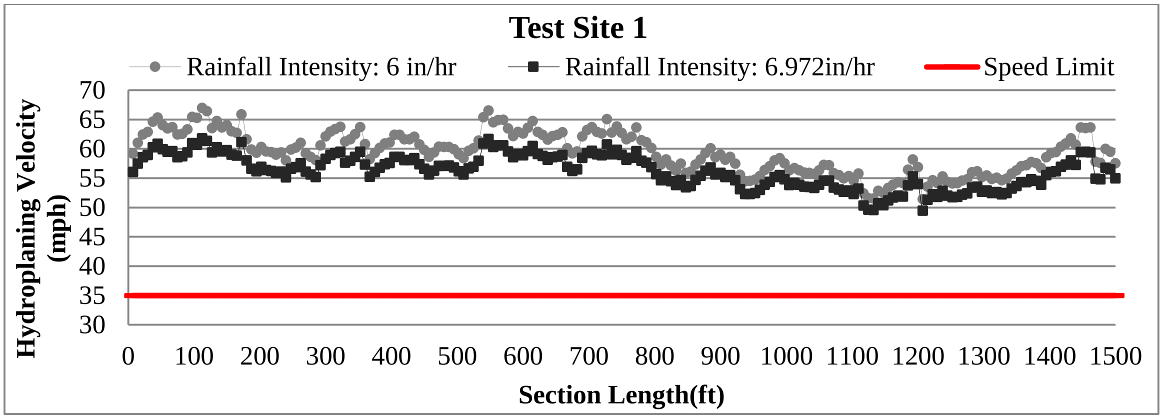

(a)

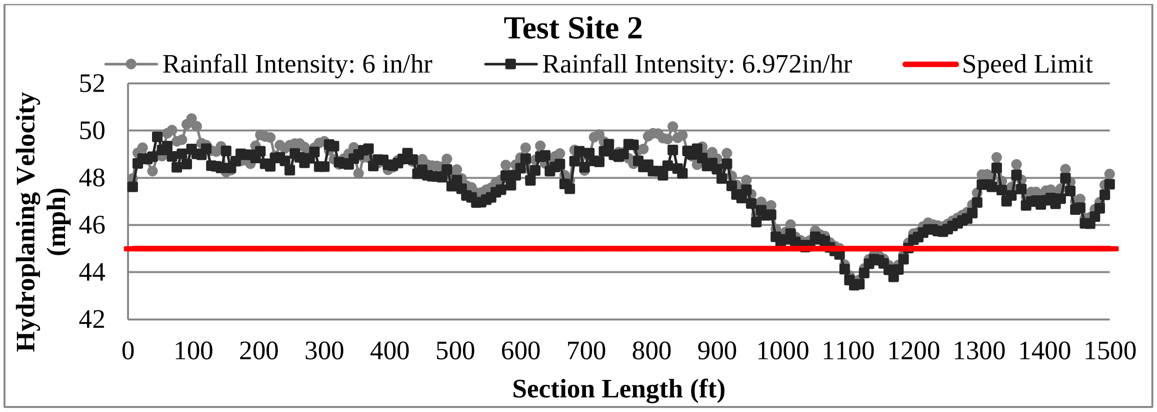

(b)

Figure 5.3 Predicted hydroplaning speed at: (a) test site 1; (b) test site 2

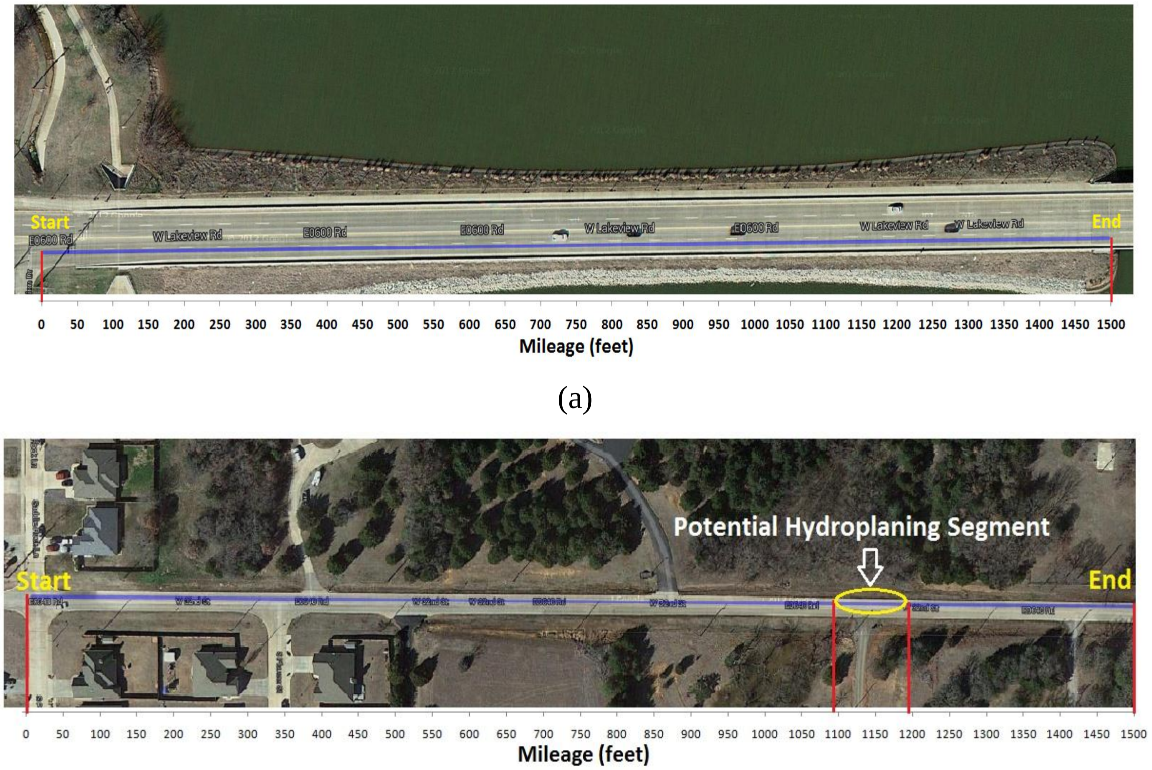

(a)

(b)

Figure 5.4 Potential hydroplaning segments at: (a) test Site 1; (b) test Site 2

5.3 Summary

This chapter presents the application of Gallaway model in hydroplaning speed prediction. The four key parameters used in Gallaway model namely MTD, cross slope, longitudinal grade, and rainfall intensity need to be determined first. In this study the 3D texture data and IMU data are continuously collected on the test section. The local rainfall intensity data are obtained from National Oceanic and Atmospheric Administration's (NOAA) National Water Service database.

Once the values of four parameters are determined, the following task is to estimate the WFD by incorporating them into the Gallaway model. Subsequently the hydroplaning speed can be predicated based on the Gallaway prediction model. In order to identify the pavement segments have the potential hydroplaning risk issues, the comparisons between the predicted hydroplaning speeds and the posted speed limit are made. Once the potential hydroplaning segments of the test sections are detected, pavement engineers can take a series of maintenance activities on hazardous segments, and further to avoid the occurrence of traffic accident due to hydroplaning.

CHAPTER 6. HYDROPLANING SPEED PREDICTION ON PAVEMENTS WITH LARGE SLOPES

6.1 Model Preparation

Pavement slope includes the cross slope and longitudinal grades. Its main objective is to ensure the rapid removal of rain, melting snow and ice from pavement surface. The increase of the cross slope of roadways would short drainage time and flow path length, and thereby reducing the risk of hydroplaning occurrence. Longitudinal grade or slope is also an important factor that is associated with surface drainage. It can shorten or extend the water runoff time on pavement surface depending on flow path length. Therefore, the presence of longitudinal grade may decrease or increase the risk of hydroplaning occurrence.

6.1.1 Effects of Pavement Slope on Wheel Load

In Chapter 5, effects of cross slope and longitudinal grade have been incorporated into the WFD and hydroplaning prediction models. However, the cross slope and longitudinal grade not only affect WFD, but also affect the vertical load on pavement surface.

Typically cross slope and longitudinal grade would reduce the vertical wheel load of vehicles on pavement surface. Hydroplaning occurs when the vertical wheel load is equivalent to the uplift force by water (Equation 6.1), and the steering and traction force would be lost during hydroplaning.

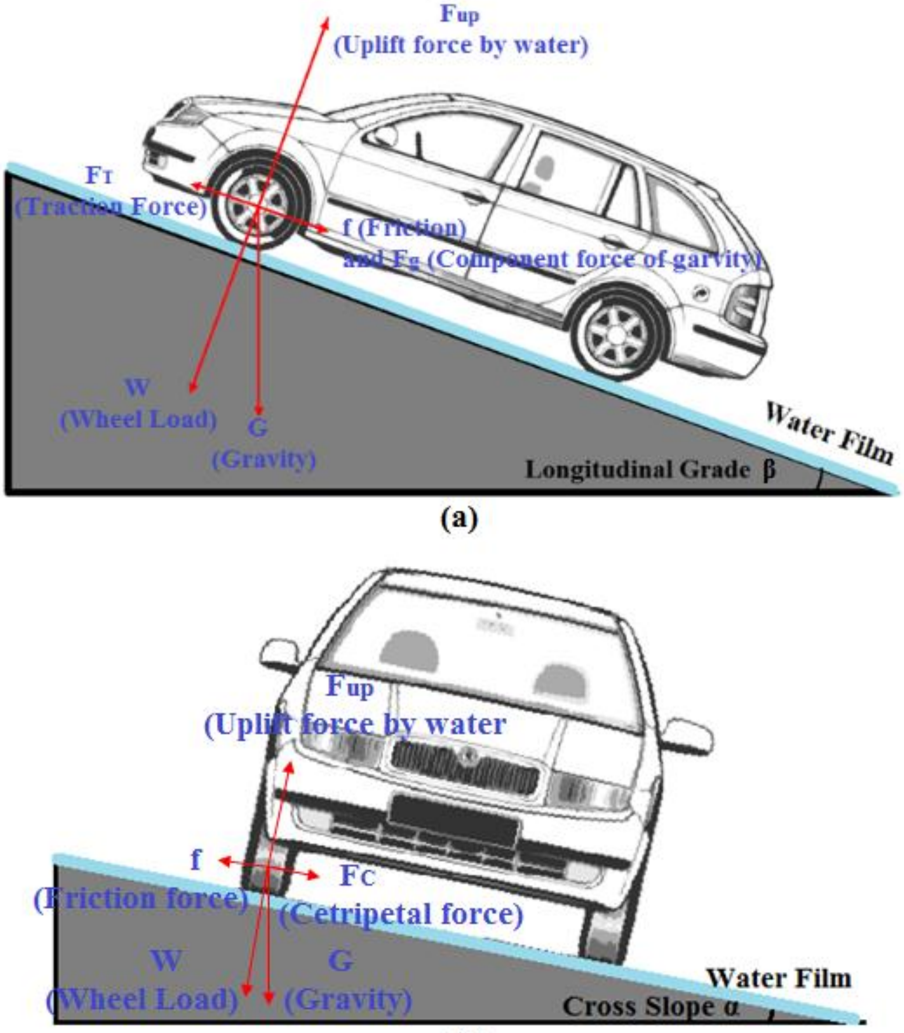

(a)

(b)

Figure 6.1 Vehicle travelling on (a) pavements segments with longitudinal grade; (b) pavement segment with horizontal curve

Figure 6.1a shows the pavement section with a large longitudinal grade. When the vehicle travels on this pavement segment, the vehicle gravity would be partitioned into two components of forces: one (wheel load) is perpendicular with the travelling surface, and the other one (traction force) is parallel with pavement surface. The wheel load would decrease with the increase of longitudinal grade (Equation 6.2), and the reduced wheel load would increase the hydroplaning risk.

Figure 6.1b shows the pavement section with horizontal curves or large cross slope. Similarly, the vehicle gravity is partitioned into two components of forces when the vehicle travels on the horizontal curve. One component of force is the wheel load, and the other one is the centripetal force shown in Figure 6.1b. The wheel load on horizontal curve would decrease with the increase of super-elevation (Equation 6.3). Finally the wheel load can be calculated with flow path slope by combining the cross slope and longitudinal grade, as given in Equation 6.4.

$$F_{Up} = W \tag{6.1}$$

$$W_L = G \times cos(\beta) \tag{6.2}$$

$$W_C = G \times cos(\alpha) \tag{6.3}$$

$$W = G \times cos(\rho) \tag{6.4}$$

Where, F_{Up} -- Minimum uplift force causing hydroplaning, N; W -- Wheel load, N; W_L -- Wheel load in longitudinal section, N; W_C -- Wheel load in cross section, N; G -- Gravity of vehicle, N; β -- Angle of longitudinal grade, degree; α-- Angle of cross slope, degree; ρ -- Angle of flow path slope, degree.

Note that the effects of pavement slope on vehicle traction force and wheel load cannot be ignored when the large pavement slope appears, and their effects on wheel load and traction forces should be reflected in WFD and hydroplaning speed prediction models as well. Accordingly in this study the original WFD and hydroplaning would be modified based on the mechanic theory.

6.1.2 Modified Gallaway and USF Models

Two hydroplaning prediction models, the Gallaway model (Equation 2.14-2.18) and USF model (Equation 2.24) are chosen for hydroplaning risk evaluation. The influences of flow path slope on vertical wheel load are neglected in the original hydroplaning speed prediction models since the development of these models are based on the flat and straight pavement sections. For pavements with larger slopes, the reliable models for hydroplaning speed prediction are still missing. To overcome this limitation, this study aims at modifying the existing Gallaway and USF models by taking account into the effects of flow path slope on vertical wheel loads, as shown in Equations 6.5 and 6.6 respectively. The WFD calculation in this section is based on Gallaway WFD model.

$$v_p = 0.9143 \times SD^{0.04} \times (P_t \times cos\rho)^{0.3} \times (TD + 0.794)^{0.06} \times A \tag{6.5}$$

$$v_p = (W \times cos\rho)^{0.2} \times (P_t \times cos\rho)^{0.5} \times (0.82/WFD^{0.06} + 0.49) \tag{6.6}$$

Where, W -- Wheel load, N; WFD -- Water film depth, mm; P_t -- Inflation pressure, Kpa; SD -- Spin down ratio; TD -- Tire tread depth, mm; A -- Maximum value of Equation 16 and 17; ρ -- Angle of flow path slope, degree.

6.1.3 Sensitivity Analysis of the Modified Models

To explore the sensitivity of modified models to cross slope and longitudinal grade, the cross slope and longitudinal grade change by ± 25%, ± 50%, and ± 75% individually while the other variables are maintained constant values, as provided as follows:

- Cross slope: $S_c = 1.53\%$
- Rainfall intensity: $I = 148.4\ mm/hr$
- Mean texture depth: $\mathrm{MTD} = 1.2\ \mathrm{mm}$
- Longitudinal grade: $\mathrm{S_l} = 1.32\%$

The results of sensitivity analysis from the modified Gallaway and USF models to cross slope and longitudinal grade are given in Figure 6.2. It can be seen that the resulting change in hydroplaning speed, "$\mathrm{V_p}$", is apparent along the increase of cross slope and longitudinal grade.

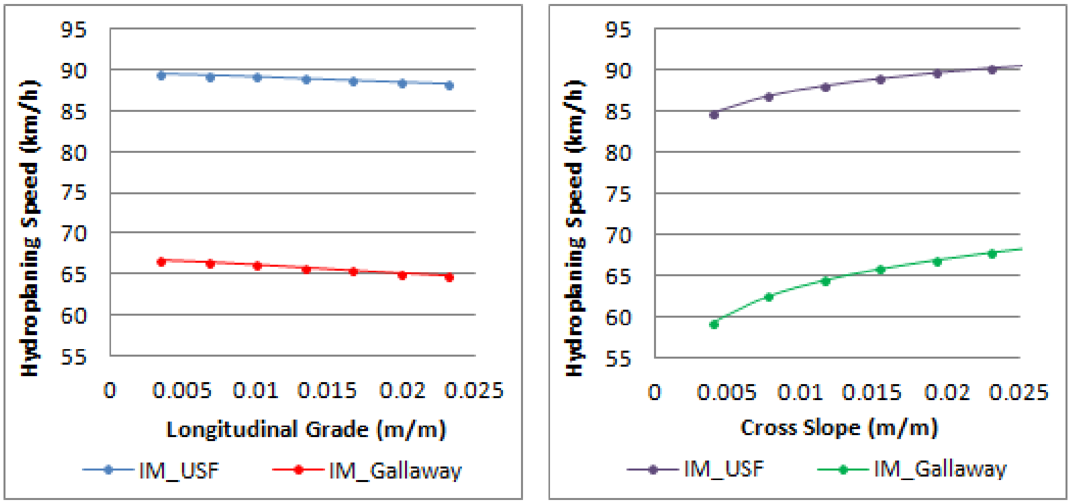

(a) (b)

Figure 6.2 Sensitivity test for two improved models: (a) longitudinal grade vs. hydroplaning speed; (b) cross slope vs. hydroplaning speed.

The increase in longitudinal grade would diminish the vertical wheel load and extend the flow path length. Both the decrease in vertical load and the increase in flow path length would reduce the hydroplaning speed. Therefore, as Figure 6.2a shows the hydroplaning speed goes shown with the increase of the longitudinal grade.

Typically the increase in cross slope would diminish the vertical wheel load and shorten the flow path length. These two results have contrary effect on hydroplaning speed: the diminished vertical load reduce the hydroplaning speed, while the shortened flow path length increase the hydroplaning speed. Figure 6.2b shows that hydroplaning speed goes up with the increase of the cross slope, indicating the effect of flow path length on hydroplaning speed is greater than that of wheel load.

6.2 Case Study

6.2.1 Test Site

A flexible pavement section located in Spavinaw, Oklahoma is chosen to demonstrate the hydroplaning speed prediction on pavements with large slopes. The chosen test section with a length of 2.7 mile has five horizontal curves, starting from the GPS coordinates (36.329175, -95.081696) and ending with the GPS coordinates (36.351066, -95.062796). In addition, the test lane is in excellent condition, with a width of 12ft.

6.2.2 Local Rainfall Intensity

The local rainfall intensity is obtained from National Oceanic and Atmospheric Administration's (NOAA) National Water Service database (NOAA 2015). Table 6.1 shows the precipitation in Spavinaw Station of Oklahoma from NOAA database. The two-year return period storm with duration of five minutes is used in Gallaway WFD model for rainfall intensity acquisition. Based on NOAA database, the rainfall intensity of 5.84in/h is used for the test site.

Table 6.1 Precipitation (90% Confidence Intervals) in Spavinaw Station (NOAA 2015)

Duration (in inches)	Average recurrence interval (years)			
	1	2	5	10
5 min	0.428 (0.343-0.542)	0.487 (0.390-0.618)	0.587 (0.468-0.745)	0.671 (0.532-0.855)
10 min	0.627 (0.502-0.794)	0.713 (0.571-0.905)	0.859 (0.685-1.09)	1.16 (0.890-1.51)
15 min	0.764 (0.612-0.969)	0.870 (0.696-1.10)	1.05 (0.835-1.33)	1.20 (0.950-1.53)
30 min	1.13 (0.906-1.44)	1.29 (1.03-1.64)	1.56 (1.25-1.98)	1.79 (1.42-2.28)
60 min	1.52 (1.22-1.92)	1.74 (1.39-2.20)	2.10 (1.68-2.67)	2.42 (1.92-3.08)
2 hr	1.90 (1.54-2.38)	2.18 (1.76-2.73)	2.65 (2.13-3.32)	3.05 (2.44-3.83)
3 hr	2.15 (1.75-2.67)	2.46 (2.00-3.06)	3.00 (2.43-3.73)	3.46 (2.79-4.32)

6.2.3 Horizontal Curve Safety Evaluation

Curve radius measurement needs the combination of IMU data and the transverse profile data (extracted from 3D texture data). In DHDV system, IMU and 3D texture data are triggered from different sources, so they have different data interval and report format. In order to establish a relationship between IMU and 3D texture data, the common property between them should be identified first.

Note that both of data sets are associated with Distance Measurement Instrument (DMI) pulse, and thereby they can be roughly matched through the recorded DMI pulses. Table 6.2 shows the part of the IMU data such as heading direction, roll, and test speed. Figure 6.3 shows the cross slope or super-elevation at five horizontal curves: the orange line represents the raw data; and the green line represents the calibrated cross slope or super-elevation. By comparing those two values, it can be found that calibrated data is smoother than the raw data, which means the noise (e.g. the abrupt drop) derived from the vehicle body roll is suppressed after calibration.

Table 6.2 Example of IMU Data for Curve Radius Calculation

$\mathrm{D}_{\mathrm{DMI}}$	$\alpha_{\mathrm{heading}}$ (Degree)	α_{Roll} (Degree)	Speed (km/h)	N_Vel (m/s)	E_ Vel (m/s)	L_Acc (m/s^2)	T_Acc (m/s^2)	D_Acc (m/s^2)
7379803	88.06	1.48	53.37	1.59	78.25	0.18	0.03	-0.71
7379803	88.06	1.49	53.36	1.6	78.24	-0.8	0.5	0.39
7380445	88.07	1.5	53.36	1.6	78.24	-0.3	-0.1	0.28
7381089	88.07	1.53	53.37	1.59	78.26	1.23	1.87	0.81
7381949	88.09	1.57	53.37	1.56	78.26	-0.7	0.69	-2.04
7381949	88.09	1.57	53.37	1.55	78.26	-0.2	-0.5	-2.76
7382804	88.1	1.58	53.36	1.51	78.24	1.35	2.32	-0.05
7382804	88.1	1.59	53.36	1.52	78.25	0.58	-0.1	0.08
7383019	88.1	1.6	53.37	1.53	78.26	0.35	-1.2	0.85
7383235	88.11	1.61	53.38	1.55	78.27	0.49	-1.1	-1.39
7383881	88.11	1.61	53.37	1.53	78.26	-1.2	0.14	-1.47
7383881	88.11	1.62	53.36	1.51	78.25	-0.8	3.73	-0.57

Note: N_Vel=North velocity; E_Vel=East velocity; L_Acc=Longitudinal acceleration; T_Acc=Transverse acceleration; D_Acc=Down acceleration.

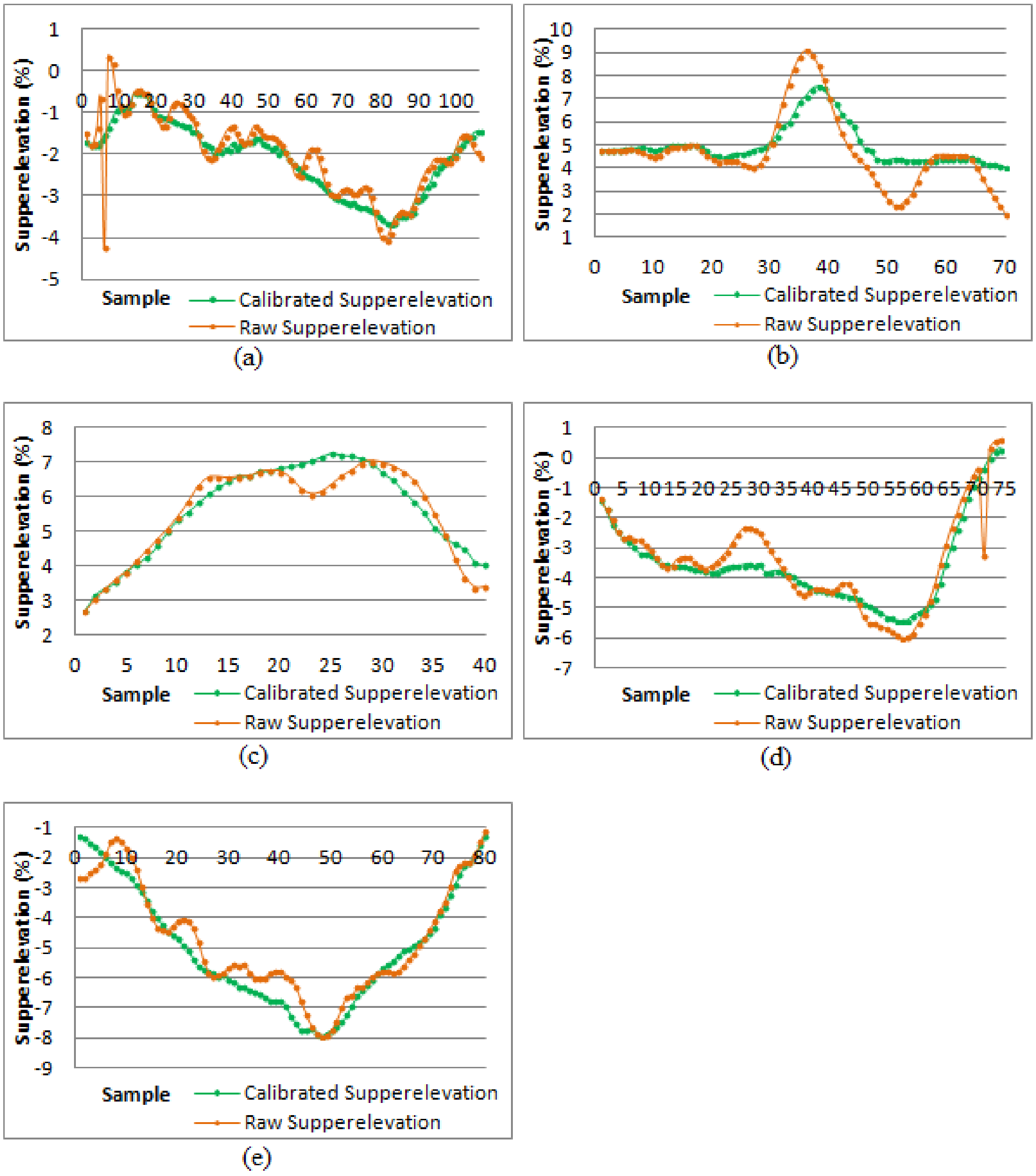

Figure 6.3 Raw and calibrated super-elevation data on (a) curve1; (b) curve2; (C) curve3; (D) curve4; (e) curve 5

6.2.3.1 Curve Identification and Length Measurement

The start-end points (PC and PT) of a curve are the most paramount factors for a curve identification and curve length calculation. In this study the start-end points of each curve are determined by the change of heading angle. Figure 6.4 shows the heading angles of DHDV traveling on five curves, which is measured with the IMU system. As a rule of thumb, the simple horizontal curve can be identified when the heading angles linearly increase or decrease, and the two points that start and end the changes are considered as the PC and PT of the simple curve, respectively. For example, the change of heading angles at curve 1 starts at the sample #73 and ends with sample #209, so sample #73 and #209 are considered as the PC and PT of the curve and the curve length is computed with a length of 310m since each sample length is 2.28m. Similarly, the curve lengths at curve 2, 3, 4, and 5 are computed as well, with values of 187m, 198m, 264m, and 262m, respectively.

6.2.3.1 Curve Radius Estimation

Figure 6.5 shows curve radius estimated from four abovementioned methods. Herein, the ground truth of the radius of five curves measured by Chord Length method are 168m, 153m, 183m, 143m, and 111m, respectively. Analysis of Variance (ANOVA) is used to test the accuracy of Kinematic method, Geometry method, and Lateral Acceleration method for curve radius measurement, and the curve radius measured by satellite pictures is considered as control variable. The mostly widely used distinct level, $\alpha = 0.05$, is selected as distinct level in this study. The significant difference is considered as "existence" if the distinct of level is smaller than 0.05.

Table 6.3 shows the ANOVA test results for three methods. According to the distinct level ($\alpha = 0.05$), the difference between the control variable and the measurements of three methods are not significant, which means all of three methods have good accuracy in curve radius measurement. It can be observed that the radius calculated from Kinematic method has the least difference with the ground truth, and followed by Geometry method and Lateral Acceleration method.

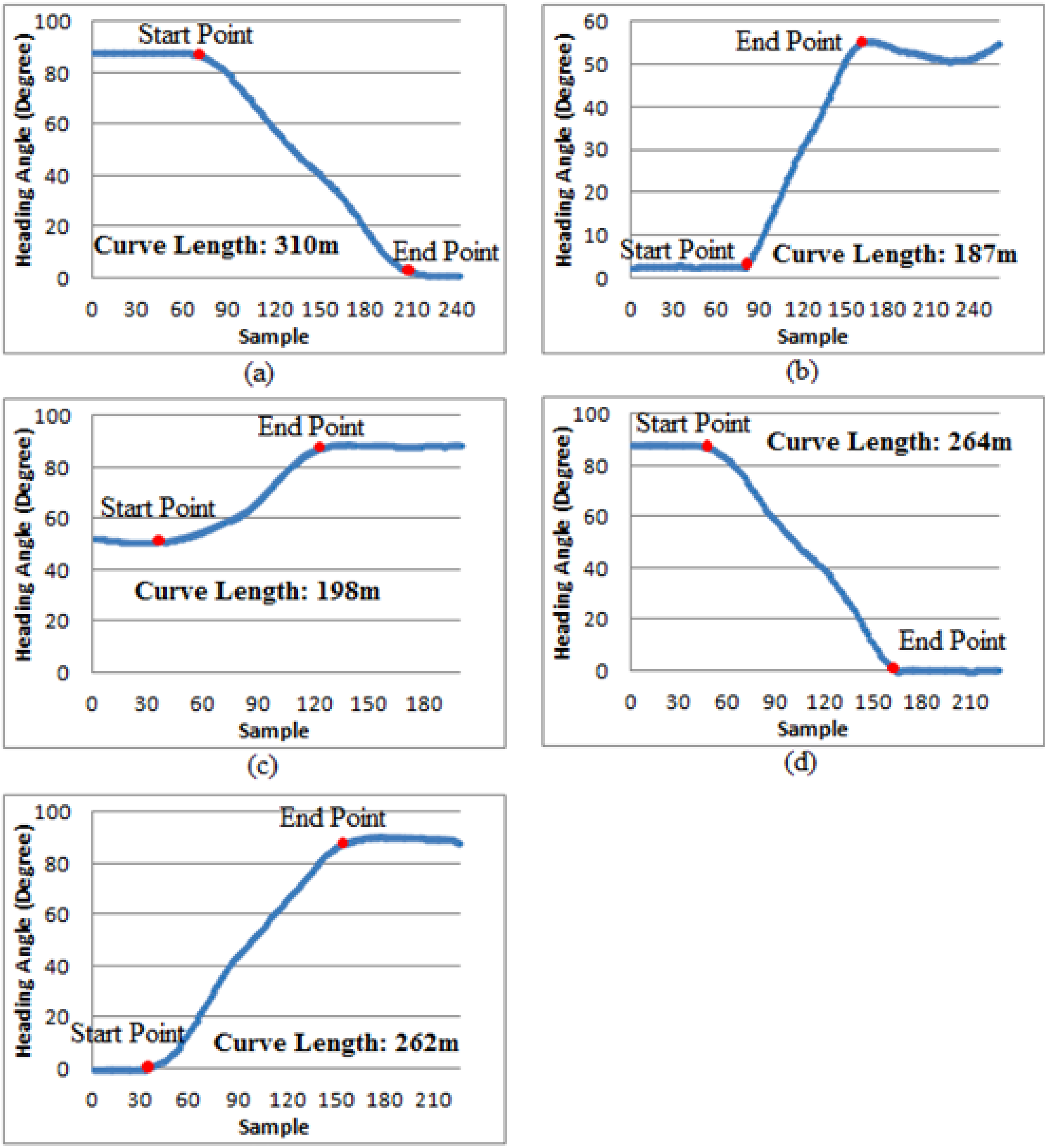

(a) (b) (c) (d) (e)

Figure 6.4 Start-end points determination using change of heading

Table 6.3 ANOVA test results for three horizontal curve measuring methods

Method	T-value	P-value	Significant Difference
Kinematic Method	0.34	0.7357	No
Geometry Method	0.57	0.5703	No
Lateral Acceleration Method	0.69	0.4057	No

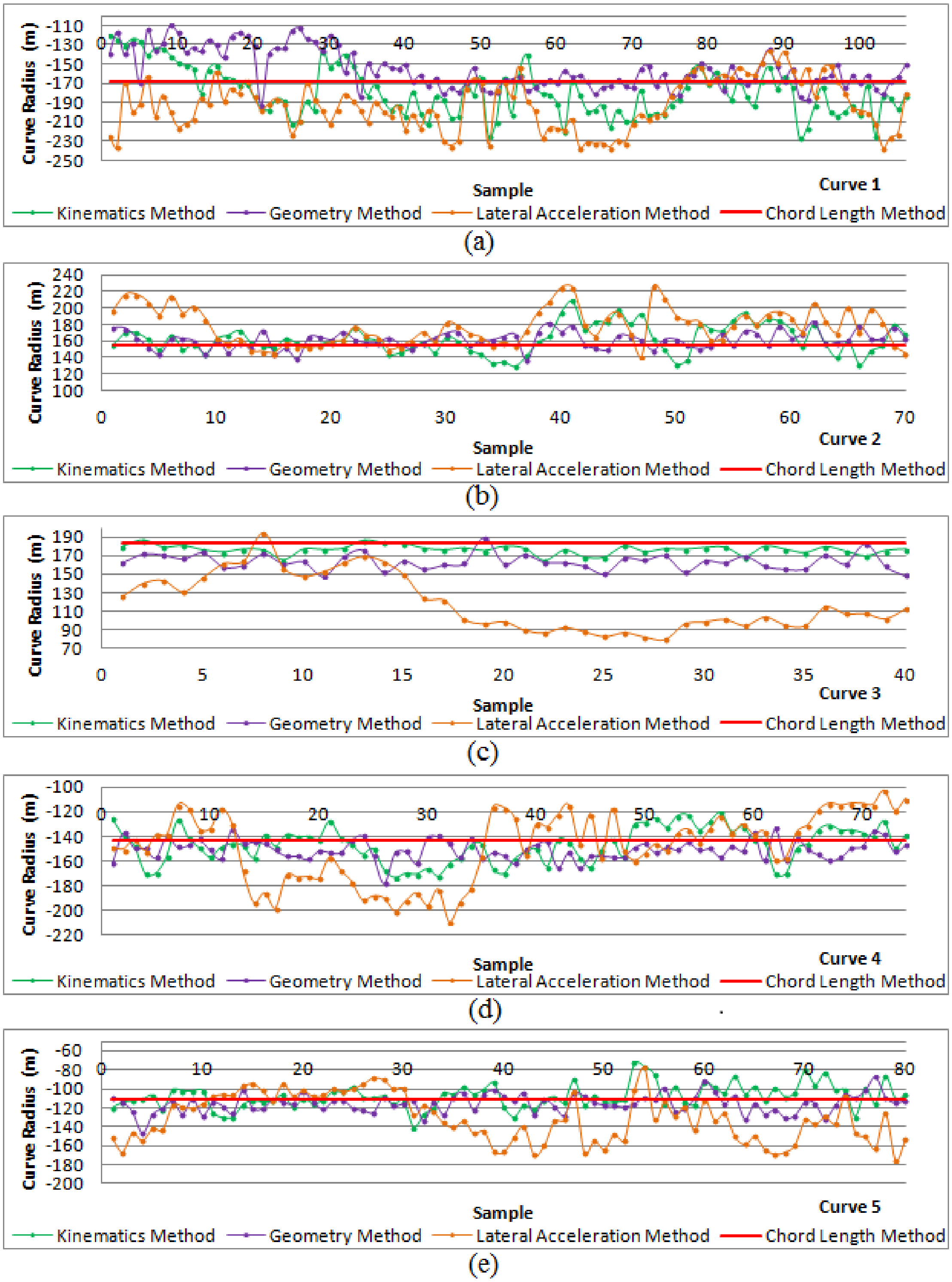

Figure 6.5 Curve radius calculated from four methods at: (a) curve 1; (b) curve 2; (c) curve 3; (d) curve 4; (e) curve 5.

6.2.3.2 *Curve Safety Analysis*

A curve safety analysis model developed by Fitzpatrick et al is applied to predict the safe driving speeds and crash rate of the curves. This model describe the relationships between curve radius and crash frequency based on the crash data on two-lane rural highways (Fitzpatrick et al 2000). Equations 6.7-6.9, are used to compute the curve total crash rate and safe driving speeds. In this study the tangent speed limit (65mph) of the test site is considered as the 85th percentile tangent speed of passenger cars.

$$\mathrm{CR} = \mathrm{CR_b} \times \mathrm{AMF_{sr}} \tag{6.7}$$

$$\mathrm{AMF_{sr}} = \mathrm{e}^{0.078(\mathrm{V_{t,85,pc}} - \mathrm{V_{c,85,pc}})} \tag{6.8}$$

$$\mathrm{V_{c,85,pc}} = 104.77 - \frac{3576}{\mathrm{R}} \tag{6.9}$$

Where: CR: the total curve crash rate, crashes/million-vehicle-km, crashes/mvk; $\mathrm{CR_b}$: the base crash rate (=0.42), crashes/million-vehicle-km; $\mathrm{AMF_{sr}}$: the accident modification for curve speed reduction; $\mathrm{V_{t,85,pc}}$: the 85th percentile tangent speed of passenger cars, km/h; $\mathrm{V_{c,85,pc}}$: the 85th percentile curve speed of passenger cars, km/h; R: the curve radius (m).

Table 6.4 Curve Safety Evaluation for Test Sites

	Curve 1	Curve 2	Curve 3	Curve 4	Curve 5
$\mathrm{V_{c,85,pc}}$ (km/h)	83.47722	81.38989	85.22237	79.75505	72.5441
R (m)	168	153	183	143	111
$\mathrm{AMF_{sr}}$	5.358996	6.30655	4.676991	7.164268	12.5731
CR (crashes/mvk)	2.250778	2.648751	1.964336	3.008992	5.280704

The safety evaluation results at the five curves are shown in Table 6.4. The safe driving speeds at the five curves are estimated to be around 80km/h, and the estimated crash rates at five curves are ranked as follows from low to high: Curve3, Curve1, Curve2, Curve4, and Curve5.

6.2.4 Cross Slope and Longitudinal Grade

As Figure 6.6a shows, the maximum longitudinal grade is 12.03%, and the standard deviation is 2.48. Figure 6.6b shows the calibrated cross slopes. The cross slope presents negative values at left turn curves and positive values at right turn curves.

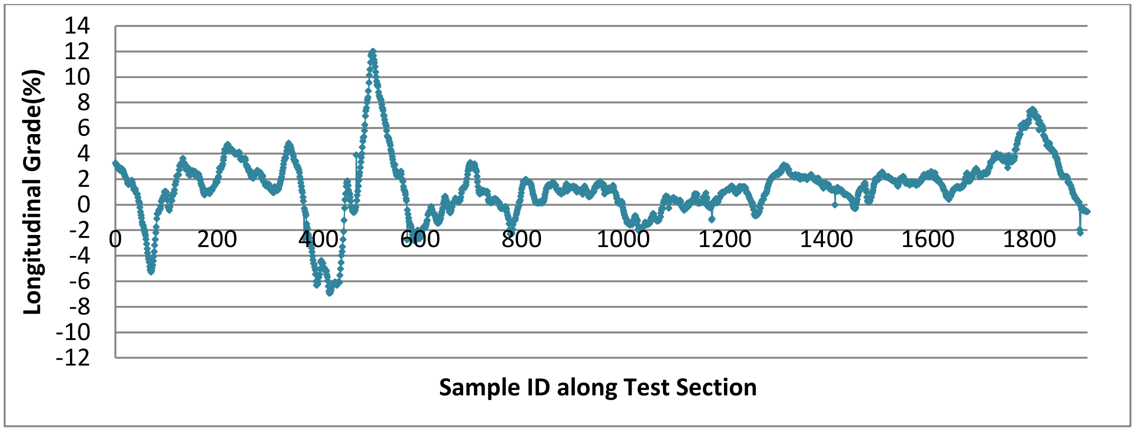

(a)

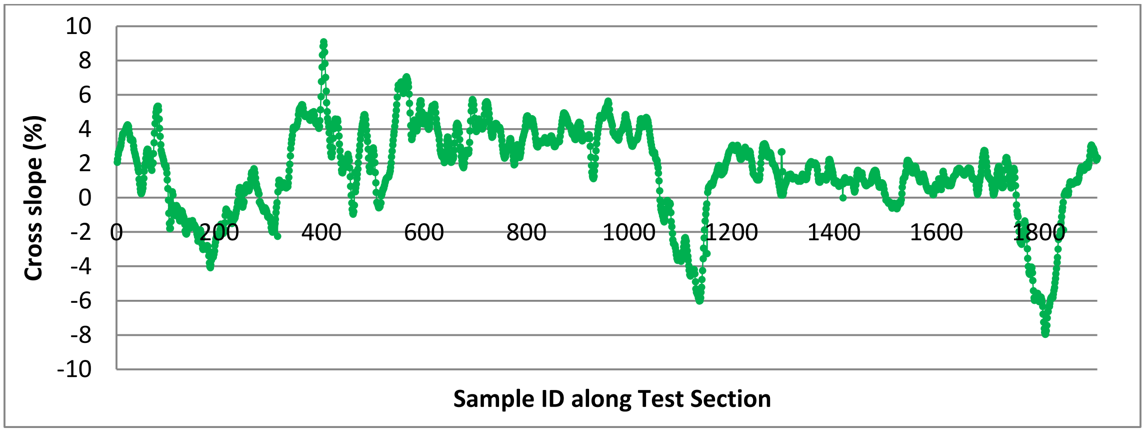

(b)

Figure 6.6 Pavement geometry of test site: (a) longitudinal grade; (b) cross slope.

In this test site, curves #1, #4, and #5 belong to left turn curve, while curves #2 and #3 belong to right turn curve. The statistical results of the calibrated cross slopes on test site are given as follows: (1) the average cross slope on the straight road segments is

1.94%; (2) the average cross slope of curve #1, #2, #3, #4, and #5 are -2.06%, 4.96%, 5.80%, -3.81%, and -5.01%, respectively. The results confirm that there are larger cross slopes at road curves than on straight road segments.

6.2.5 EMTDs and WFDs

Figure 6.7a shows the EMTDs with an average value of 1.20 mm, and Figure 6.7b shows the corresponding WFDs with an average value of 1.73mm and the maximum value of 8.52 mm. The WFD is calculated with Gallaway WFD model based on pavement texture depth, flow path slope, and local rainfall intensity.

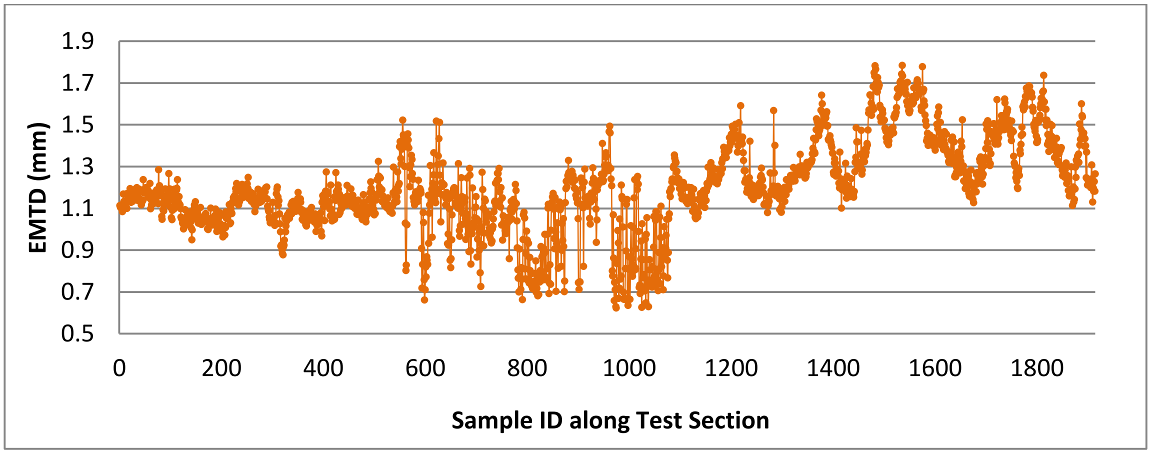

(a)

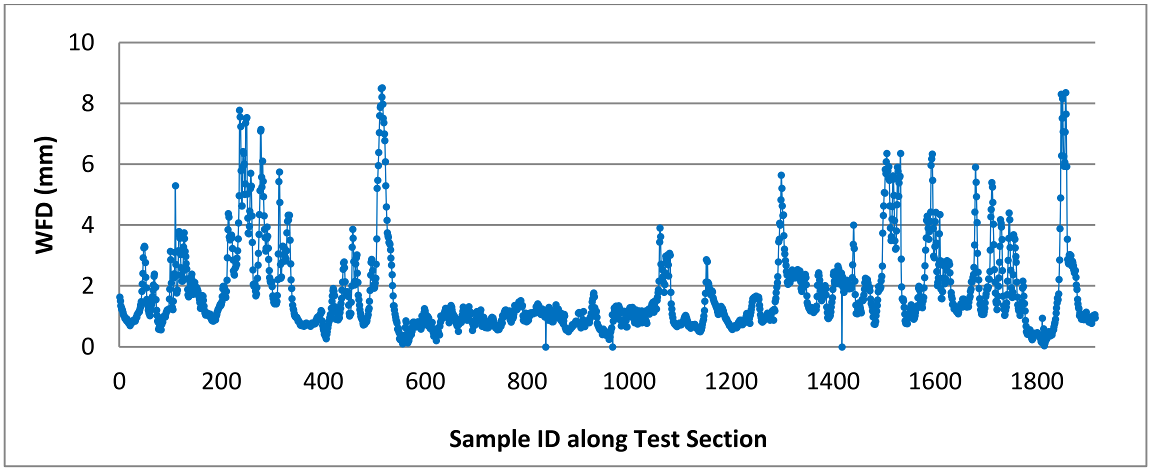

(b)

Figure 6.7 EMTDs and WFDs of test site: (a) EMTDs; (b) WFDs.

6.2.6 Hydroplaning Speed Estimation

Part of the calculated WFD, EMTD and IMU data for hydroplaning speed prediction is given in Table 6.5. Gallaway model, USF model, the modified Gallaway model, and the modified USF model are utilized to predict hydroplaning speed, respectively, as shown in Figure 6.8a. Results indicate the predicted hydroplaning speeds from original Gallaway and USF model are around 87mph and 165km/h, respectively, which are approximately 30mph higher than those predicted from the modified Gallaway model (60mph) and modified USF model (56mph). The results also show as expected that the hydroplaning speeds at curves of the five horizontal curves in Figure 6.8a are lower than that on the straight road sections.

Table 6.5 Part of 3D Imaging Data and IMU Data for Hydroplaning Speed Calculation

Sample ID	WFD (mm)	EMTD (mm)	Cross Slope (%)	Longitudinal Grade (%)
1	1.64	1.12	2.07	3.27
2	1.51	1.11	2.26	3.18
3	1.35	1.11	2.54	3.10
4	1.30	1.10	2.68	3.12
5	1.23	1.11	2.82	3.07
6	1.21	1.09	2.87	2.89
7	1.13	1.12	2.95	2.78
8	1.05	1.17	3.05	2.77
9	1.03	1.14	3.23	2.72
10	1.00	1.10	3.44	2.67
11	0.93	1.12	3.64	2.71
12	0.94	1.11	3.74	2.81
13	0.94	1.10	3.76	2.85
14	0.86	1.17	3.79	2.79
15	0.92	1.10	3.83	2.76

6.2.7 Potential Hydroplaning Segment Detection

Identification of hazardous locations with hydroplaning potential is based on the comparison of estimated hydroplaning speed with posted speed of the road section (Luo et al. 2014). At the test site, speed limits are 50mph on straight sections and 35mph on road curves. The average values of estimated hydroplaning speeds from the modified Gallaway and USF models are used to detect potential hydroplaning segments, as shown in Figure 6.8a.

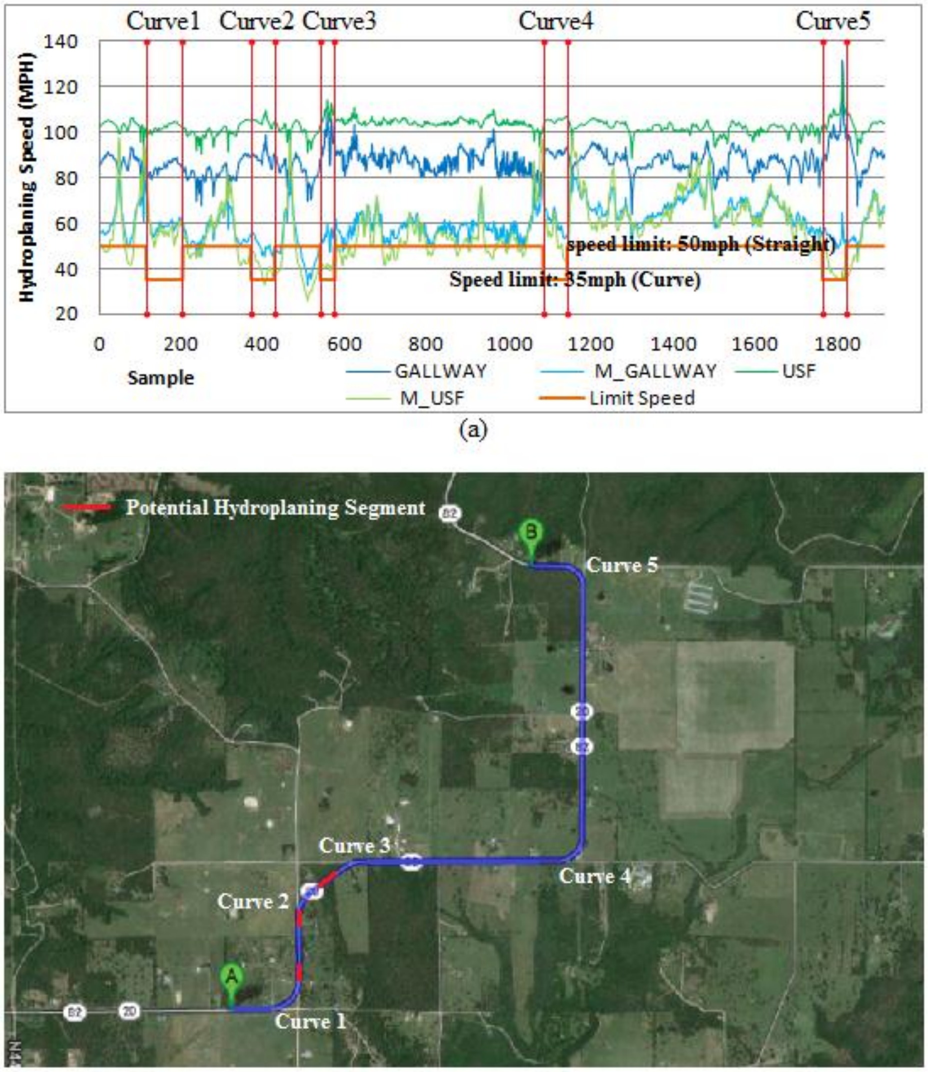

(a)

(b)

Figure 6.8 Potential hydroplaning detection: (a) hydroplaning speed; (b) hydroplaning hazardous segments.

Since the predicted hydroplaning speeds at the five curves are higher than posted speed limit, there is low hydroplaning risk at the five curves for vehicles operating at speed limit. However, for several segments of the test site, the predicted hydroplaning speeds are lower than posted speed limit. Therefore, these segments can be identified as potential hazardous segments for hydroplaning risk, as marked with red line in Figure 6.8b. To minimize traffic accidents caused by hydroplaning, highway agencies can post a reduced speed sign at these locations, or take other remedial actions, such as installing High-Friction Surface Treatment (HFST) (Shah et al. 2014).

6.3 Summary

This chapter presents the application of modified Gallaway and USF models on hydroplaning speed prediction. The original prediction models do not consider effects of super-elevation and large longitudinal grade on vertical wheel load, however, the change of vertical wheel load would result in the change of the predicted hydroplaning speeds. To overcome this limitation, the original models would be modified based on mechanic theory.

In this study the IMU heading data is used to identify the locations of the potential horizontal curves. The curve lengths are estimated based on the start-end points of the identified horizontal curves. The horizontal curve radius are estimated with three approaches namely kinematic method, Geometry method, and Lateral acceleration method. The ground truth of curve radius is obtained by satellite pictures. ANOVA test results indicate all three methods have good accuracy in curve radius measurement, among which the result from Kinematic method has the best agreement with the ground truth. Finally, the Fitzpatrick's model is applied for curve safety analysis on horizontal curves.

The EMTD is computed on test section with 1mm 3D texture data on the entire lane. IMU data and 3D laser image data are combined together to eliminate impacts of vehicle vibration on cross slope measurement. The rainfall intensity used in prediction models is obtained from NOAA database. WFD and hydroplaning prediction models are modified based on the fact that effects of cross slope and longitudinal grade on wheel load and flow path length should be considered, it is found that hydroplaning speed decrease with the increase of the longitudinal grade, but increase with the increase of the cross slope. Results also indicate the predicted hydroplaning speeds from original Gallaway and USF models are approximately 30mph higher than those predicted from the modified Gallaway and USF models. In addition, the predicted hydroplaning speeds at horizontal curves are lower than that on the straight road sections.

By comparing estimated hydroplaning speed with posted speed, pavement segments having potential hydroplaning risk can be identified. As a result, highway agencies can post a reduced speed sign at these locations, or take other remedial actions to avoid hydroplaning related traffic accidents.

CHAPTER 7. HYDROPLANING SPEED PREDICTION ON RUTTING PAVEMENTS

7.1 Model Preparation

The presence of pavement rutting is hazardous to drivers and road users since the rutting would be functioned as the reservoir or small puddle during rainy weather. The ponding water on pavement rutting might cause a series of hydroplaning related safety issues. However, the effects of pavement rutting on water film depth are negligible in the currently used hydroplaning speed prediction models. In this study, effects of pavement rutting on water film depth would be examined on the chosen test section during- and after- precipitation, and subsequently a new WFD prediction model is developed. Based on new WFD model, the hydroplaning speeds on rutting pavements can be predicted.

7.1.1 Effects of Cross Slope on Rutting Ponding

Wheel path depressions or rutting interrupt the normal flow pattern of water and can, if excessive, completely alter the drainage pattern on pavement surfaces. Ponding of water is prevalent in the depressions that may cause hydroplaning or less of vehicle control.

Studies indicate hydroplaning can occur in rutting areas when the length of the rut is 9.144m (30ft) or greater. However, with normal cross slope (≤ 2.5%), rut depths of 0.61cm (0.24 in) or less do not significantly contribute to a higher risk of hydroplaning (Balmer and Gallaway 1983). In addition, the ponding can be partially or fully relieved through drainage if the pavement cross slope or longitudinal grade is large enough. Based on the two assumptions: (1) the minimum cross slope to provide decent drainage capacity is 0.5 percent and (2) the wheel-path depression width is 600 mm (24 in) (Balmer and Gallaway 1983), the allowable wheel-path depressions are calculated by Equation 7.1.

$$WPD = S\frac{W}{2} - 0.005\frac{W}{2} \tag{7.1}$$

Where, WPD: wheel-path depression, mm (in), as shown in Figure 7.1; S: cross slope, m/m; W: Width of the wheel track, mm (in), as shown in Figure 7.1.

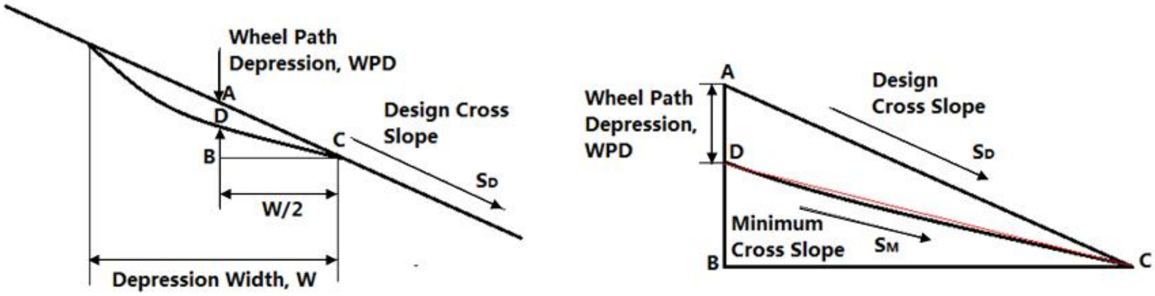

Figure 7.1 Wheel path pavement depression geometry

Table 7.1 Allowable wheel path depression (Balmer and Gallaway 1983)

Pavement Cross Slope, %	Maximum Wheel Path Depression	
	mm	In.
1	1.5	0.06
2	4.5	0.18
3	7.5	0.30
4	10.5	0.41

Table 7.1 shows the admissible values when the influence of cross slope on drainage is considered. Pavement maintenance, resurfacing, or rehabilitation is required whenever the depressions exceed these depth.

7.1.2 Rutting Water Film Depth Calculation

Based on intensity and duration of the storm, the water film depth within wheel path can be estimated under three scenarios: 1) the onset of storm events: water film on non-rutting areas has not been formed yet; 2) during storm events: the rutting pond have been filled up, and the water film on non-rutting areas have been formed, and 3) after storm events: the water on non-rutting areas have been drained off, but some water may be still trapped by the pavement rutting. Therefore, the rutting water film depth can be calculated under these three scenarios. The model developed for water film depth calculation on rutting pavement is termed as 3S-WFD model.

7.1.2.1 Onset of Storm Event

At the onset of storm events, the rainy water would discharge into the rutting pond before they start to develop a water film on pavement surface, so the rutting water film depth would increase along with the storm event. This period before the storm event starts to develop water film on non-rutting areas, can be considered as the “onset of storm event”. In this scenario, the maximum rutting water film depth would be equivalent to the rutting depth, as shown in Equation (7.2).

$$WFD_o \leq D_{rut} \tag{7.2}$$

Where, WFD_o: rutting water film depth at the onset of store event, mm; D_{rut}: rutting depth, mm.

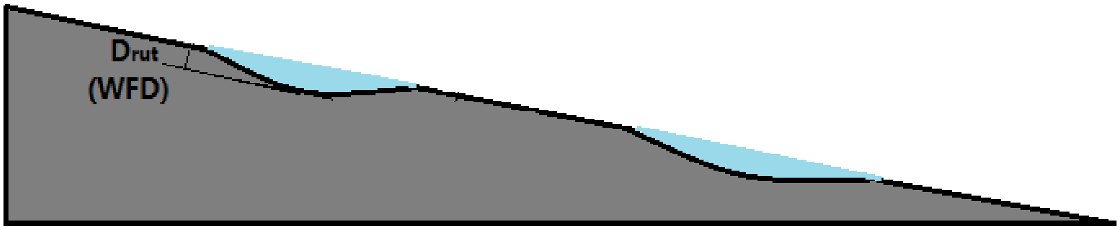

Figure 7.2 Rutting water film depth at the onset of storm event

7.1.2.2 During storm events

Once the rutting ponds are filled up, the redundant rainy water would start to flow on pavement surface so that the water film are developed. The rainfall intensity is the important factor to determine whether the water film have been formed or not on non-rutting areas. Typically the minimum rainfall intensity that is required to develop water film on non-rutting areas can be determined based on the Gallaway WFD model with the assumption of water film depth equivalent to zero. In this study the minimum rainfall intensity forming water film on non-rutting areas are termed as the reference rainfall intensity, and it can be calculated by Equation 7.3.

$$\mathrm{I} = [\frac{(\mathrm{WFD} + \mathrm{TXD}) \times \mathrm{S_c}^{0.42}}{\mathrm{z} \times \mathrm{TXD}^{0.11}\mathrm{L_f}^{0.43}}]^{1.695} \tag{7.3}$$

Where, WFD: Water film depth in mm on pavement surface (0mm); TXD: Pavement texture depth, mm; z: 0.01485 (Constant); $\mathrm{L_f}$: Pavement flow path length, m; $\mathrm{S_c}$: Pavement cross slope, m/m.

When the actual rainfall intensity is larger than the reference rainfall intensity, the redundant water cannot rapidly run off pavement surface so that the water film are formed, as Figure 7.3 shows.

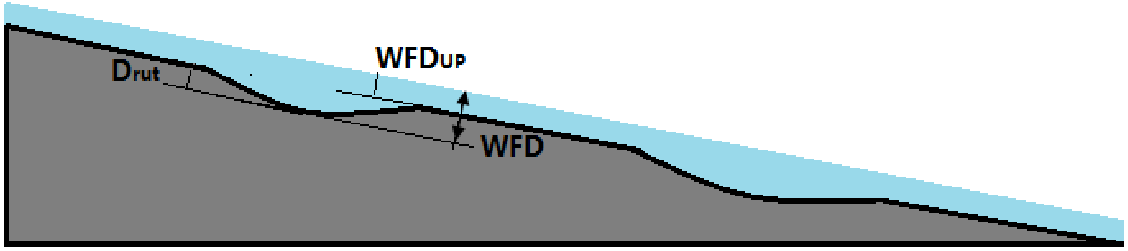

Figure 7.3 Rutting water film depth during storm event

In this case the rutting water film depth is the result of rutting depth plus the water film depth on non-rutting area, as mathematically described in Equation 7.4. In this Equation, the water film depth on non-rutting area is calculated by Gallaway WFD model.

$$WFD_d = WFD_{NR} + D_{rut} \tag{7.4}$$

Where, WFD_d: rutting water film depth during storm event, mm; D_{rut}: rutting depth, mm; WFD_{NR}: water film depth on non-rutting area, which is calculated by Gallaway WFD model, mm.

7.1.2.3 After storm events

When the storm event stops, most of rainy water can drain off the pavement surface except some are trapped by pavement rutting, as illustrated in Figure 7.4a. In this case effects of cross slope on rutting pond should be considered. Typically the cross slope and the calculated rut depth are combined together to determine whether there is the trapped water within rutting areas after storm event, as calculated by Equation 7.5.

$$WFD_a = AB - L \times cross\ slope \tag{7.5}$$

Where, WFD_a: rutting water film depth after storm event; AB: see Figure 7.4a (approximate to the rut depth) ; L: see Figure 7.4a (approximate to the half of the rut width).

If the rutting water film depth from Equation (7.5) is greater than zero, as shown in Figure 7.4a, which indicates the rutting ponding is partially relieved or discharged by the cross slope and there is still some redundant water within rutting areas. The trapped water might cause the potential hydroplaning risks. If the calculated rutting water film depth is no larger than zero, as shown in Figure 7.4b, which represents the rutting ponding is fully relieved or discharged due to effects of cross slope, and thus there is no hydroplaning risks in this situation.

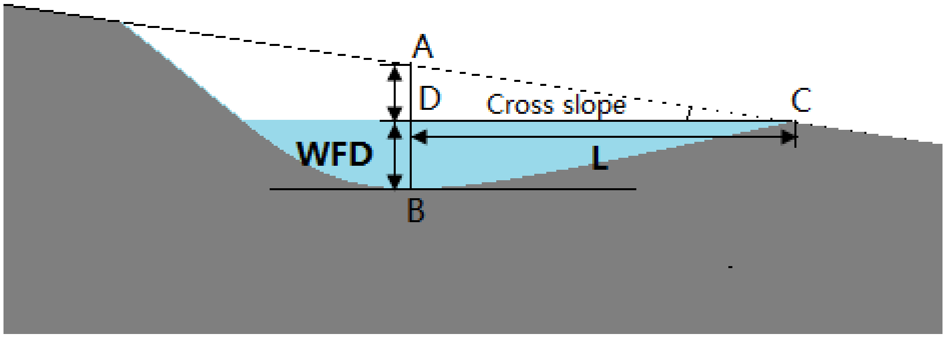

(a)

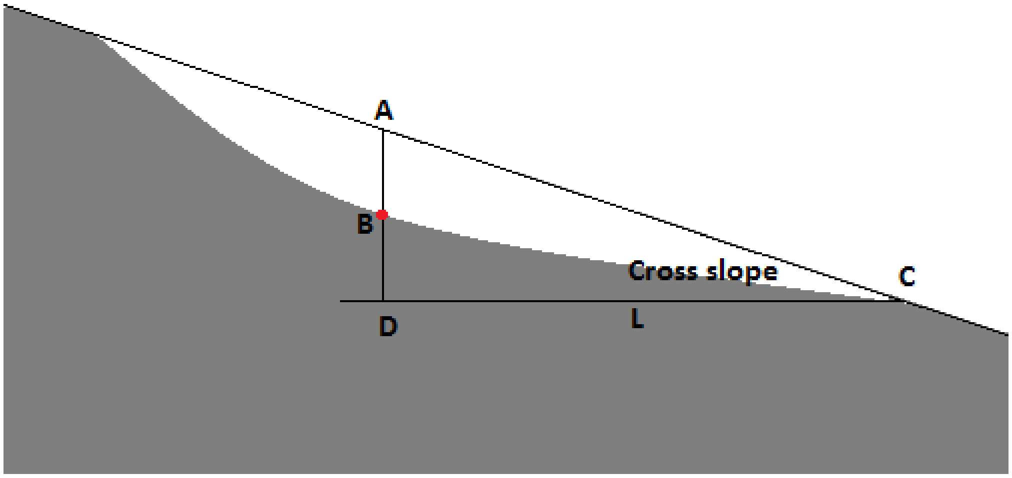

(b)

Figure 7.4 Rutting water film after storm events (a) with standing water; (b) without standing water

7.1.3 Hydroplaning Speed Estimation

Once the rutting water film depth are determined, the following task is to incorporate the calculated WFDs into the Gallaway model to predict hydroplaning speeds. In this study the hydroplaning speeds under the three scenarios are exported for safety evaluation purpose. By comparing the posted speed limit with estimated hydroplaning speed, these segments with potential hydroplaning risks are identified out. To reduce rutting-related crashes, the surface maintenance measures can be taken on the hazardous segments.

7.2 Case Study

7.2.1 Test site

A flexible pavement section located in Alameda Street Los Angeles, California is chosen as the test bed for hydroplaning related safety evaluation. This section starts from the GPS coordinates (34.02497, -118.240549), and ends with the GPS coordinates

(34.011067, -118.23974), with a length of 4 miles, as marked in Figure 7.5. The test lane are in poor condition and has a width of 12ft. Severe rutting occurs on some short segments.

7.2.2 Local Rainfall Intensity

The local rainfall intensity at the test site is obtained from National Oceanic and Atmospheric Administration's (NOAA) National Water Service database (NOAA 2015). Table 7.2 shows the precipitation in Los Angeles Station California from NOAA database. The two-year return period storm with duration of five minutes is used for rainfall intensity acquisition. Based on NOAA database, the maximum rainfall intensity of 2.8in/hour is used for the test site.

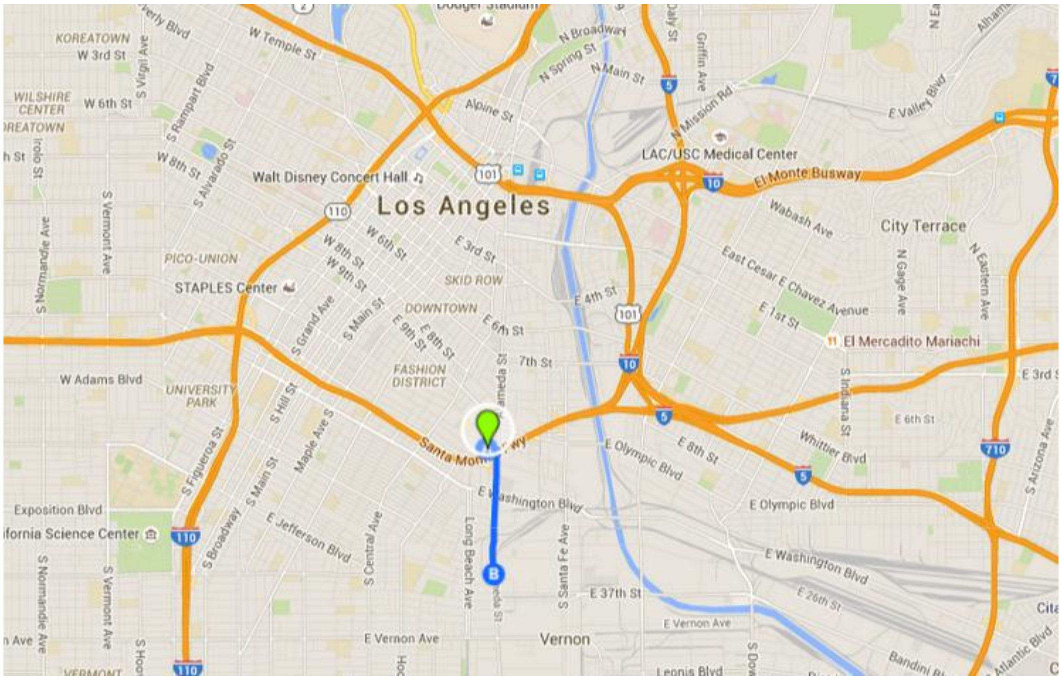

Figure 7.5 Test sites on Los Angeles, California

Table 7.2 Precipitation (90% Confidence Intervals) in Los Angeles Station (NOAA 2015)

Duration (in inches)	Average recurrence interval (years)			
	1	2	5	10
5 min	0.151 (0.126-0.182)	0.194 (0.162-0.234)	0.252 (0.210-0.306)	0.302 (0.249-0.369)
10 min	0.216 (0.181-0.261)	0.277 (0.232-0.335)	0.361 (0.301-0.438)	0.433 (0.357-0.529)
15 min	0.261 (0.219-0.316)	0.336 (0.280-0.406)	0.437 (0.364-0.530)	0.523 (0.432-0.640)
30 min	0.350 (0.293-0.422)	0.449 (0.375-0.543)	0.585 (0.487-0.709)	0.700 (0.578-0.856)
60 min	0.502 (0.420-0.607)	0.645 (0.539-0.780)	0.840 (0.700-1.02)	1.00 (0.830-1.23)

7.2.3 Cross Slope and Longitudinal Grade

The longitudinal grade and cross slope of test site are shown in Figure 7.6 and Figure 7.7 respectively. As Figure 7.6 shows, the maximum longitudinal grade is 2% and the minimum longitudinal grade is -2.18%, which means the test site is in a flat road segment.

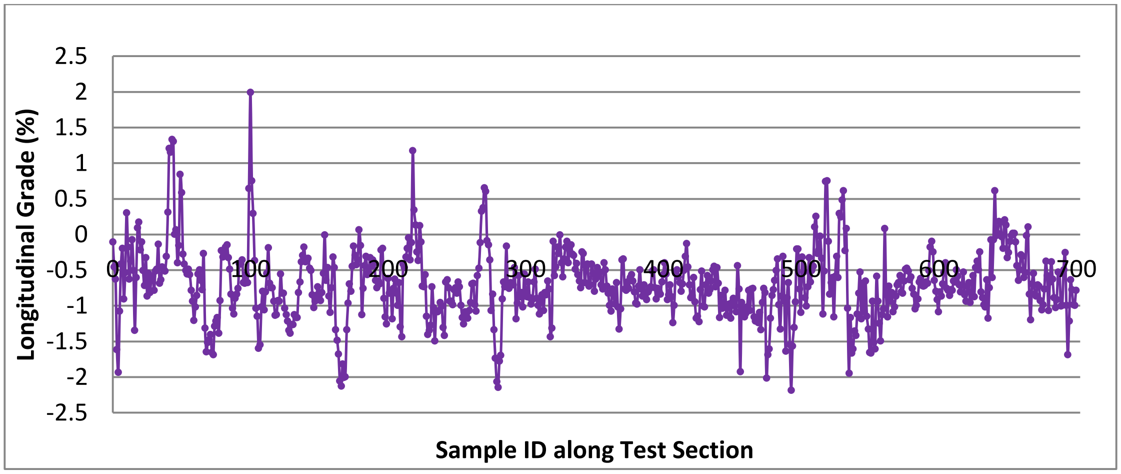

Figure 7.6 Longitudinal grade at the test site

Figure 7.7 shows the raw cross slope and calibrated cross slopes. Comparing the raw cross slope data and calibrated cross slope, the calibrated cross slope is much smoother than the raw cross slope since the errors from survey vehicle body roll has been eliminated. The cross slope in test site is around 1.5%, and the maximum cross slope in test site is 5.11%.

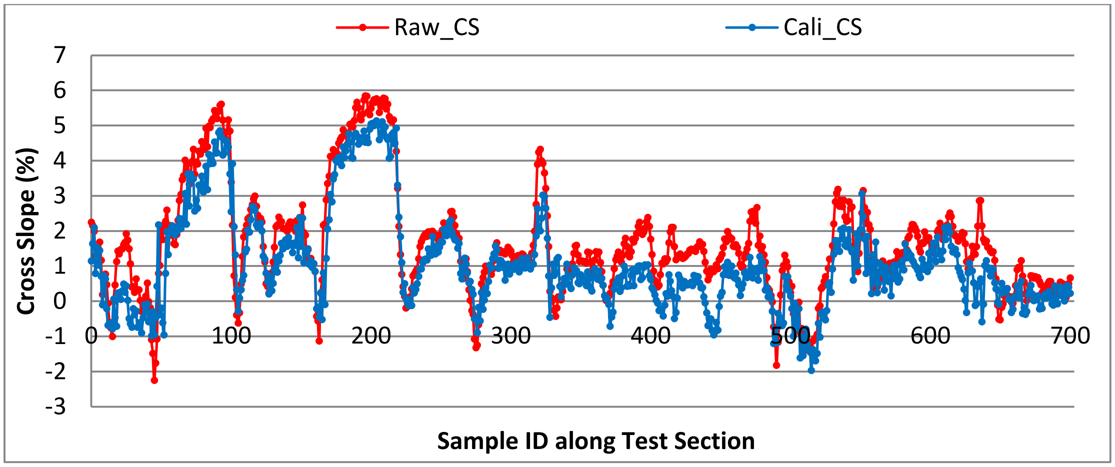

Figure 7.7 Raw and calibrated cross slope at test site

7.2.4 EMTDs and Rutting Depth Calculation

The EMTD on test site are calculated as well and almost all EMTDs are ranged from 0.6-0.8mm with some exceptions such as some EMTD up to 1.44mm, as Figure 7.8 shows.

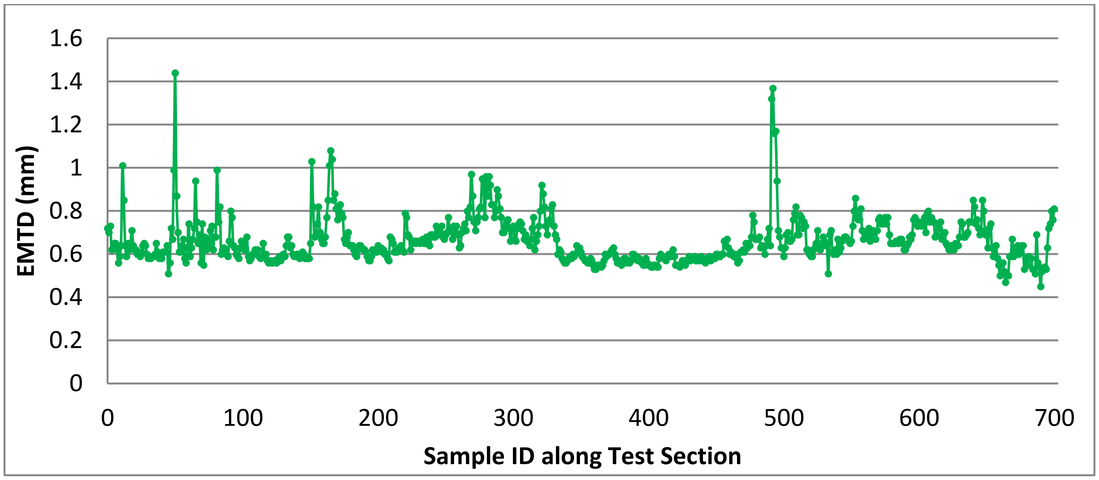

Figure 7.8 EMTD at test site

The occurrence of hydroplaning is dependent on the deepest water film that separate pavement surface and vehicle tires, and thus in this case the maximum value of the left and right rutting depths is used for hydroplaning risk evaluation, as shown in Figure 7.9. Note that the majority of rutting depth for hydroplaning related safety evaluation is around 15mm, with some exceptions such as sample 53, 54, 101, and 632 to 637.

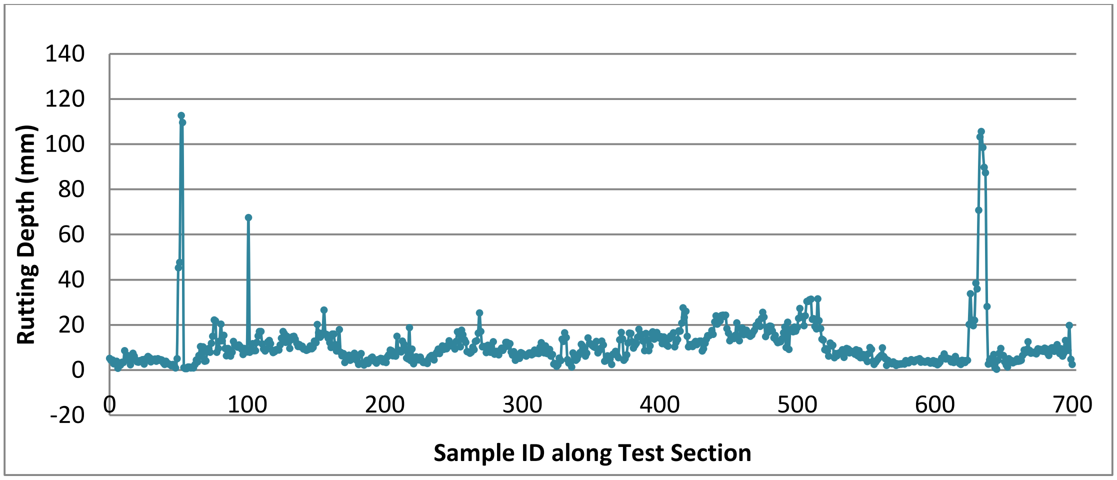

Figure 7.9 The rutting depth distribution on test section

7.2.5 Rutting Water Film Depth Calculation

Figure 7.10 shows the reference rainfall intensity calculated from Gallaway model. The local rainfall intensity of the test site is 2.8 in/h. Note that at several segments (e.g. samples175 to 217) the local rainfall intensity is no less than the reference rainfall intensity during storm event, and thus the water film depth under scenarios 1 and 2 should be considered. However for most segments (e.g. samples 10 to 50), the local rainfall intensity is less than the reference rainfall intensity, and so the water film depth under scenario 1 needs be considered since the water film under scenario 2 would not be developed during store event.

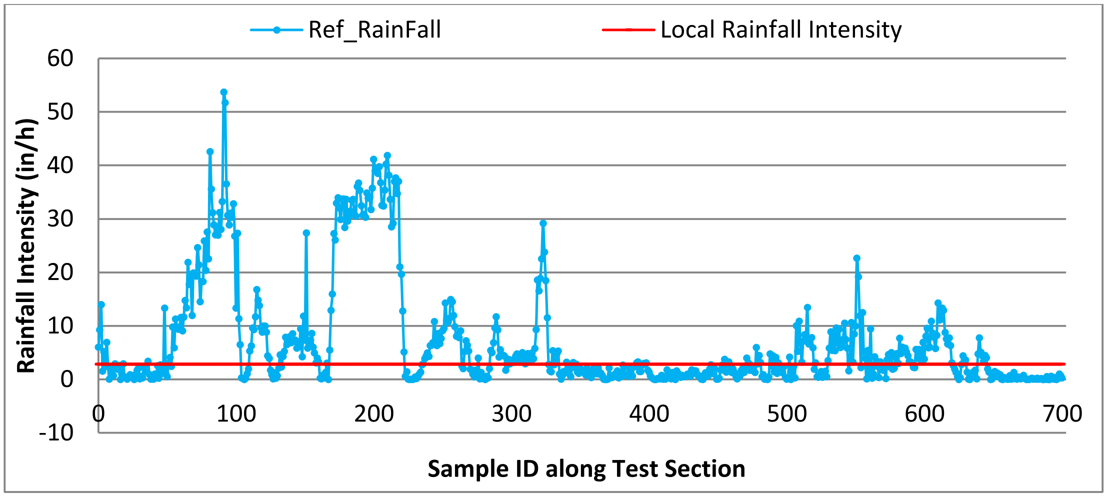

Figure 7.10 Local and reference rainfall intensity along test section

After storm event, the water film depth under scenario 3 would be investigated. Whether developing water film on rutting areas or not depends on the two factors: the rutting depth and the corresponding cross slope. The water film depth calculated from Gallaway WFD model and 3S-WFD model are shown in Figure 7.11.

The Gway_WFD denotes water film depth at non-rutting areas during storm events. The negative Gway_WFD indicates that the rainy water can drain off the pavement surface rapidly under the local rainfall intensity in this area so that the water film will not be developed, as Table 7.3 shows, that is, there is no hydroplaning risks for segments with the negative WFDs.

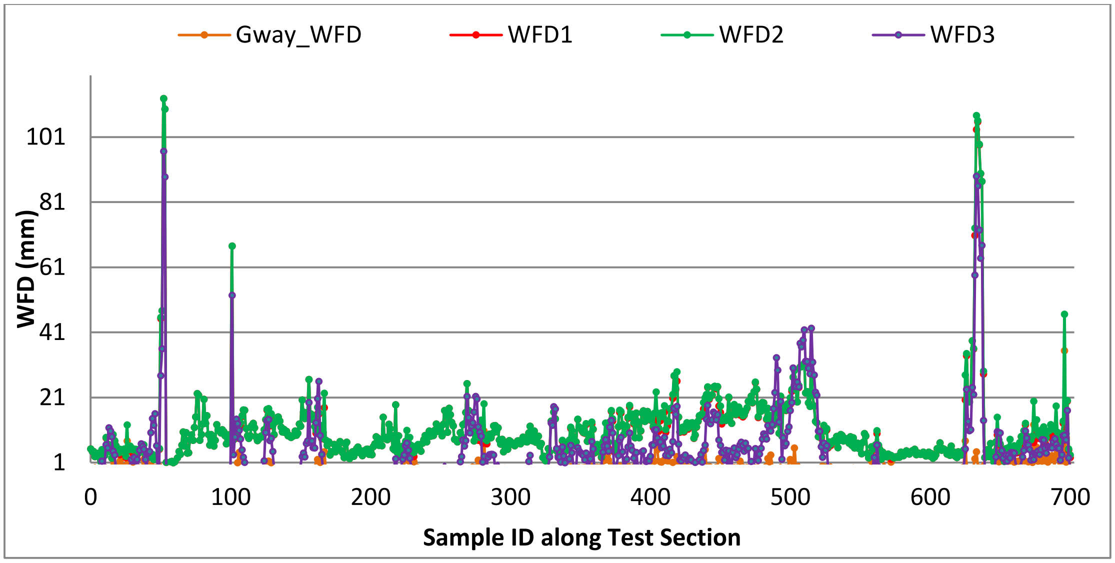

Figure 7.11 WFDs calculated by Gallaway WFD model and 3S-WFD model

In Figure 7.11, WFD1 represents the water film depth at the onset of storm events; WFD2 denotes the water film depth during the rainfall events; and WFD3 stands for the rutting water film depth after the storm events. The presence of rutting increases the water film depth during the storm events, so the WFDs calculated from Gallaway WFD model are smaller than the WFDs calculated from 3S-WFD model under scenarios 1 and 2. Once the storm event stops, Gway_WFD would be reduced to 0. However, due to the presence of wheel depression, some water might be trapped in rutting area. In some road sections the pavement cross slope is large enough to discharge all the ponding in rutting, resulting in the WFD3 is equivalent to 0, as Table 7.3 shows.

Table 7.3 Example of Reference Rainfall Intensity and WFDs on Test Site

Sample ID	Ref_RainFall	Gallaway_WFD	WFD1	WFD2	WFD3
39	0.53	0.37	3.23	3.6	1.99
40	0.04	1.96	2.52	4.47	0
41	0.98	0.3	4.01	4.31	4.08
42	0.29	0.82	3.12	3.94	4.5
43	2.55	0.03	2.66	2.69	10.26

44	0.25	0.96	2.6	3.56	14.59
45	2.75	-0.01	1.97		12.55
46	1.15	0.13	2.53	2.66	16.06
47	1.16	0.12	2.23	2.35	6.25
48	13.33	-0.3	0.96		0
49	1.03	0.2	5.12	5.32	0
50	0.55	0.42	45.27	45.69	27.76
51	3.01	-0.19	47.75		36.01
52	4.11	-0.15	112.83		96.68
53	2.45	-0.01	109.63		88.79
54	9.79	-0.22	1.07		0
55	5.89	-0.18	0.75		0
56	11.3	-0.28	0.68		0
57	9.62	-0.2	1.34		0

7.2.6 Estimation of Hydroplaning Speeds

Once the water film depths under the three scenarios are calculated, the following task is to predict the hydroplaning speeds with Gallway models. Figure 7.12 shows the hydroplaning speed estimation under the scenarios 1 and 2. Due to the low local rainfall intensity (2.8in/h), for some segments the water film will not be formed on non-rutting area during storm event, indicating only situation 1 would happen on these segments. As Figure 7.12 shows, at the onset of the storm events the predicted hydroplaning speeds are lower than speed limits for most segments (e.g. samples 70-180), which means there is high hydroplaning risk on these segments. During the storm event, only several short segments presents the potential hydroplaning risks such as samples 350-500.

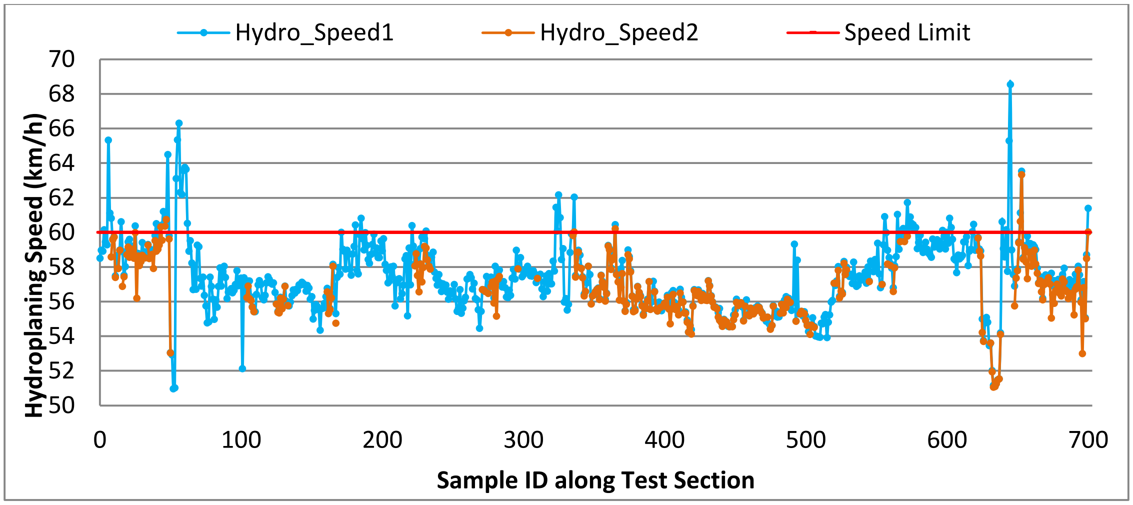

Figure 7.12 Predicted hydroplaning speed under scenarios 1 and 2

Figure 7.13 shows the predicted hydroplaning speeds with the Gway_WFD. Apparently the predicted speeds are greater than those presented in Figure 7.12. By comparing the speed limits with the predicted values, it can be found that there is almost no hydroplaning risk on this section, which are inconsistent with the findings presented in Figure 7.12. The disagreement might be caused by the calculation of Gway_WFD that is exclusive of effects of rutting depth, while effects of rutting depth on WFD are considered in scenarios 1 and 2.

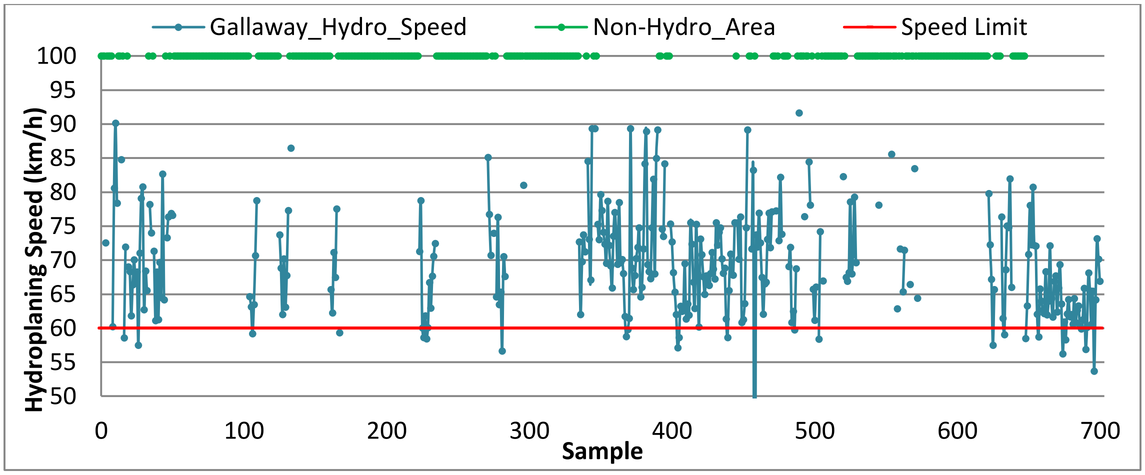

Figure 7.13 Predicted hydroplaning speed with Gway_WFD

Past studies assumed that all rainy water would drain off pavement surface immediately after storm, and thus there is no water film and the resultant hydroplaning risk. However, the presence of wheel depression would make some water trapped in rutting areas after storm events. The trapped water may form a film and cause the hydroplaning risks. Figure 7.14 shows the predicted hydroplaning speeds under scenario 3. Note that the hydroplaning risk is still high on some segments (e.g. samples 272-279) after storm due to effects of the trapped water in pavement rutting.

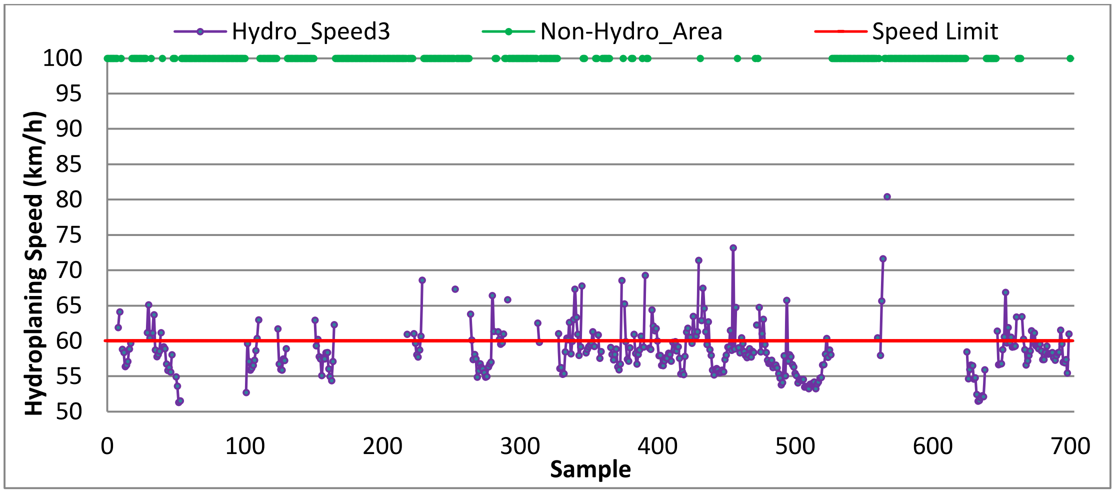

Figure 7.14 Predicted hydroplaning speed under scenario 3

7.2.7 Identification of Potential Hydroplaning Segments

Identification of hazardous locations with hydroplaning potential is based on the comparison of estimated hydroplaning speed with posted speed of the road section (Luo et al. 2014). At the test site, speed limit is 60km/h. During the storm event, if the predicted hydroplaning speed on the road segment is lower than posted speed, the segments can be identified as potential hazardous segments for hydroplaning risk. The potential hydroplaning segments during storm events are marked with red line in the map (Figure 7.15).

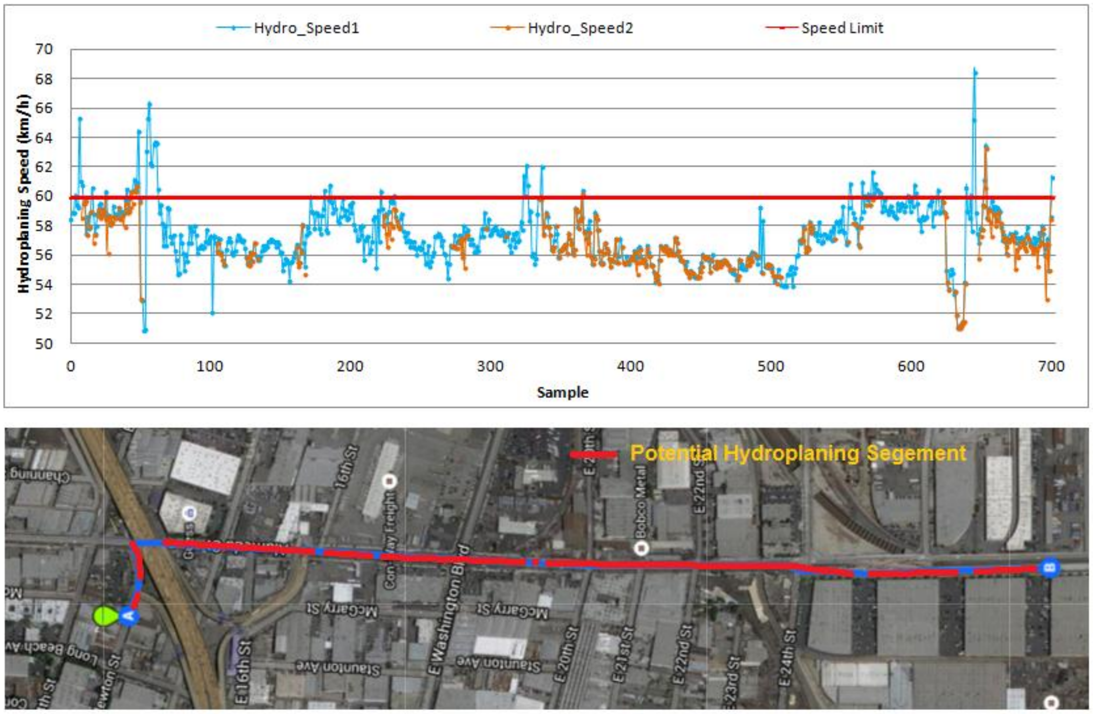

Figure 7.15 Potential hydroplaning segment detection for Scenarios 1 and 2

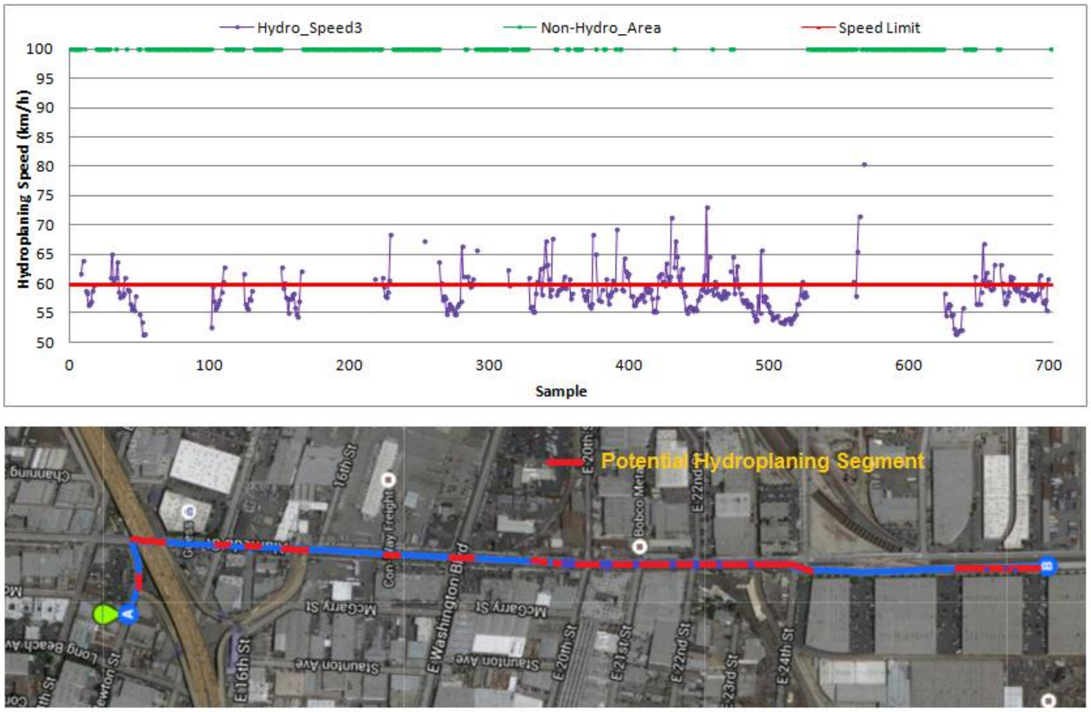

Figure 7.16 Potential Hydroplaning Segment Detection for Scenario 3

Similar with the scenarios 1 and 2, after storm event the potential hazardous segments for hydroplaning are marked with red line in google map (Figure 7.16). To minimize traffic accidents caused by hydroplaning, highway agencies can post a reduced speed sign at these locations, or corrective actions are made for the rutting.

7.3 Summary

This chapter presents the application of Gallway hydroplaning speed prediction model on rutting pavements. To take into account effects of rutting resulting hydroplaning speeds, the water film depth on rutting pavement are examined under three scenario: (1) at the onset of storm events: rainy water hasn't developed a layer of film on non-rutting pavements but start to accumulate in rutting areas; (2) during storm events: the water film has been formed on non-rutting pavement surface; (3) after storm events: the trapped water in rutting area may develop a layer of water film that might cause hydroplaning risks. The WFD estimation model developed under the three scenarios is termed as 3S-WFD model.

In this study the reference rainfall intensity is defined to examine which pavement segment may present the hydroplaning risks. It can be back calculated with Gallaway model. During storm event, both scenarios 1 and 2 need to analyzed if the local rainfall intensity is greater than the reference rainfall intensity. However, only scenario 1 need to be analyzed if the rainfall intensity is less than the reference rainfall intensity since the water film would be not developed on the non-rutting areas.

To demonstrate the application of Gallaway model on hydroplaning speed prediction for rutting pavements, pavement section with a length of 4 miles is chosen. EMTD, cross slope, and longitudinal are calculated with the same procedures used in Chapter 5 and 6. The local rainfall intensity is obtained from NOAA database. The Gallway model and 3S-WFD model are used to calculate the WFDs under the three scenarios. In addition, the effects of cross slope on rutting ponding is also analyzed in this study, and used in scenario 3. The findings indicate different evaluation results are observed when the different scenarios are used for analysis. The effect of rutting on hydroplaning related safety evaluation cannot be negligible, or unexpected traffic accidents may occur.

CHAPTER 8. CONCLUSIONS

This study presents a comprehensive methodology for hydroplaning related safety evaluation with IMU and 1mm 3D texture data. The presented hydroplaning evaluation methods can be implemented for evaluating pavements in various conditions (e.g. with or without rutting), various surface types (e.g. concrete or asphalt), and various geometry features (e.g. straight road, with horizontal curve, or with large longitudinal slope). The presented models enable to integrate the 1mm 3D texture and IMU data to predict hydroplaning speed, and subsequently the predicted hydroplaning speeds can be compared with the posted speed limits to identify the pavement segments with potential hydroplaning, so that pavement engineers may take remedial measures to decrease hydroplaning potential and minimize potential traffic accidents.

In Chapter 3 the existing WFD estimation models and hydroplaning prediction models are evaluated based on field tests. The WFD estimation models include empirical PAVDRN model, analytical PAVDRN model, Gallaway model, and NZ modified model. The hydroplaning speed prediction models contain Agrawal model, Gallaway model, PAVDRN model, and USF model. To validate the various models, pavement texture is collected by LS-40 Surface Texture Analyzer. Cross slope and longitudinal grade data are measured with SurPro3500 Walking Profiler. The rainfall intensity and water film depth is measured by rain gauge and eTape. The friction coefficients are measured with DFT. Once the parameter values used in WFD and hydroplaning models are obtained, they can be incorporated into WFD and hydroplaning speed prediction models to calculate the estimated WFD and hydroplaning speed. By comparing the predicted and measured WFDs, the findings of the study indicate that the WFDs from Gallway model and empirical PAVDRN model have a good agreement with the measured values from eTape. Similarly, findings also indicate the predicted hydroplaning speeds from Gallaway model and USF model have an acceptable agreement with the measured values from DFT.

Two data acquisition technologies namely 3D Ultra and IMU system are presented in Chapter4 to acquire 3D texture data and IMU data. Both systems are mounted on DHDV to conduct data collection at highway speeds up to 60mph. Generally four key parameters are included in hydroplaning speed prediction models, namely MTD, cross slope, longitudinal grade, and rainfall intensity. Different from traditional methods, the MTD calculation is conducted on 3D texture image by simulating sand patch method, and the estimated MTD called EMTD is used to replace the MTD in this study. The 3D texture data are also used to calibrate pavement cross slope along with the IMU roll data. The calibrated cross slope can help suppress the effects of vehicle vibration on the collected IMU data. Longitudinal grade is directly derived from IMU pitch data. The local rainfall intensity data can be obtained from NOAA database. Three approaches namely kinematic method, Geometry method, and Lateral acceleration method are employed to determine the horizontal curve radius. Pavement rutting dimension is measured in accordance with AASHTO PP 69 standard.

In addition, the repeatability test is conducted to validate the quality of DHDV data including IMU data and 3D pavement texture data. Two test sections are chosen as test bed and three repetitive measurements are conducted on each section. ANOVA test results indicate the IMU data has the good reliability regardless of the data collection speed and vehicle vibration. However, the data quality of 3D texture data is not as good as IMU data. Findings indicate the data collection speed and vehicle vibration greatly affect the quality of 3D texture quality. It is recommended that the data collection should be conducted at constant speeds to avoid vehicle vibration to guarantee the quality of 3D texture data.

Chapter 5 presents the application of the original Gallaway model in hydroplaning speed prediction on the regular pavements. Based on the comparison between the predicted speeds with the posted speed limit, pavement segments with potential hydroplaning risks can be identified. As a result, the corrective measures can be taken on the hazardous sections to prevent the hydroplaning related accidents.

Chapter 6 presents the use of the modified Gallaway and USF model in the hydroplaning speed prediction on pavements on horizontal curve or with large longitudinal grade. The effects of flow path slope on vertical wheel load are investigated, based on the modified Gallaway and USF models. Subsequently the modified models are used for hydroplaning speed predictions on pavements with horizontal curve or large longitudinal grade. As a result, pavement segments with potential hydroplaning risk can be identified.

Chapter 7 presents the use of the 3S-WFD model developed in this study and original Gallaway hydroplaning speed model in hydroplaning speed prediction on rutting pavements. In this chapter the water film depths of rutting pavement are examined under three scenarios: 1) at the onset of storm event: the water film hasn’t been formed on non-rutting areas; 2) during the storm event: the water film has been formed on non-rutting areas; 3) after storm event. A new model named as 3S-WFD model is developed to calculate the rutting water film depth under the three scenarios. In addition, the effects of cross slope on rutting ponding is also analyzed in this study, and used in scenario 3. The findings indicate different evaluation results are observed when the different scenarios are used for analysis. The effects of rutting on hydroplaning related safety evaluation cannot be ignored in pavement safety evaluation.

REFERENCES

AASHTO, 2004 “A policy of geometric design of highway and street”, 5 Edition.

AASHTO, 2010, “Standard Practice for Determining Pavement Deformation Parameters and Cross Slope from Collected Transverse Profiles”, AASHTO Designation: pp69-10

Ahmed, Z., White, T.D., and Kuczek, T., 1997 “Comparative Field Performance of Subdrainage Systems.” *Journal of Irrigation and Drainage Engineering, ASCE,* Vol. 123, No. 3, pp. 194-201.

Anderson David A., Huebner R. Scott, Reed R. Joseph, Warner John C., 1998 “Improved surface drainage of pavement”, Final report NCHRP 16 Project 1-29.

American Society for Testing and Materials (ASTM), 2011. ASTM E 303: Standard Test Method for Measuring Surface Frictional Properties Using a British Pendulum Tester, ASTM Standard Practice E 303 Book of ASTM Standards, Volume 04.03 Philadelphia, P A.

American Society for Testing and Materials (ASTM), 2011. ASTM E 867: Standard Terminology Relating to Vehicle-Pavement Systems, ASTM Standard Practice E 867 Book of ASTM Standards, Volume 04.03 Philadelphia, P A.

American Society for Testing and Materials (ASTM), 2011. ASTM E 965: Standard Test Method for Measuring Pavement Macro texture Depth Using a Volumetric Technique, ASTM Standard Practice E 965 Book of ASTM Standards, Volume 04.03 Philadelphia, P A.

American Society for Testing and Materials (ASTM), 2011. ASTM E 1845: Calculating Pavement Macro texture Profile Depth, ASTM Standard Practice E 1845 Book of ASTM Standards, Volume 04.03 Philadelphia, P A..

American Society for Testing and Materials (ASTM), 2011. ASTM E 1911: Standard Test Method for Measuring Paved Surface Frictional Properties Using Dynamic

Friction Tester, ASTM Standard Practice E 1911 Book of ASTM Standards, Volume 04.03 Philadelphia, P A.

American Society for Testing and Materials (ASTM), 2011. ASTM E 2157: Standard Test Method for Measuring Pavement Macro texture Properties Using the Circular Track Meter, ASTM Standard Practice E 2157 Book of ASTM Standards, Volume 04.03 Philadelphia, P A.

American Society for Testing and Materials (ASTM), 2011. ASTM E 2380: Standard Test Method for Measuring Pavement Texture Drainage Using an Outflow Meter, ASTM Standard Practice E 2380 Book of ASTM Standards, Volume 04.03 Philadelphia, P A.

Balmer G. G., Gallaway B. M. 1983 “Pavement design and controls for minimizing automotive hydroplaning and increasing traction”. *Frictional Interaction of Tire and Pavement*, ASTM STP 793, W.E. Meyer and J.D. Walter, Eds., American Society for Testing and Materials, pp: 167-190

Bancroft Jared B., and Lachapelle Gerard, 2011 “Data fusion algorithms for multiple Inertial Measurement Units”, *Sensors (Academic Journal)*, Vol.11, Issue 7, p6771

Beer F.P., Johnston E.R. Jr, 1977. "Vector Mechanics for Engineers-dynamics", *Mc Graw-Hill*, New York.

Bergstrom Torbjorn, 2001 “Investigation of measurement artifacts introduced by horizontal scanning surface profiling instruments”, A thesis of Worcester Polytechnic Institute.

Bolzon G., Caroti G., and Piemonte A. 2007 “Road’s cross slope measurement: evaluation’s algorithms and accuracy analysis”, *International Symposium on Mobile Mapping Technology*.

Browne A.L., 1975 “Mathematical Analysis for Pneumatic Tire Hydroplaning. Surface Texture versus Skidding: Measurements, Frictional Aspects, and Safety Features of Tire-Pavement Interactions”, ASTM STP 583, American Society for Testing and Materials, pp. 75-94.

Cao-Changyong, Fwa-TF, Ong-Ghim-Ping, 2011 "Comparing Hydroplaning Characteristics of Trucks with Wide-Based and Conventional Dual Tires", *TRB Annual Meeting*

Carlson P. J., Burris M, Black K and Rose E. R. 2005 “Comparison of Radius-Estimating Techniques for Horizontal Curves”. *Transportation Research Record: Journal of the Transportation Research Board*, No. 1918. Washington, D.C. pp. 76-83.

Carlson P. J. and J. M. Mason Jr. 2008 “Relationships between Ball Bank Indicator, Readings, Lateral Acceleration Rates, and Vehicular Body-Roll Rates”. *In Transportation Research Record: Journal of the Transportation Research*. USA.

Campbell Scientific, INC., 2007 "Vaisala DSC111 Remote Road Surface state Sensor", App. Note Code: 2MI-S.

Caroti G., and Piemonte A. 2010 “Measurement of cross slope of roads: evaluations, algorithms and accuracy analysis”, *International Journal: Survey Review, Volme 42, Issue 315* (01 January 2010), pp. 92-104

Chesterton John, Noel Nancekivell, Noel Tunnicliffe, 2006 "The use of the Gallaway Formula for Aquaplaning Evaluation in New Zealand", *Transit New Zealand and New Zealand Institute of Highway Technology (NZIHT) Annual Conference*, 8th.

Christopher, B.R. and V.C. McGuffey. 1997 "NCHRP Synthesis of Highway Practice 239: Pavement Subsurface Drainage Systems", *TRB, National Research Council*, Washington, D.C.

Coiret, A., 2005. “Spectroscopic evaluation of pavement wetting states: Influence on tire/road friction”. Nantes: LCPC.

Duminda I. B Randeniya, 2007 "Automaic geo-referencing by integrating camera vision and inertial measurements", Ph.D. Dissertation of University of South Florida.

Fitzpatrick, K., L. Elefteriadou, D.W. Harwood, J.M. Collins, J. McFadden, I.B. Anderson, R.A. Krammes, N. Irizarry, K.D. Parma, K.M. Bauer, and K. Passetti, 2000 "Speed Prediction for Two-Lane Rural Highways". *FHWA-RD-99-171. Federal Highway Administration*, U.S. Department of Transportation.

FLUKE Technology, "Fluke 289 True-rms Industrial Logging Multimeter with TrendCapture", June 2015, http://www.fluke.com/fluke/r0en/digital-multimeters/advanced-multimeters/fluke-289.htm?PID=56061

Gallaway, B. M., Schiller, R. E., & Rose, J. G. 1971 “The effects of rainfall intensity, pavement cross slope, surface texture and drainage length on pavement water depths”. *Texas: Texas Transportation Institute*.

Gallaway, B. M., et. al., 1979 "Pavement and Geometric Design Criteria for Minimizing Hydroplaning," *Federal Highway Administration*, Report No. FHWA-RD-79-31.

Gunaratne, M., Lu, Q., Yang, J., 2012 “Hydroplaning on Multi Lane Facilities”, *Report for Florida Department of Transportation*, Report No. BDK84 977-14.

Henry, J.J. 2000 "Evaluation of pavement friction characteristics". *NCHRP Synthesis of Highway Practice 291, Transportation Research Board*, National Research Council, Washington, D.C.

Horne, W.B., et al. 1962 “Influence of Tire Tread Pattern and Runway Surface Condition on Braking Friction and Rolling Resistance of a Modern Aircraft Tire,” NASA TN D-1376.

Horne, W.B., and Dreher. R.C., 1963 “Phenomena of Phenumatic Tire Hydroplaning”, *NASA TN D-2-56, NASA Langley Research center,* NASA, Hampton, VA.

Huebner. R.S., et al., 1996"PAVDRN Computer Model for Predicting Water Film Thickness and Potential or Hydroplaning on New and Reconditioned Pavements.” *Transport Research Record 1599*, pp. 128-131.

International Cybernetics, "SurPRO 3500", June 2015, http://www.intlcybernetics.com/surface_profiler_surpro_3500.html

Ivey, D.L., Lehtipuu, E. K., and Button, J. W., 1975 “Rainfall and Visibility – The View From Behind the Wheel,” *Research Report 135-3, Texas Transport Institute,* College Station, Tex.

Jayasooriya Waruna, Gunaratne M.Sc. Manjriker, 2014 "Evaluation of widely used hydroplaning risk prediction methods using Florida's past crash data", TRB Annual Meeting.

Jenq Syh-Tsang and Chiu Yuen-Sheng, 2011 "Verification and Analysis of Transient Hydroplaning Performance for inflated Radial Tire with V-shaped Groove Tread Pattern on the Fluid Structure Interaction Scheme", *ICCES*, vol.16, no.1, pp.15-15

Kulakowski, B. T., & Douglas, H. W. 1990 “Effect of water-film thickness on tire pavement friction”. *Surface characteristics of roadways: international research and technologies,* 50-60.

Kumar, Santosh S, Kumar, Anupam, Kumar, Anupam, 2010 "Analyzing Effect of Tire Groove Patterns on Hydroplaning Speed", *Journal of the Eastern Asia Society for Transportation Studies*, Vol.8.

Kumar S. Santosh, Kumar Anupam, T.F. FWA, 2009 "Analyzing effect of tire groove patterns on hydroplaning speed", *Journal of the Eastern Asia Society for Transportation Studies*, Vol.8.

Larson, R.M. and Smith K.L., 2010 “Relationship between Pavement Surface Characteristics and Crashes, Volume 1–Synthesis Report.” *Final Report prepared for Federal Highway Administration,* Washington, DC.

Luo, Wenting, Wang, Kelvin C. P., Li, Lin 2014 “Surface Drainage Evaluation for Rigid Pavements Using IMU and 1 mm 3D Texture Data”, *Transportation Research Record: Journal of the Transportation Research Board*, Pavement Management, Volume 3, pp121-128.

Mallela, J., L. Titus-Glover, and M. Darter, 2000 “Considerations for Providing Subsurface Drainage in Jointed Concrete Pavements,” *In Transportation Research Record 1709, TRB, National Research Council*, Washington, D.C. pp. 1-10.

Mekemson et al, 2002 “Method and Apparatus for Pavement Cross-slope Measurement”, *Patent Application Publication*, Pub. No.: US 2002/0013644 A1, Jan. 31.

Miller, John S. and William Y. Bellinger, 2003 “Distress Identification Manual for the Long-Term Pavement Performance Program.” *U.S. Department of Transportation*, pp. 90-91.

MILONE Technology, "eTape™ continuous fluid level sensor", June 2015, http://www.milonetech.com/About_eTape.php

MnROAD, "MnROAD Rutting -- All Measurement Types", June 2011, http://www.mrr.dot.state.mn.us/research/dataproduct/Data

NAASRA (National Association of Austrialian State Road Authorities), 1974 “Drainage of Wide Flat Pavements,” NAASRA.

Negrini Neto, Osvaldo, 2003 "Treaty for Criminalistics Evaluations -- dynamics of traffic accidents: analyses and reconstructions". *Porto Alegre. Sagra-Luzzatto*.

NOAA's National Water Service, Hydrometeorological Design Studies Center, "Precipitation Frequency Data Server (PFDS)": http://dipper.nws.noaa.gov/hdsc/pfds/, Accessed on July, 2015

Okano Toshihiko and Koishi Masataka, 2001 "Hydroplaning Simulation using MSC.Dytran", *The Yokohama Rubber CO., LTD. 2-1 Oiwake Hiratsuka Kanagawa 254-8601*, Janpan.

Ong, G.P. and Fwa, T.F., 2007 “Wet-pavement hydroplaning risk and skid-resistance: Modeling”, *ASCE Journal of Transportation Engineering*, Vol. 133, No. 10

Ong, Ghim Ping, Fwa, Tien F, 2008 "Hydroplaning Risk Management for Grooved Pavements", *Seventh International Conference on Managing Pavement Assets*.

Paine John E., "Skid Resistance of Concrete Pavements", Concrete Construction October 1969, http://www.concreteconstruction.net/concrete-articles/skid-resistance-of-concrete-pavements.aspx

Park Hun Myoung, 2009 “Comparing Group Means: T-tests and One-way ANOVA Using Stata, SAS, R and SPSS”, http://creativecommons.org/licenses/by/3.0/

Roe, P. G., Hewitt, A. P., Parry, A. R., May, R. W., & Cheetham, R. J., 1997. “Water depths on wide carriageways - a laboratory study”. *Crowthorne: Transport Research Foundation*.

Ross, N. F., & Russam, K. 1968 “The depth of rain water on road surfaces”. *Wokingham: Road Research Laboratory*.

Russam, K. and Ross, N.F., 1968 "The Depth of Rain Water on Road Surfaces." *Road Research Laboratory, Ministry of Transport Report No. LR 236*, 25pp.

Shah, Yogesh U. , Jain, S.S. , and Parida, Manoranjan 2014 “Evaluation of prioritization methods for effective pavement maintenance of urban roads”, *International Journal of Pavement Engineering*, Volume 15, Issue 3, pp 238-250.

Smith Kelly L. and Larson Roger, 2011 “Engineering safety road surface to help achieve U.S. highway safety goal”, *the 3rd International Conference on Road Safety and Simulation September 14-16,* Indianapolis, IN, USA.

Tsai Yichang (James), Ai Chengbo, Wang Zhaohua, Eric Pitts, 2012 "A MOBILE CROSS SLOPE MEASUREMENT METHOD USING LIDAR TECHNOLOGY", *Georgia Institute of Technology 2013 TRB Presentations*, 07, 31

Vemulapalli, Pramod, Brennan, Sean N, 2009 "Design and Testing of a Terrain Mapping System for Median Slope Measurement", *Transportation Research Board 88th Annual Meeting*.

Vogt Florian and Fevrier Pierre, 2013 "Measurements of the grip level and the water film depth for real accidents of the german in-depth accident study (GIDAS)." BASt, PP 1-11.

Wambold, J.C., C.E. Antle, J.J. Henry, and Z. Rado. 1995. “International PLARC Experiment to Compare and Harmonize Texture and Skid Resistance Measurements,” *AIPCR*-01.04.T.

Wang Kelvin C.P., 2011 "Automated Survey of Pavement Distress based on 2D and 3D Laser Images", *Report for MBTC DOT* 3023.

Wang, Kelvin C.P., Li, Lin, 2011 “Potential Measurement of Pavement Surface Texture based on Three-Dimensional (3D) Image Data”, *Transportation Research Board 91th Annual Meeting*, Washington, D.C. USA.

Wikipedia, "Rain gauge", June 2015, http://en.wikipedia.org/wiki/Rain_gauge.

XSENS, “Inertial Measurement Unit ", June 2015, https://www.xsens.com/tags/imu/

Yang N.C., 1972 “Design of Functional Pavements”. *McGraw-hill Book Company,* New York.

VITA

WENTING LUO

Candidate for the Degree of

Doctor of Philosophy

Thesis: PAVEMENT HYDROPLANING EVALUATION BASED ON IMU AND 1MM 3D TEXTURE DATA

Major Field: Civil (Transportation) Engineering

Biographical:

Education:

Completed the requirements for the Doctor of Philosophy in Civil Engineering at Oklahoma State University, Stillwater, Oklahoma in July, 2015.
Completed the requirements for the Master of Civil Engineering at University of Arkansas, Fayetteville, United States in 2012.
Completed the requirements for the Master of Safety Engineering at Beijing Jiaotong University, Beijing, China in 2008.
Completed the requirements for the Bachelor of Business Administration at Beijing University of Civil Engineering and Architecture, Beijing, China in 2006.

Experience:

Jan 2013- Present: Research Assistant, Department of Civil and Environmental Engineering, Oklahoma State University